Title
Investigation of Bio-Directed Assembly of Metal Oxide and Metal Nanomaterials for Chemiresistive Gas Sensor

Permalink
https://escholarship.org/uc/item/9ds58974

Author
Moon, Chung Hee

Publication Date
2015

Peer reviewed|Thesis/dissertation

UNIVERSITY OF CALIFORNIA
RIVERSIDE

Investigation of Bio-Directed Assembly of Metal Oxide and Metal Nanomaterials for Chemiresistive Gas Sensors

A Dissertation submitted in partial satisfaction
of the requirements for the degree of

Doctor of Philosophy

in

Materials Science and Engineering

by

Chung Hee Moon

August 2015

Dissertation Committee:
Dr. Elaine D. Haberer, Chairperson
Dr. Nosang V. Myung
Dr. Huinan Liu

The Dissertation of Chung Hee Moon is approved:

Committee Chairperson

University of California, Riverside

Acknowledgements

I would first like to thank my advisor Professor Elaine D. Haberer for her support and guidance throughout the years. She has encouraged me to push through times of difficulty and helped me develop various traits of a scientist from critical thinking to scientific and organization skills. With her mentoring, I was able to gain knowledge in the field of electronic materials and devices and to apply biologically mediated methods for such engineering technologies. Her passion and teachings have immensely influenced me. I thank my committee members Professor Huinan Liu and Professor Nosang V. Myung for their advice and support for this dissertation. Additional appreciation is towards Professor Myung, whom I have collaborated closely on this work on chemiresistive gas sensors, for his insightful suggestions and guidance.

I also thank Dr. Mohammed Shahriar Zaman for our times together as colleagues and friends. It was a great opportunity working closely with him on copper sulfide projects as well as on every part of the laboratory. I appreciate all the scientific and non-scientific discussions we had, which has been encouraging and valuable. Dr. Miluo Zhang have shared her specialty in gas sensors and helped initiate experiments on this project. I thank her for the collaboration and practical assistances.

I am thankful for Haberer group members, past and present: Xiaoyin Ma, Joon-Bok Lee, Steven Garcia, Hector Lopez-Hernandez, Marzieh Tousi, Jeffrey Young, Gabriel Grajeda, Joseph Cheeney, Tam-Triet Ngo-Duc, Yiran Yan, Joshua Plank, Kalie Inouye, and Esmeralda Catalan for their support and discussions that go above and beyond. I give my special thanks and acknowledge Steven Garcia for his work on sulfo-SMCC

chemical modification, Marzieh Tousi for her work on zinc oxide biopanning and binding studies, as well as Yiran Yan for her initial work on palladium deposition.

I also thank all the help I received from various centers and laboratories at UCR. Dr. Nicha Chartupryoon, Dr. Heng (Charles) Su, Dr. Jiwon Kim, and Chanling Li have been open for insightful discussions and provided assistances and know-hows for using equipment in the Myung lab. Moreover, Dexter Humphrey and Dr. Dong Yan at the Center for Nanoscale Science and Engineering have trained and assisted usage of cleanroom equipment and techniques. Dr. Songqin Pan at the Institute for Integrative Genome Biology provided training on MALDI-TOF. Stephen McDaniel, Mathias Rommelfanger, and Dr. Krassimir N. Bozhilov at the Central Facility for Advanced Microscopy Microanalysis trained and provided insights on various electron microscopy analyses. Dr. Dan Borchardt and Dr. Richard Kondrat at Analytical Chemistry Instrumentation Facility provided training for optical and mass spectroscopy equipment.

I have met wonderful colleagues and friends over the years at UCR, and treasure every one of these relationships. I am forever grateful for the encouragement, guidance and prayers from my parents, sister and brother, as well as for the caring support from my family-in-law. Lastly, I send my greatest gratitude to my husband Jehoon Kim and my son Matthew Danwoo Kim. They have been tremendously supportive, patient and have been my source of energy and joy through all.

This dissertation includes reprints in part of previously published materials that appeared in Nanotechnology (Moon, C. H., et al., Nanotechnology 25, 135205, 2014) and Applied Physics Letters (Moon, C. H., et al., APL 105, 223102, 2014).

ABSTRACT OF THE DISSERTATION

Investigation of Bio-Directed Assembly of Metal Oxide and Metal Nanomaterials for Chemiresistive Gas Sensors

by

Chung Hee Moon

Doctor of Philosophy, Graduate Program in Materials Science and Engineering
University of California, Riverside, August 2015
Dr. Elaine D. Haberer, Chairperson

With increasing development in nanotechnology, approaches for synthesis of nanomaterials with control over dimensions, grain size and crystallinity for various device applications is highly demanded. Biological building blocks such as amino acids direct assembly of intricate structures from nano- to macro-scale within the living system. Such ability of biological molecules have gained scientific interest to meet nanofabrication challenges and demands. A 1 μm long, filamentous M13 bacteriophage, in particular, is a promising biological molecule for synthesis of one-dimensional inorganic nanostructures. The genetic information can be easily manipulated to display specific peptide sequences on the M13 bacteriophage outer protein coats and has been involved in combinatorial phage display technology to identify inorganic specific peptide sequences. Furthermore, various inorganic nanomaterials have been synthesized by the M13 bacteriophage and its protein components. With our daily exposure to hazardous gases such as H_2S, H_2, CO, and NH_3, gas sensors with high sensitivity, low detection limit, low power consumption and miniature size for mobile and continuous monitoring are in demand. Nanoscale chemiresistive gas sensors have a relatively simple configuration and can be used for sensitive monitoring of gas levels with low power consumption. The large surface area to volume ratio provides increased adsorption sites for sensor-analyte interactions and the short diffusion length allows a rapid resistance change with exposure to low gas concentrations.

In this work, a novel platform for metal-based H_2S and H_2 chemiresistive gas sensors has been designed based on a gold-binding bacteriophage template. Continuous nanocrystalline gold chains assembled on the M13 bacteriophage backbone displayed high sensitivity and low lowest detection limit for H_2S sensing. The carboxyl and amine functional groups on the template with an affinity for sulfur added to device sensitivity. The same platform was also adapted for hybrid gold-palladium nanopeapod sensors for H_2 sensing. The sensor showed high response to low H_2 concentrations at ambient conditions. Moreover, bio-directed ZnO synthesis from M13 bacteriophage protein coats and peptide components were explored. Materials characterization revealed peptide concentration dependent morphology, crystallinity, and optical property tuning. This work demonstrates the promise of bio-directed nanofabrication for sensitive chemiresistive gas sensors.

Table of Contents

Chapter 1. Introduction.. 1

1.1 Motivation 1

1.2 Biomineralization and Bio-Assembly 2

1.3 M13 Bacteriophage... 4

1.3.1 Background.. 4

1.3.2 pIII Phage library and peptide selection 6

1.3.3 pVIII phage library and templated inorganic assembly...................... 6

1.4 Chemiresistive Gas Sensors 7

1.4.1 Background.. 7

1.4.2 Metal-based Gas Sensor 11

1.4.3 ZnO-based Gas Sensor 13

1.5 Scope of Work.. 15

Chapter 2. Nanocrystalline Gold-Based H_2S Gas Sensor... 16

2.1 Introduction 16

2.2 Experimental details... 19

2.2.1 Assembly of viral-templated gold nanowire gas sensors 19

2.2.2 Morphological characterization... 21

2.2.3 Resistance measurements 22

2.2.4 Sensor performance analysis 22

2.3 Results and discussion 23

2.3.1 Morphological characteristics of nanocrystalline gold nanowires 23

2.3.2 Electrical characteristics of viral-templated gold nanowire devices . 29

2.3.3 Sensing performance of viral-templated gold nanowire devices....... 33

2.4 Conclusion 41

Chapter 3. Gold-Palladium Nanopeapod H_2 Sensor 42

3.1 Introduction 42

3.2 Experimental details... 43

3.2.1 Au-Pd nanopeapod assembly on substrate 43

3.2.2 Morphological and materials characterization.................................. 45

3.2.3 Electrical and sensor characterization 45

3.3 Results and discussion.. 46

3.4 Conclusion 61

Chapter 4. ZnO Nucleation on Viral-Scaffold 62

4.1 Introduction 62

4.2 Experimental details... 64

4.2.1 Genetic insertion of ZnO-binding peptide in pIII............................. 64

4.2.2 Chemical conjugation of peptide with sulfo-SMCC linker 65

4.2.3 Matrix-assisted laser desorption/ionization (MALDI) analysis 66

4.2.4 ZnO nanocrystal synthesis on M13 bacteriophage protein coat........ 67

4.2.5 Morphological characterization 68

4.3 Results and discussion.. 68

4.4 Conclusion 75

Chapter 5. Peptide-Assisted ZnO Nanomaterial Synthesis.. 77

5.1 Introduction 77

5.2 Experimental details.. 79

5.2.1 Combinatorial phage display technology using the pVIII library 79

5.2.2 Binding test against ZnO 81

5.2.3 Nucleation with ZnO-binding phage 81

5.2.4 ZnO synthesis with specific peptide additives.................................. 82

5.2.5 Morphology and crystallinity characterization................................. 82

5.2.6 Optical characterization... 82

5.2.7 Device fabrication and photoresponse measurement 83

5.3 Results and discussion 84

5.4 Conclusion 100

Chapter 6. Conclusion 101

Chapter 7. Future Work... 105

References.. 107

Appendix A. Construction of pVIII Library 123

Appendix B. Discovery of SiO_2-Binding Peptides 125

List of Figures

Figure 1-1 Schematic diagram of M13 bacteriophage with five structural proteins pVIII, pIII, pVI, pVII, and pIX enclosing single-stranded DNA in center. 5

Figure 1-2 Simplified Chimera image of (a) pIII (yellow) and pVIII (blue) coat proteins displayed on its location, (b) top-down view of pVIII protein arranged in five-fold symmetry, and (c) single α-helical pVIII coat protein with amine (cyan) and carboxyl (red) side groups indicated [24]. 5

Figure 1-3 Schematic illustration of sensor response vs. time plot. Key parameters, response, response and recovery times, are labeled. 9

Figure 1-4 Schematic illustration of sensor calibration curve displaying response vs. concentration of gas analyte. Sensor dynamic range, lower detection limit (LDL), upper detection limit (UDL) and sensitivity are indicated according to the definition. 10

Figure 1-5 Zinc oxide (ZnO) (a) wurtzite and (b) zinc blende crystal structures displaying single unit cell (created by software VESTA) [72]. Zinc and oxygen atoms are colored in gray and red, respectively. 14

Figure 2-1 Schematic representation of the sensor fabrication process for as-assembled devices. (a) O_2 plasma treatment of pre-patterned gold electrodes to enhance surface hydrophilicity. (b) Non-specific adsorption of gold-binding phage on the patterned substrate. (c) Specific binding of 5 nm gold nanoparticles to the pVIII coat protein of the gold-binding phages. (d) Nanocrystalline gold nanowires formed through seeded, electroless deposition. 21

Figure 2-2 Morphology of viral-templated gold nanowires within fabricated devices assembled with a $1x10^8$ pfu/μL phage concentration and a range of electroless deposition times. (a) Low magnification SEM image that shows viral-templated gold nanowires with a 3 min electroless deposition time on 50 μm electrode and across 3 μm gap. Scale bar is 1 μm. High magnification SEM images of viral-templated gold nanowires with electroless deposition times of (b) 3 min, (c) 7 min, and (d) 12 min. Gold nanoparticles are assembled in a bead-like nanowire form with increasing nanowire widths corresponding to increasing electroless deposition time. Scale bars are 1 μm. 25

Figure 2-3 High magnification scanning electron microscopy (SEM) image of viral-templated gold nanowires. Viral-templated gold nanowires in an (a) as-assembled device in which the viral template was intact and (b) the same device and location following an ethanol treatment in which the template was removed. Scale bars are 200 nm. 26

Figure 2-4 Morphology and connectivity of viral-templated gold nanowires. TEM image shows a fragment of a viral-templated gold nanowire that was removed from the substrate with ultrasonication. Scale bar is 100 nm. High magnification TEM image (inset) shows fused, polydisperse gold nanoparticles within a different nanowire fragment. Scale bar is 20 nm. 26

Figure 2-5 Dependence of gold nanowire surface coverage on phage template concentration. SEM images of gold nanowire devices assembled with phage concentrations (a) 1×10^8 pfu/μL, (b) 3×10^8 pfu/μL, (c) 5×10^8 pfu/μL and a 3 min electroless deposition time. Scale bars are 1 μm. 28

Figure 2-6 Dependence of electrical behavior of gold nanowire devices on electroless deposition time and phage concentration. The device yield associated with each assembly condition is written above the relevant data. Median resistances of the devices with maximum and minimum values are shown as a function of (a) electroless deposition time and (b) phage concentration. 30

Figure 2-7 Histograms of resistances for as-assembled and ethanol-treated devices fabricated using a 3×10^8 pfu/μL phage concentration and 3 min electroless deposition. 32

Figure 2-8 Representative room temperature H_2S sensing behavior of (a) as-assembled and (b) ethanol-treated viral-templated gold nanowire devices. Sensors were alternately exposed to H_2S and dry air for intervals of 15 and 30 min, respectively. Dashed line indicates the H_2S concentration to which the sensors were exposed at each time. Calibration curve of (c) as-assembled and (d) ethanol-treated sensors showing sensor response to H_2S concentrations between 0 and 0.5 ppm. Inset in (d) shows calibration curve of ethanol-treated devices for H_2S concentrations between 0 and 40 ppm. 35

Figure 2-9 Sensing response of viral-templated gold nanowire sensors to exposure to 0.5 ppm of H_2S, NH_3, and NO_2 gases. 36

Figure 3-1 Schematics of viral templated Au-Pd nanopeapod assembly and chemiresistor geometry. (a) A gold-binding M13 virus was used to bind Au nanoparticles which were used as seeds for Pd deposition. (b) A chemiresistor composed of a random network of Au-Pd nanopeapods bridging two electrodes. 44

Figure 3-2 High magnification scanning electron microscope (SEM) images of (a) Au nanoparticle seeds and Au-Pd nanopeapods assembled with (b) thick and (c) thin Pd deposition. Scale bar is 200 nm. 47

Figure 3-3 Energy dispersive spectroscopy spectrum of thick Au-Pd nanopeapods. Au and Pd were present in addition to Si and O from the substrate and Ag from the silver paste for grounding... 48

Figure 3-4 (a) Scanning electron microscopy image and (b-d) energy dispersive spectroscopy elemental mapping of thick Au-Pd nanopeapods with an average diameter of 50 ± 11 nm on a Si/SiO_2 substrate. SEM image is overlapped with elemental mapping of (b) both Au and Pd, (c) Au only, and (c) Pd only. Yellow and magenta are used to indicate the presence of Au and Pd, respectively. 49

Figure 3-5 Energy dispersive spectroscopy spectrum of thin Au-Pd nanopeapods. Au and Pd were present in addition to Si and O from the substrate and Ag from the silver paste for grounding........ 50

Figure 3-6 (a) Scanning electron microscopy image and (b-d) energy dispersive spectroscopy elemental mapping of thin Au-Pd nanopeapods with an average diameter of 29 ± 8 nm on a Si/SiO_2 substrate. SEM image is overlapped with elemental mapping of (b) both Au and Pd, (c) Au only, and (c) Pd only. Yellow and magenta are used to indicate the presence of Au and Pd, respectively. 51

Figure 3-7 Representative I-V curves for Au-Pd nanopeapod devices with (a) thick and (b) thin Pd deposition shown with median resistance values for each fabrication condition. 53

Figure 3-8 Representative real-time sensing behavior of thick Au-Pd nanopeapod sensors. (a) Sensors were exposed to H_2 for 15 min followed by dry air for 30 min. Corresponding H_2 concentrations, ranging from 100 to 2000 ppm$_v$, are shown with dashed lines. (b) Sensors were conditioned by exposure to 2000 ppm$_v$ H_2 gas for 3 hours. Subsequently, sensors were alternately exposed to dry air for 30 min followed by 2000 ppm$_v$ H_2 for 15 min. H_2 gas on and off points are shown with dashed lines. Inset displays sensor response throughout entire conditioning and H_2/air alternating exposure sequence. 55

Figure 3-9 (a) Representative real-time sensing behavior and (b) average calibration curve of thin Au-Pd nanopeapod sensors. Sensors were exposed to H_2 for 15 min followed by dry air for 30 min. Corresponding H_2 concentrations, ranging from 50 to 2000 ppm$_v$, are shown with dashed lines. 58

Figure 4-1 Ball-and-stick model of ZnO-binding sequence, EAHVMHKVAPRP, built using Chimera software [24]. 64

Figure 4-2 (a) Chemical structure of sulfo-SMCC and (b) Chimera image of pVIII coat protein [24]. The amine groups present in pVIII coat protein are indicated in green, and the sulfo-SMCC linker molecule can conjugate to the n-terminus and lysine residue. 66

Figure 4-3 Transmission electron microscopy (TEM) images of ZnO nanoparticles formed on the pIII genetically modified M13 bacteriophage after 10 h of incubation. (a) A single M13 bacteriophage with nanoparticle attached at one end and (b) shows polydispersity of nanoparticles formed. TEM images were negatively stained with 2% uranyl acetate. 69

Figure 4-4 Histogram to show distribution of ZnO nanoparticle diameters obtained from 10 mM $Zn(OH)_2$ after 10 h incubation. 70

Figure 4-5 The average diameter of ZnO nanoparticles at different precursor and incubation times. 71

Figure 4-6 Percent coverage of ZnO-binding peptide on phage with 0.238 mM available sites with respect to concentration of peptides added in reaction. 72

Figure 4-7 MALDI-TOF MS spectra of pVIII coat protein with sulfo-SMCC and ZnO-binding peptide conjugation. 73

Figure 4-8 Transmission electron microscopy (TEM) images of flocculated ZnO-binding peptide-conjugated phages (a) after uranyl acetate staining and (b) after ZnO nucleation at room temperature in film-like form. (c) Energy dispersive x-ray spectrum (EDS) of nucleated material on flocculated ZnO-binding peptide-conjugated phages shown in (b). Copper and carbon peaks likely originate from carbon-coated copper grid used. 75

Figure 5-1 Schematic diagram of one complete round of combinatorial phage display technique (biopanning) from pVIII phage display library. 80

Figure 5-2 (a) Ball-and-stick model of identified ZnO-binding peptide sequence, VPGAAEHT. (b) The binding strength of the ZnO-binding and the wild-type phages for ZnO. Inset shows optical images of ZnO nanoparticle dispersion (left) with and (right) without the addition of the ZnO-binding phage. 88

Figure 5-3 Transmission electron microscopy (TEM) images (inset, scale bar: 0.5 μm) and corresponding electron diffraction patterns of ZnO nanostructures synthesized with varied peptide concentrations. 90

Figure 5-4 Representative energy dispersive x-ray spectra (EDS) of peptide-assisted structures synthesized with (a) no peptide and (b) 0.6 mM ZnO-binding peptide on carbon-coated copper TEM grid. 91

Figure 5-5 Scanning electron microscopy (SEM) images of ZnO nanostructures synthesized with the addition of varied peptide concentrations (scale bar: 2 μm). 92

Figure 5-6 Aspect ratio (Length/Diameter) of ZnO structures synthesized with the addition of peptide concentrations from 0 to 0.05 mM. 94

Figure 5-7 Fourier transform infrared (FTIR) spectra of ZnO-binding peptide (black) and ZnO nanostructures prepared with no peptide (red) and 0.1 mM peptide (blue). The absorbance of the ZnO-binding peptide spectrum was multiplied by 3 to aid in visualization. 95

Figure 5-8 Photoluminescence (PL) spectra of ZnO nanostructures formed with different peptide concentrations: (top) 0, 0.005, 0.01, 0.05, 0.1, and (bottom) 0.31, 0.6 mM. Emission intensity was normalized to the band-edge or near band-edge peak. 97

Figure 5-9 Schematic band diagram of intrinsic sub-bandgap defect levels in ZnO........ 98

Figure 5-10 Photoresponse of ZnO film composed of nanostructures synthesized with 0.1 mM peptide to illumination of 527 nm green light. Constant bias of 0.15 V was applied. Light turned on at t=0 and turned off after 5 min. Five min cycles of on/off repeated 4 times. 99

Figure B 1 The binding strength of recurrent, consensus, and wild-type phages for SiO_2 (red) and Au (blue). Bar height that starts from 0 indicates concentration of phages that were bound and eluted from each target materials. 129

List of Tables

Table 2-1 Chart to compare sensor performance of gold nanoparticle-based H_2S chemiresistive sensors. Work described in this chapter in bold...................... 40

Table 3-1 Chart to compare sensor performance of nanoscale Pd-based H_2 chemiresistive gas sensors. Work in this chapter in bold... 60

Table 5-1 List of peptide sequences obtained after 5 rounds of biopanning. The isoelectric point of each peptide was calculated using peptide property calculator by Innovagen AB (http://PepCalc.com). Of the 23 phages analyzed, 6 different peptides were isolated and 11 phages were found to be unmodified. 85

Table 5-2 Statistical analysis of peptides obtained after 5 rounds of biopanning. The frequency of each amino acid occurrence at each position and within all resulting sequences was calculated. The amino acids are presented in single letter form and color coded according to its chemical moieties. Data associated with the 11 unmodified phage were not included in this analysis. 86

Table 5-3 Summary of nucleation conditioned using ZnO-binding phage in solution..... 89

Table A 1 Percentage of expected and actual amino acid groups present pVIII library. 124

Table B 1 List of peptide sequences obtained after 4 rounds of negative biopanning for SiO_2 and not Au. Nineteen sequences were obtained and 2 out of 19 were unmodified phages. 126

Table B 2 Statistical analysis of peptides obtained after 4 rounds of negative biopanning. The frequency of each amino acid occurrence at each position within all resulting sequences was calculated. The amino acids are presented in single letter form and color coded according to its chemical moieties. The consensus sequence is shown at the bottom of the list. 127

Chapter 1. Introduction

1.1 Motivation

Molecules including DNA, amino acids, and monosaccharides are important building blocks of natural biological systems. Especially in the field of biomineralization, amino acids are crucial in directing hierarchical assembly of inorganic materials. These biological molecules collect and transport raw materials to fabricate highly organized nano- to macro-scale structures from the bottom-up. Assembly of these building blocks is genetically controlled and can be manipulated through genetic modification. In addition, biological molecules are very precise in their role and recognition for assembly. Furthermore, amino acids in particular provide highly diverse combinations that are the basis for all the proteins and enzymes in the natural systems. Few amino acids make up a peptide sequence, and depending on the combination, the electrostatic, structural, and self-assembling properties can be altered. Moreover, in the materials perspective, assembly and synthesis from biological components in aqueous condition, mild temperature, pressure, and ambient air are energetically beneficial.

With the development of bionanotechnology, this innate ability of organisms has been utilized and redirected to synthesis of complex nanomaterials for non-biological application such as transistors, lasers, batteries, and sensors. Use of biological molecules facilitates synthesis of intricate and hierarchical nanostructures for improved device performances that are otherwise challenges using conventional methods. Morphology, crystallinity, size, and arrangement of nanomaterials can greatly impact electrical, optical and sensing properties of nanodevices. In this dissertation, M13 bacteriophage template and its protein components with affinity for specific target materials are used to direct assembly of metal and metal-oxide nanostructures for gas sensor applications. The biological components are involved in different stages of gas sensor fabrication for enhanced gas sensor performances.

1.2 Biomineralization and Bio-Assembly

Biomineralization is a process by which living organisms mineralize inorganic materials *in vivo*. Nacre of abalone is a well-known example of organic-inorganic composite formed by biomineralization. It is known for the high mechanical strength as a result of hierarchical assembly of layers of calcium carbonate ($CaCO_3$) crystal planes and proteins [1]. Biosilification, formation of amorphous silica (SiO_2) *in vivo*, observed in diatoms is another example of biomineralization where complex assembly of SiO_2 nanostructures is controlled by proteins [2]. Other examples include magnetic iron oxide (Fe_3O_4) nanoparticles formed in magnetotactic bacteria [3] and woven rod of enamel hydroxyapatite crystallites found in human tooth [4]. Nature's ability to form highly ordered materials at nano-, micro-, and macro-scales with application-fitted physical and mechanical properties has triggered much scientific interest.

Expanding from studies to understand and mimic biomineralization, extensive research on bio-assisted mineralization and bio-assembly has emerged. Bio-assisted mineralization is synthesis of inorganic materials from chemical precursor ions, in most cases in aqueous conditions. In comparison, bio-assembly refers to long range ordering of smaller pre-synthesized components or building blocks. Complex macroscopic biological structures have been used as a template to mineralize unique structures from chemical precursor ions. Some examples include, interwoven SnO_2 from eggshell membrane [5], porous α-Fe_2O_3/C nanocomposites from pollen grains [6], AlO_3 coating on butterfly wings [7], and porous TiO2 from wood [8]. In addition to complex structures, 1-D nanoscale biomolecules such as DNA [9], microtubule [10], peptide nanofiber [11], tobacco mosaic virus (TMV) [12], and M13 bacteriophage [13] have been employed as templates for one-dimensional (1-D) nanostructures. These templates have successfully mediated assembly and mineralization of various inorganic materials from gold [13], silver [14], palladium [12], ZnO [15], SiO_2 [16] and more. One-dimensional nanoscale biomolecules listed above have also been adapted for bio-assembly, often to form linear arrays of metal [17-20] or semiconductor [15, 21] nanocrystals for device applications.

1.3 M13 Bacteriophage

1.3.1 Background

M13 bacteriophage is a virus that belongs in the filamentous bacteriophage family with fd and f1 viruses. It is non-lethal to humans as it only infects and replicates in the *Escherichia coli* (*E.coli*) by specific recognition using its F-pilus. The M13 bacteriophage inserts its DNA into the *E.coli* and rapidly replicates using the host cell components in the non-lytic manner [22].

The wild-type M13 bacteriophage is 930 nm in length and 6.5 nm in diameter and depicted in Figure 1-1. A single-stranded circular DNA that encodes for protein sequences and length of the phage is enclosed by 5 structural proteins, pVIII, pIII, pVI, pVII and pIX, which are essential for phage structural stability. As shown in Figure 1-2, the length of phage is composed of 2700 identical copies of the α-helical major coat protein, pVIII, assembled cylindrically at five-fold symmetry. Two sets of protein coats, pIII and pVI at one end, and the pVII and pIX at the other, are present in 5 copies to cap the ends of the bacteriophage. All five coat proteins have been studied for foreign peptide display, however the most widely studied are peptide display on the N-terminal ends on the pIII and the pVIII protein coats. Phage library containing large pool of phages displaying random peptides on the protein coats have been used in combinatorial phage display technology. This technology, also known as biopanning, has been applied to study protein-protein, protein-DNA, protein-inorganic material interactions as well as for antibody and enzyme selection [23].

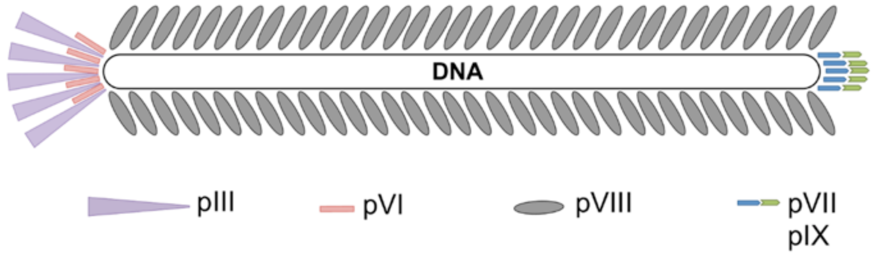

Figure 1-1 Schematic diagram of M13 bacteriophage with five structural proteins pVIII, pIII, pVI, pVII, and pIX enclosing single-stranded DNA in center.

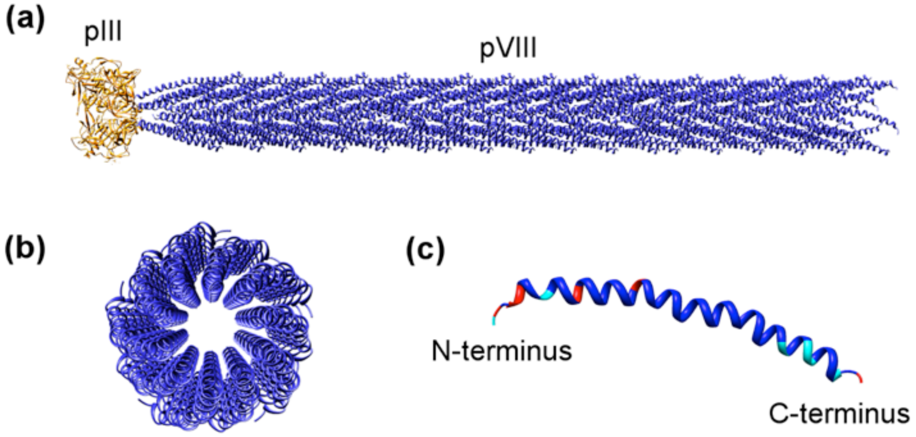

Figure 1-2 Simplified Chimera image of (a) pIII (yellow) and pVIII (blue) coat proteins displayed on its location, (b) top-down view of pVIII protein arranged in five-fold symmetry, and (c) single α-helical pVIII coat protein with amine (cyan) and carboxyl (red) side groups indicated [24].

1.3.2 pIII Phage library and peptide selection

The pIII protein coat displayed at one end of the virus is highly flexible and therefore susceptible to wide range of foreign peptides for display. Naturally, it has been used most frequently for combinatorial phage display technique and pIII phage libraries displaying 7-mer, 12-mer, and looped peptide sequences are even commercially available by New England Biolabs Inc. One major application of the pIII phage display library is selection of peptides with affinity for specific inorganic materials. By performing several rounds of the standard biopanning process, the most recurrent peptide sequence is isolated for further study. Peptides with affinity to metals (silver [14], gold [25], platinum [26]), semiconductors (GaAs [27], ZnS [21]), and metal-oxides (SiO_2 [16], ZnO [28]) have been identified and confirmed using the pIII library. Furthermore, peptides identified using the pIII phage library successfully directed crystal growth of nanomaterials including CdS [29], ZnS [30], ZnO [28, 31], to name a few, in solution or on planar substrates by acting as nucleation sites or capping agents.

1.3.3 pVIII phage library and templated inorganic assembly

As described above, the pVIII protein is highly packed and organized on the length of the M13 bacteriophage. Unlike the pIII protein coat, the genetic display of foreign peptides on pVIII protein is constrained by length (6-8 amino acids) and electrostatic charge (negative to neutral) due to incompatible capsid assembly. As a major coat protein, displayed in highest copy number, modification of the outside N-terminus of the pVIII protein coat significantly affects the phage properties. Selection of chloroform resistant phage using the pVIII library is an example of such drastic property change [32]. In addition, the pVIII library is an ideal nanoscaffold for synthesis of 1D nanomaterials with uniform length. Huang et al. identified gold-binding peptide on the pVIII coat protein and displayed binding of gold nanoparticles and progressive growth of continuous gold nanowire on the template [13]. Nam et al. and Zaman et al used electrostatic interactions of E4/E3 (-EEEE/-EEE) displaying negatively charged phage and metal ions to synthesize Co_3O_4 [20] and $Cu_{1.8}S$ [33] nanowires. Furthermore, Lee et al. reported hybrid nanowires of Co and Pt from on Co^{2+} binding phage identified from the pVIII library [34]. Likewise, the peptide display on pVIII is essential for viral-templated nanomaterial synthesis. Hence, methods to overcome capsid assembly constraint to increase diversity of displayed peptides and express desired peptides at high density are of interest.

1.4 Chemiresistive Gas Sensors

1.4.1 Background

Gas sensors are very intimately associated with our lives. Nearly every household, industrial or commercial settings has at least one type of gas sensor monitoring the gas levels of either toxic or explosive gas, humidity or odor. Gas sensors can be largely divided into three types: solid state sensors, mass sensitive sensors, and optical sensors [35]. Chemiresistive sensor is a type of solid state sensor that monitors change in resistance as the gas analyte interacts with the sensor. Amongst different types of sensors, chemiresistive sensor has a relatively simple configuration and reported for rapid response, recovery, and low cost. Nanoscale metals and metal oxides have been used as sensor materials to effectively detect common hazardous gases: SO_2, H_2S, O_3, H_2, NO_x, Cl_2, CO, NH_3. In particular the increased surface-to-volume ratio in nanomaterials provide large interactive sites, accessibility to conductive pathways, short diffusion length for rapid, sensitive gas detection.

There are several figures of merit for direct comparison and assessment of chemiresistive gas sensor performances: sensitivity, response and recovery time, detection limit, selectivity, dynamic range, and powder consumption. Out of these, sensitivity, response and recovery time, lowest detection limit are key parameters reported to quantify sensor performance in this work. Figure 1-3 is an illustration of the time vs. sensing response plot as the sensor is exposed to analyte gas. A stable baseline resistance is obtained during carrier gas flow and used as the reference to determine the response. Response, plotted on the y-axis, is the change in resistance relative to the baseline resistance (R_0):

$$\text{Response} = \frac{\Delta R}{R_0} = \frac{(R-R_0)}{R_0}$$

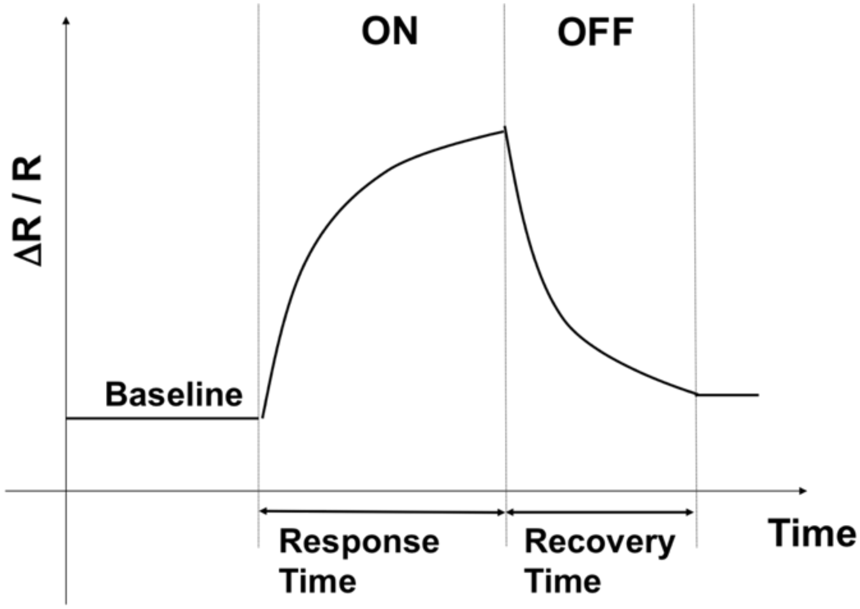

Figure 1-3 Schematic illustration of sensor response vs. time plot. Key parameters, response, response and recovery times, are labeled.

As shown in Figure 1-3, sensor-analyte interaction which cause resistance increase (in this case) is directly displayed by the response increase when the gas is “on.” In reverse, when the gas is “off,” a gradual decrease in response to the baseline is observed with analyte removal. The response and recovery times are defined as the time taken to reach 90% of the maximum (gas “on”) and minimum (gas “off”), respectively. These gas exposure and release periods are alternately tested for different analyte concentrations as well as for repeatability. Although increasing response is presented here, depending on the sensor-analyte interaction, decreasing response can be obtained simply as the reverse of this plot. A calibration curve of sensor response is shown in Figure 1-4, now displaying response relative to the analyte concentration. Here, the linear region between the lower and upper detection limit is defined as the dynamic range. The linear slope within the dynamic range determines the sensitivity of the device:

$$\text{Sensitivity (S)} = \frac{\%\ \text{Response}}{\Delta\ \text{Gas concentration}} = \frac{{}^{\Delta R}\!/_{R_0} \times 100}{\Delta\ [\text{Gas}]} = {}^{\%}\!/_{\text{ppm}}$$

Finally, the lowest detection limit, defined as 3 times the signal-to-volume ratio, can be calculated from the monitored sensor responses. Abovementioned parameters will be addressed in the following chapters and compared to other reported sensors.

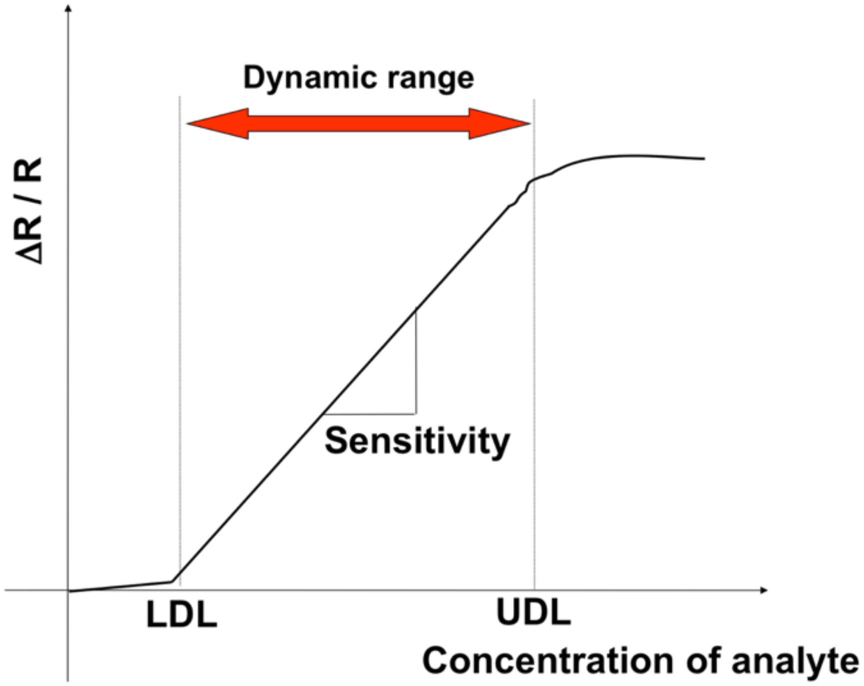

Figure 1-4 Schematic illustration of sensor calibration curve displaying response vs. concentration of gas analyte. Sensor dynamic range, lower detection limit (LDL), upper detection limit (UDL) and sensitivity are indicated according to the definition.

1.4.2 Metal-based Gas Sensor

Metal nanostructures of different morphological forms have been reported for its use in chemiresistive sensors for their fast response and low operation temperatures. The two metals discussed in this dissertation are gold (Au) and palladium (Pd). These metals have been explored as sensitizers, conductive channels, or both in chemiresistive gas sensors. Particularly, nanocrystalline metals have been reported to enhance sensor performance. When incorporated in conductive platforms such as carbon nanostructures [36-39], semiconductor materials [40-42], and conductive polymers [43, 44], metal nanocrystals functioned as analyte affinity sites or as electron donors to enhance sensor response. Furthermore, sensors based on metal nanocrystal arrays have also shown promises. Unlike bulk or single crystalline metals, the charge transport across metal nanoparticles is dominated by activated electron hopping between nearest-neighboring particles. Hence a large change in electrical conductivity is achieved even with small changes in activation energy (E_A) as shown in the equation below, where σ is conductivity, k is Boltzmann constant, and T is temperature:

$$\sigma \approx \exp\left(\frac{-E_A}{kT}\right)$$

This exponential relationship is clearly represented in metal nanoparticle-based gas sensors to significantly improve response and sensitivity of the devices.

While Au is known for its catalytic role in sensing various hazardous gases, it's particularly important as a sensitizer in hydrogen sulfide (H_2S) sensing due to its high affinity for sulfur-containing compounds. Evaporated nanocrystalline Au films [45], chains of glycine-stabilized Au nanoparticles [46], and clusters of randomly deposited citrate-coated Au nanoparticles [47] were reported as sensitive H_2S sensors. Increased resistance was observed for all these devices, in which charge transport between neighboring nanoparticles was impeded by H_2S adsorption on the Au surfaces.

Pd has been reported as an effective sensing material only for H_2 gas due to its selective interaction with H_2 to form palladium hydride (PdH_x). Upon contact with Pd, H_2 gas adsorbs and dissociates to form H atoms, which then diffuse into the interstitial sites of Pd to form alpha-phase palladium hydride (α-PdH_x) [48, 49]. At H_2 concentrations above 2%, PdH_x undergoes a phase transformation from α-phase to β-phase [48]. Based on these PdH_x phases, two main chemiresistive H_2 sensing approaches exist. The first approach uses an increase in resistance with exposure to lower concentrations of H_2 gas as Pd metal converts to more resistive PdH_x for sensing. The second approach uses the decrease in resistance caused by the closing of nanogaps due to the volumetric expansion accompanying β-PdH_x formation with exposure to H_2 gas above 2% for sensing. Pd-based H_2 sensing is heavily dependent on efficient H_2 diffusion and hence nanostructures that provide large surface area and short diffusion lengths are idea candidates. Some examples of Pd-based sensors include thin films [49-52], electrodeposited single nanowires [53-55], and nanoparticles [56, 57].

1.4.3 ZnO-based Gas Sensor

Zinc oxide (ZnO) is a self-doped n-type semiconductor that has been studied for various applications such as optoelectronic, electric, piezoelectric, phootcatalytic, and gas sensor applications. It has a wide, direct band-gap (3.2-3.4 eV), high exciton binding energy (60 meV), and high electron mobility (150-350 $cm^2 V^{-1} s^{-1}$). ZnO can form cubic zinc blende and hexagonal wurtzite crystal structures, however the latter is more stable and predominantly formed (Figure 1-5). Reports have shown ZnO sensing against several reducing gases: NH_3, NO_x, CO, and H_2S [58]. Like most semiconductor-based sensors, many ZnO-based sensors have great thermal stability and require high operation temperature for sensing, which increases energy consumption and cost [59, 60]. Hence, efforts to decrease the operation temperature by changing morphology, size, crystallinity, doping and addition of metal catalysts have been reported [61-63]. Additionally, sensors were exposed to UV or visible light that promote electron carrier generation for sensing at lower temperatures [64-66]. The large surface area provided by ZnO nanomaterials is critical for reducing gases to participate in oxidation/reduction reaction with chemisorped O^{2-} or O^- ion species. When the reducing gas adsorbs on the ZnO surface, it reduces the ionized oxygen species and transfers electron carriers to decrease electrical resistance in sensor. Furthermore, the Debye length, which is measure of electric field migration in semiconductors, is comparable to the grain or particle sizes in nanomaterials. In return, a more significant change in charge transport can be obtained. Wide range of ZnO nanowires [67], nanorods [64], nanopowder [68], as well as metal-decorated ZnO [42, 62, 69] have been studied. Moreover, enhanced sensing has been reported with additional surface and sub-gap defects that act as adsorption sites and electron carrier donors [70, 71] and for catalysis via visible light exposures [66].

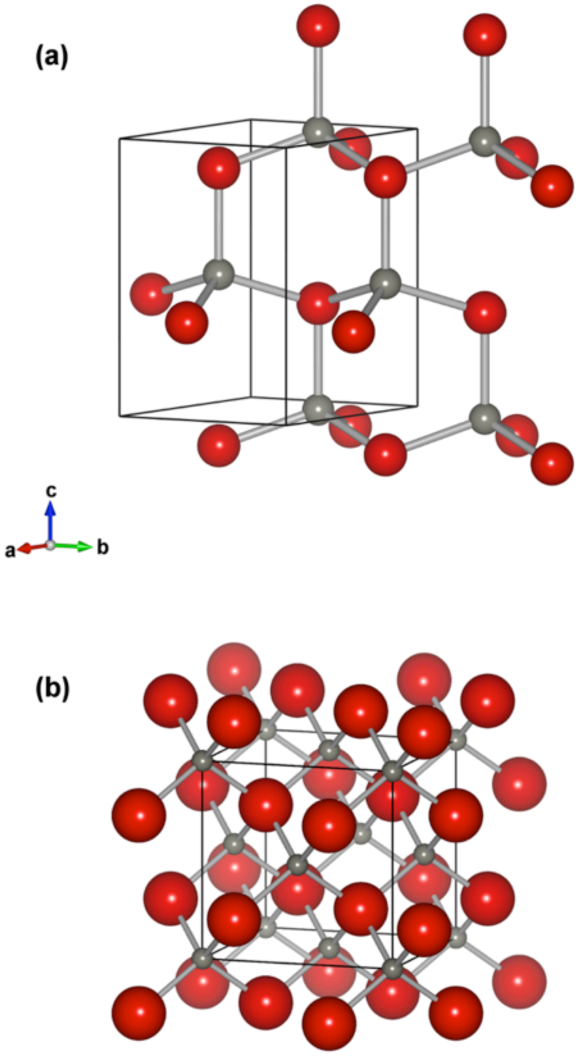

Figure 1-5 Zinc oxide (ZnO) (a) wurtzite and (b) zinc blende crystal structures displaying single unit cell (created by software VESTA) [72]. Zinc and oxygen atoms are colored in gray and red, respectively.

1.5 Scope of Work

This dissertation focuses on synthesis and assembly of inorganic nanomaterials from bio-directed technique for gas sensor applications. Bottom-up assembly of inorganics from M13 bacteriophage and its protein/peptide components formed intricate nanoscale materials for added functionality and improvements in gas sensing performance.

Chapter 2 discusses design and fabrication of viral-templated continuous gold nanoparticle chains for highly sensitive H_2S gas senor. Gold-specific M13 bacteriophage functioned as template and sensing material for detection of sub-ppb level H_2S gas at room temperature. Furthermore, in Chapter 3, gold-palladium peapod nanostructures are developed on the platform of gold nanoparticle chains-based devices. Here, H_2 sensing dependence on Pd shell thickness is presented.

The next chapters present development of ZnO synthesis methods on M13 bacteriophage components for future gas sensor studies. In Chapter 4, ZnO mineralization on pIII and pVIII protein coats each displaying previously reported 12-mer peptide genetically and chemically, respectively, is presented. Chapter 5, focuses on ZnO synthesis and characterization of M13 bacteriophage selected 8-mer peptide-directed materials. The peptide controlled morphological and optical characteristics, regulating sub-gap defect levels in the materials. Photoluminescence and photocurrent measurements were made to assess the potential use of these ZnO nanomaterials for light-assisted gas sensing.

Chapter 2. Nanocrystalline Gold-Based H_2S Gas Sensor

2.1 Introduction

Hydrogen sulfide (H_2S) is a toxic gas released in petroleum, mining, paper, and water treatment industries [73]. Although low concentrations of H_2S, below 5 ppm, are innocuous, slightly higher concentrations, near 20 ppm, can cause eye and respiratory tract irritation. Furthermore, H_2S concentrations at or above 100 ppm are considered Immediately Dangerous to Life and Health (IDLH), and may cause paralysis and even death [74, 75]. To minimize occupational health hazards, H_2S gas levels must be monitored continuously. In particular, compact, low power consumption sensors with high sensitivity and low detection limit for personal exposure and mobile monitoring applications are highly desirable.

Nanostructured materials with high surface area-to-volume ratios are good candidates for chemiresistive gas sensors that address these needs. These materials facilitate interaction with analytes and support significant changes in electrical resistance due to analyte surface adsorption/desorption, with minimal power expenditure and a reduced device footprint. H_2S gas sensors have been assembled from a variety of nanostructured metals and metal oxides [46, 47, 58, 76, 77]. Gold has received specific attention because its strong affinity for sulfur-containing compounds can be used to impart sensor selectivity [78-80]. Gold nanostructures, assembled with various methods, have been investigated both as sensitizers for other materials and as independent building blocks to fabricate H_2S gas sensors. For example, for H_2S detection, electrochemical deposition has been used to attach gold nanoparticles to carbon [36, 37] and polyaniline nanotubes [43]; sputtering has also been used to create discontinuous nanoscale gold films on carbon nanotubes [38] and 1-pyrenesulfonic acid-coated templates have been used to synthesize gold nanoparticles and nanowires on the surface of carbon nanotubes [81]. Additionally, gold-based H_2S sensors have been assembled directly from thermally evaporated nanocrystalline gold films [45], thick chains of electrophoretically-assembled glycine-stabilized gold nanoparticles [46], and clusters of randomly deposited citrate-coated gold nanoparticles [47]. Moreover, some of these gold-based and gold-functionalized devices report room temperature operation [37, 43, 46, 81] a condition which significantly reduces power consumption and is generally not feasible for metal oxide-based H_2S sensors.

Biological materials with nanoscale, hierarchical structures advantageous for gas sensing provide an alternative route to nanostructured material synthesis [6, 60, 82, 83]. Fibrous matrices of eggshells [84], quasi-honeycomb structures of butterfly wings [85], and reticulated porous networks of wood [86] have been used to template solution-based synthesis of SnO_2, α-Fe_2O_3, and ZnO, respectively. Not readily attainable with conventional fabrication or synthesis methods, these novel architectures with high surface area-to-volume ratios were found to be useful for chemiresistive H_2S gas sensors at elevated operation temperatures following calcination to remove the biological template [84-86].

In this chapter, viral-templated gold nanowire H_2S gas sensors were demonstrated. A gold-binding M13 filamentous bacteriophage, approximately 6-7 nm in diameter and 930 nm in length [13, 23], was used to template nanocrystalline gold. The high aspect ratio M13 virus has been used successfully to template numerous inorganic nanowires and nanowires assemblies, as well as for the fabrication of a range of device architectures [87-89]. These one-dimensional biological structures were well-suited for nanowire-based H_2S gas sensor formation. Unlike previous bio-templated H_2S sensors [84-86], the viral template was designed with specific affinity for the inorganic sensor material and the template was not removed prior to gas detection. The 2700 copies of gold specific 8-mer peptide displayed on the length of the virus not only functioned as selective binding sites, but were also integral sensor components necessary for sensitive and effective H_2S sensing at low ppb levels. To our knowledge, this is the first report of bio-templated, room temperature H_2S gas sensors in which the template contributes more than simple geometry to sensing performance. These studies reveal the promise of biologically-directed synthesis for simple fabrication of highly sensitive, nanostructured gas sensors.

2.2 Experimental details

2.2.1 Assembly of viral-templated gold nanowire gas sensors

As depicted in Figure 2-1 (a-d), to form H_2S gas sensors, bio-templated gold nanowires were assembled on electrodes fabricated on a Si/SiO_2 substrate using a modification of a previously reported procedure [90, 91]. A gold-binding [13] M13 bacteriophage was used as the template. This particular clone displayed an 8-mer peptide (VSGSSPDS) with an affinity for gold on the N-terminus of each of 2700 copies of the pVIII major coat protein [13, 34]. The 300 nm thermal oxide layer electrically insulated the viral-templated nanowires from the underlying Si substrate. The Ti/Au (20 nm/180 nm) electrodes, which were 50 μm wide and separated by a 3 μm gap, were fabricated using standard photolithography, electron beam deposition, and lift-off techniques. Prior to nanowire assembly, the substrates with patterned electrodes were solvent cleaned with ultrasonication in acetone, isopropanol, and deionized water and activated with O_2 plasma using a reactive ion etching (RIE, Surface Technology Systems) system at 100 W, 100 mT for 30 sec. This plasma treatment was critical for uniform and non-specific adhesion of the viral template to the patterned substrates. The pre-patterned substrates were then incubated with gold-binding phage in tris-buffered saline (TBS, 50 mM Tris-HCl, 150 mM NaCl, pH 7.5) for 10 min. During this step, the gold-binding phages were adsorbed onto the substrate. The substrate was then washed and rinsed in TBS with 0.7% Tween-20 (TBST) and deionized water. To control the density of phage on the substrate surface, and ultimately the number of parallel electrical connections between the electrodes, samples were made with three different phage concentrations: 1×10^8 pfu/μL, 3×10^8 pfu/μL, and 5×10^8 pfu/μL. Gold nanoparticles were selectively bound to the gold-binding phage by submerging the substrate in a 5 nm diameter gold colloid solution of $5\text{x}10^{13}$ particles/mL (BBI Solutions.) for 1 hr. The substrate was rinsed 3 times with deionized water and gently dried with air. The nanoparticles bound to the phages were used as seeds for electroless deposition of gold using Nanoprobes GoldEnhance™ LM solutions. The electroless deposition time was varied from 3 to 12 min to control the nanoparticle size and electrical resistance of the gold nanowires formed. The viral-templated gold nanowire devices are hereafter referred to as "as-assembled" devices. As-assembled devices were treated with O_2 plasma for 30 sec at 100 mT and 100 W using the RIE system, dipped in ethanol (Sigma-Aldrich) for 10 min, and gently blown dry with air. This two-step process removed the viral template and surface organics, as well as Au_2O_3 which may have been generated by exposure to O_2 plasma [92, 93]. These devices will hereafter be referred to as "ethanol-treated" devices and were used to evaluate the contribution of the viral-template to device resistance and sensing performance.

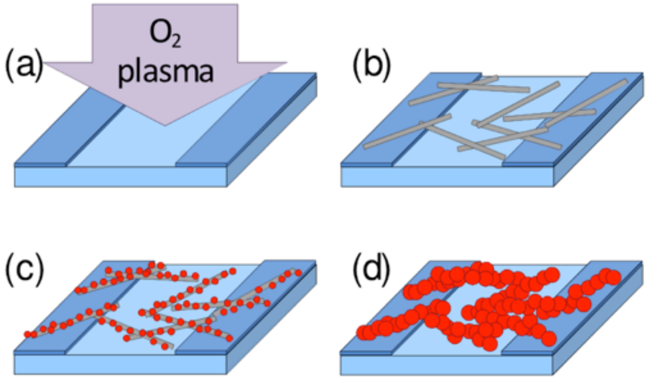

Figure 2-1 Schematic representation of the sensor fabrication process for as-assembled devices. (a) O_2 plasma treatment of pre-patterned gold electrodes to enhance surface hydrophilicity. (b) Non-specific adsorption of gold-binding phage on the patterned substrate. (c) Specific binding of 5 nm gold nanoparticles to the pVIII coat protein of the gold-binding phages. (d) Nanocrystalline gold nanowires formed through seeded, electroless deposition.

2.2.2 Morphological characterization

Scanning electron microscopy (SEM, Phillips XL30 FEG) was used to determine the morphology and spatial distribution of the gold nanowires on the substrate. The number of seed particles per phage was quantified. A short electroless deposition of 1 min was used to slightly enlarge the gold nanoparticle seeds without merging them, making them easier to observe with SEM. The particles on 15 individual templates were counted for range and average. In addition, the areal fill factors of viral-templated gold nanowires on the Si/SiO_2 substrate were determined for devices assembled with phage concentrations of $1x10^8$ pfu/μL, $3x10^8$ pfu/μL, and $5x10^8$ pfu/μL. For each concentration, a minimum of 10 locations were imaged and analyzed. Furthermore, the width of the gold nanocrystal components of the viral-templated nanowires was measured at various electroless deposition times. Approximately 100 gold nanoparticles were analyzed for each electroless deposition time. Transmission electron microscopy (TEM, Phillips Tecnai 12) was used to analyze the morphology and connection between the nanoparticles within the gold nanowires. For TEM sample preparation, gold nanowires were fabricated on unpatterned SiO_2 substrates and dispersed in deionized water by ultrasonication. The dispersed nanowires were then loaded onto carbon-coated copper grids and dried in vacuum.

2.2.3 Resistance measurements

The room temperature resistance of each as-assembled viral-templated gold nanowire device was determined using two-terminal, current-voltage (I-V) measurements in which the current was recorded as the applied voltage was swept from -0.3 V to 0.3 V (Keithley 2636A sourcemeter) in 30 mV increments. The same procedure was used to measure device resistance after ethanol treatment.

2.2.4 Sensor performance analysis

Devices selected for gas sensor measurements were wire-bonded (West-bond Inc. 7499D) at room temperature to a copper printed circuit board (PCB) with 1% Si/Al wire before sensing analysis. Wire-bonded sensors were placed in a flow cell chamber with a gas inlet and outlet. A constant bias of 0.15 V was applied to each device and, after establishing a stable baseline resistance, sensing analysis was performed at ambient temperature and pressure under a constant flow rate of 200 sccm. The resistance change of each viral-templated gold nanowire sensor was measured with exposure to H_2S gas. To vary analyte concentration, H_2S gas was diluted using dry air as the carrier gas and each sensor was alternately exposed to H_2S gas at the specified concentration and dry air for time intervals of 15 min and 30 min, respectively. A mass flow controller with LabView interface was used to control the H_2S concentration and exposure time. A similar procedure was followed for selectivity analysis using NH_3 and NO_2 as the gas analytes.

2.3 Results and discussion

2.3.1 Morphological characteristics of nanocrystalline gold nanowires

The morphology of the viral-templated gold nanowires which comprise the sensors was examined with SEM to study the effect of electroless deposition time and phage concentration on the as-assembled gold nanowires. A representative image of a sensor assembled with a phage concentration of 1×10^8 pfu/μL and an electroless deposition time of 3 min is shown in Figure 2-2 (a). Gold nanowires slightly less than 1 micron in length, composed of well-defined nanoparticles were seen randomly distributed on the substrate in addition to a few individual gold nanoparticles. The number of isolated nanoparticles was small in comparison to those incorporated in the nanowires. As shown in the high magnification SEM image in Figure 2-2 (b), the width and connectivity varied along individual nanowires, as well as from nanowire to nanowire. Further SEM analysis revealed that the number of gold nanoparticle seeds per template ranged from 31 to 61 with an average of 42. We, therefore, attributed the largest deviations in nanowire width and connectivity to differences in the density and arrangement of gold nanoparticle seeds along the gold-binding phage prior to electroless gold deposition. The size and morphological changes, which accompanied increased electroless deposition time, can be seen in Figure 2-2 (b, c, d). As the electroless deposition time increased from 3 to 12 min, the overall width and connectivity of the gold nanowires also increased. The average width of the resulting nanocrystals on nanowires for 3, 7, and 12 min of gold deposition were 29±7 nm, 60±13 nm, and 82±16 nm, respectively. No difference in the morphology, structure, or distribution of nanowires on the substrate surface was observed with SEM after template removal by ethanol treatment as shown in the Figure 2-3. The TEM image in Figure 2-4 revealed the detailed structure of the nanowires. Mostly shorter fragments (< 200 nm) of nanowires were observed with TEM. This is likely because the fragile nanowires were fractured during sample preparation. The nanoparticles within the nanowires were polydisperse. Both single chain and multi-chain nanoparticle arrangements were observed. At higher magnifications near-point-contact connections between nanoparticles that, in many cases, structurally and electrically held the viral-templated gold nanowires together were observed.

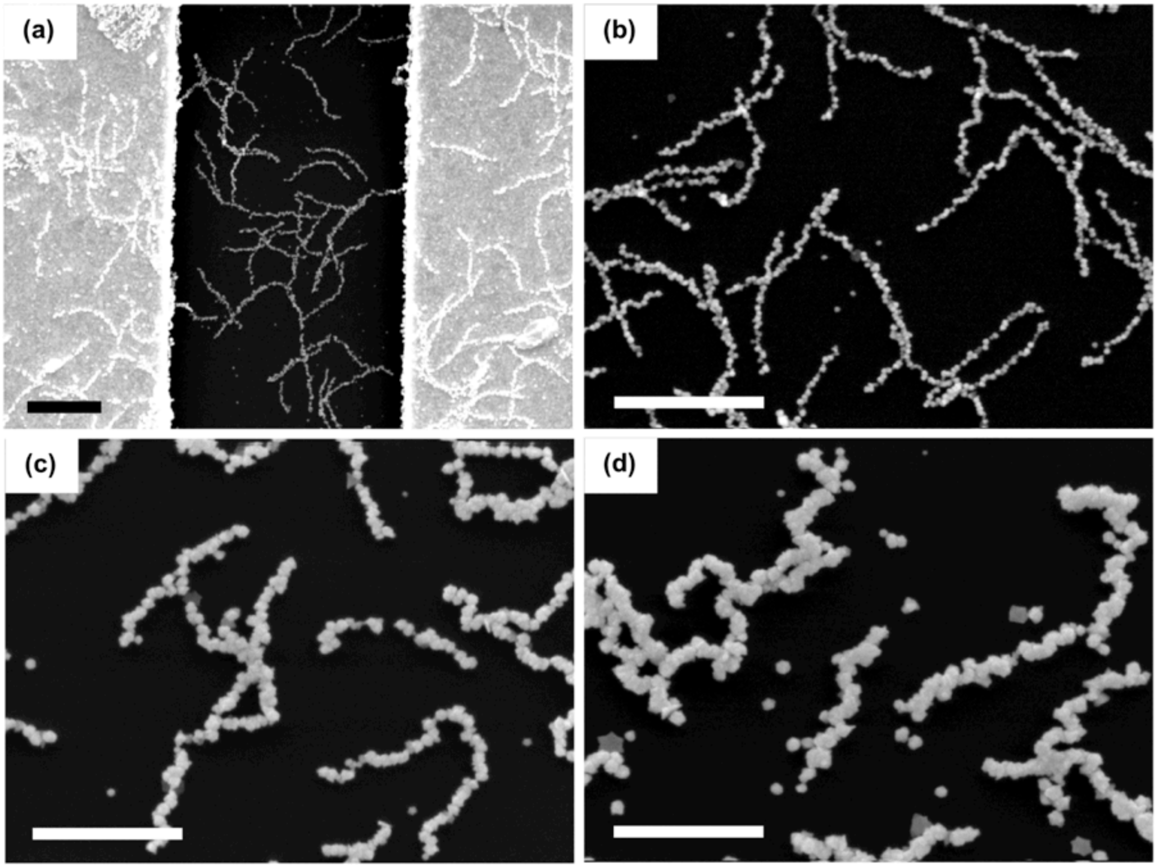

Figure 2-2 Morphology of viral-templated gold nanowires within fabricated devices assembled with a 1x10^8 pfu/μL phage concentration and a range of electroless deposition times. (a) Low magnification SEM image that shows viral-templated gold nanowires with a 3 min electroless deposition time on 50 μm electrode and across 3 μm gap. Scale bar is 1 μm. High magnification SEM images of viral-templated gold nanowires with electroless deposition times of (b) 3 min, (c) 7 min, and (d) 12 min. Gold nanoparticles are assembled in a bead-like nanowire form with increasing nanowire widths corresponding to increasing electroless deposition time. Scale bars are 1 μm.

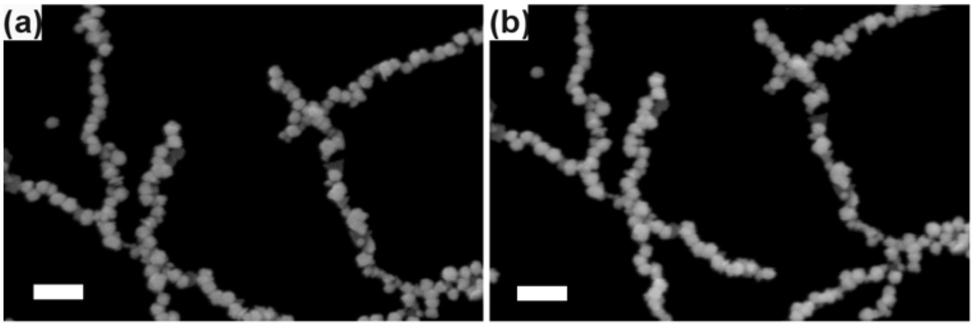

Figure 2-3 High magnification scanning electron microscopy (SEM) image of viral-templated gold nanowires. Viral-templated gold nanowires in an (a) as-assembled device in which the viral template was intact and (b) the same device and location following an ethanol treatment in which the template was removed. Scale bars are 200 nm.

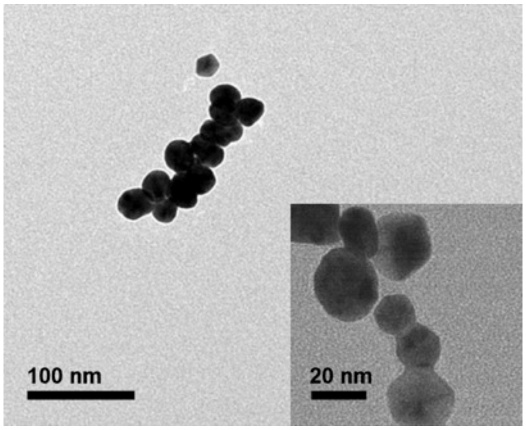

Figure 2-4 Morphology and connectivity of viral-templated gold nanowires. TEM image shows a fragment of a viral-templated gold nanowire that was removed from the substrate with ultrasonication. Scale bar is 100 nm. High magnification TEM image (inset) shows fused, polydisperse gold nanoparticles within a different nanowire fragment. Scale bar is 20 nm.

Figure 2-5 (a-c) show SEM images of the viral-templated gold nanowire sensors fabricated with increasing phage concentration and an electroless deposition time of 3 min. Phage concentrations of 1×10^8 pfu/μL, 3×10^8 pfu/μL, and 5×10^8 pfu/μL yielded devices with an average gold nanowire surface coverage of 16%, 39%, and 49%, respectively. At a phage concentration of 1×10^8 pfu/μL both isolated and small clusters of nanowires were observed within the 3 μm gap between the electrodes. At higher phage concentrations, 3×10^8 pfu/μL and 5×10^8 pfu/μL, gold nanowires formed a continuous, mesh-like structure between the electrodes. Given the relative size of the gold nanowires and electrode gap, multiple nanowires were required to physically bridge the gap between the two electrodes. As a result, a lower density of complete, physical connections was observed for the 1×10^8 pfu/μL phage concentration, as compared to the 3×10^8 pfu/μL and 5×10^8 pfu/μL phage concentrations.

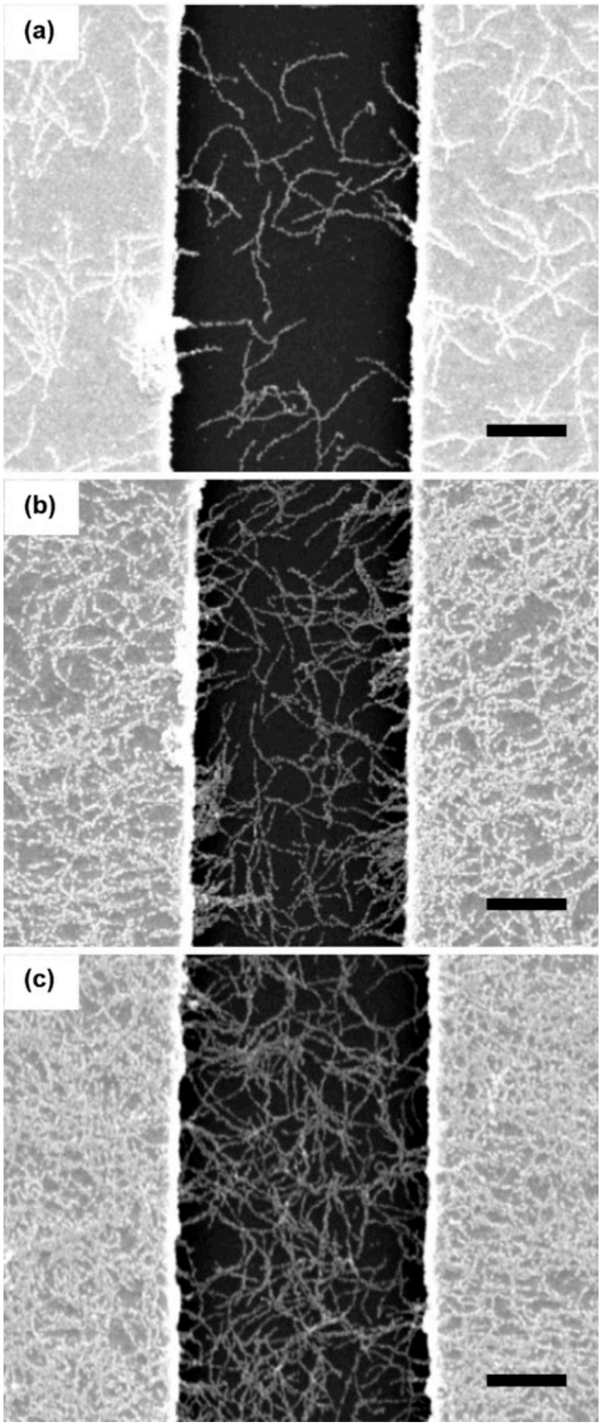

Figure 2-5 Dependence of gold nanowire surface coverage on phage template concentration. SEM images of gold nanowire devices assembled with phage concentrations (a) $1x10^8$ pfu/μL, (b) $3x10^8$ pfu/μL, (c) $5x10^8$ pfu/μL and a 3 min electroless deposition time. Scale bars are 1 μm.

2.3.2 Electrical characteristics of viral-templated gold nanowire devices

The effects of electroless deposition time and phage concentration on sensor resistance were studied. Devices displayed Ohmic behavior within the -0.3 V and 0.3 V two-terminal measurement range at room temperature for all conditions investigated. Viral-templated sensor resistance is shown as a function of gold deposition time in Figure 2-6 (a) along with the device yield for each condition. Device yield is defined as the ratio of devices with measureable resistance (less than 10 GΩ) to the total number of devices fabricated. The sensor resistance decreased as the electroless deposition time increased, which is consistent with a previous report [90]. As evidenced by SEM analysis, at longer times more gold was deposited on the nanoparticle seeds resulting in more continuous, thicker nanowires. We attribute the increase in percentage yield to the increased physical continuity of the nanowires. Furthermore, we ascribe the reduced device resistance to the increase in cross-sectional area of the nanowires, in addition to the enhanced continuity caused by deposition. At all deposition times, the device-to-device resistance varies by 1 to 4 orders of magnitude. The large range of resistances observed at a given deposition time is attributed to the previously mentioned variations in nanowire thickness and connectivity associated with differences in density and arrangement of gold nanoparticle seeds along the gold-binding phage.

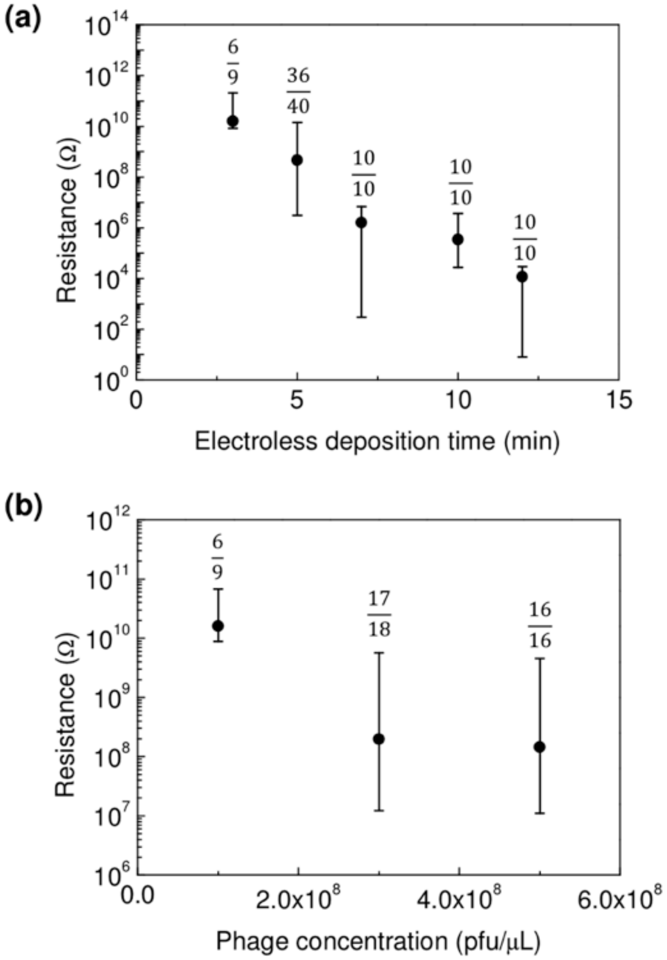

Figure 2-6 Dependence of electrical behavior of gold nanowire devices on electroless deposition time and phage concentration. The device yield associated with each assembly condition is written above the relevant data. Median resistances of the devices with maximum and minimum values are shown as a function of (a) electroless deposition time and (b) phage concentration.

As expected, the phage concentration also influenced sensor resistance. The median resistances for devices assembled with phage concentrations of 1x10^8 pfu/μL, 3x10^8 pfu/μL, and 5x10^8 pfu/μL and an electroless deposition of 3 min is shown in Figure 2-6 (b), in addition to the device yield at each concentration. As the concentration of phage increased, the median device resistance decreased. As previously discussed, the morphology of the sensors varies greatly with phage concentration. A low concentration of phage ($1x10^8$ pfu/μL) resulted in devices with nanowires that produced relatively few physical connections bridging the electrode gap and higher concentrations of phage ($3x10^8$ pfu/μL and $5x10^8$ pfu/μL) produced a fairly dense and continuous network of gold nanowires across the entire gap. As the gold nanowire density increased the number of available conductive pathways also increased, causing the overall sensor resistance to be reduced. Furthermore, the reduced yield at the low concentration was attributed the low probability of creating a physical connection between the two electrodes. To briefly evaluate the stability of the as-assembled devices the resistance was re-measured after storage under ambient conditions for 4-5 months. The resistance of all re-measured devices increased, most by no more than a few percent but a handful by as much as an order of magnitude. More studies are required to explore the cause of the resistance change and the source of device-to-device variations.

To better understand the impact of the phage template and surface organics on sensor resistance, two-terminal measurements were also performed on ethanol-treated devices. Resistance distributions of as-assembled and ethanol-treated sensors fabricated using a $3x10^8$ pfu/μL phage concentration and 3 min electroless deposition are shown in Figure 2-7. As previously discussed, a large distribution of resistances was observed in the as-assembled devices with the peak of the distribution between 10^8 and 10^9 Ω. Following ethanol treatment the distribution remained broad; however the peak resistance decreased to 10-100 Ω. Nonconductive organic ligands act as energy barriers to charge transport via electron hopping in metal nanoparticle films and chains, often resulting in highly resistive materials [17, 94, 95]. The large decrease in resistance observed in ethanol-treated sensors was attributed to the removal of organic components such as peptides and viral template from gold nanoparticle surfaces resulting in reduced nanoparticle-to-nanoparticle energy barriers and enhanced charge transport [95-97].

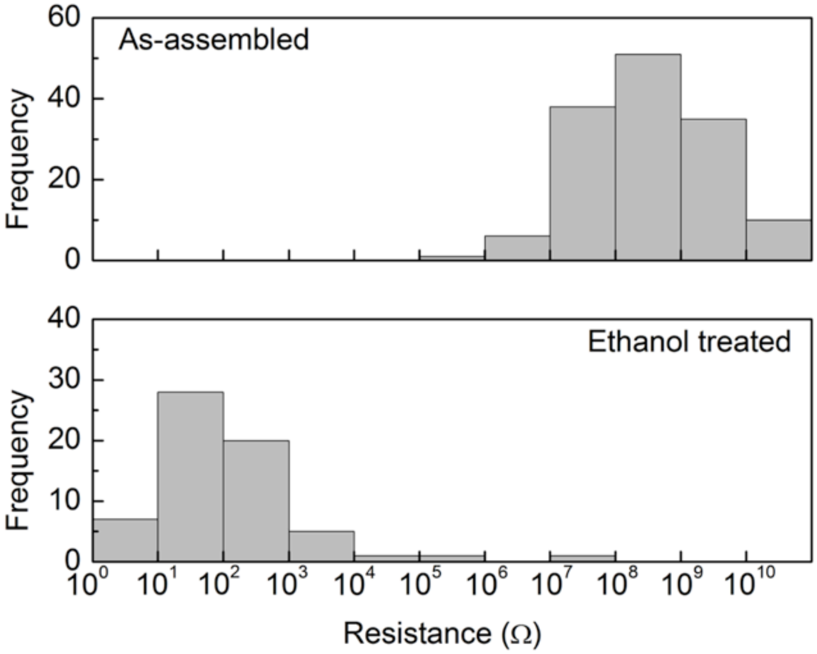

Figure 2-7 Histograms of resistances for as-assembled and ethanol-treated devices fabricated using a 3×10^8 pfu/μL phage concentration and 3 min electroless deposition.

2.3.3 Sensing performance of viral-templated gold nanowire devices

A characteristic real-time sensing response, defined as the change in resistance relative to the baseline resistance ($\Delta R/R_0$), and a calibration curve with respect to gas concentration for as-assembled gold nanowire sensors are represented in Figure 2-8 (a) and (c). These devices were assembled with a phage concentration of 3×10^8 pfu/μL and electroless deposition time of 3 min. After exposure to dry air flow for 5 hrs with constant bias applied, a stable resistance baseline was established for each device. However, within the first minute the resistance dropped sharply and then continued to slowly decline; by 10 minutes of dry air flow, all devices were stable with less than 5% change in resistance over time. Sensor resistance increased with exposure to H_2S concentrations ranging from 0.025 ppm to 0.5 ppm. This chemiresistive behavior was consistent with other reports of H_2S sensors composed of gold NP chains [46, 47, 81], and films [45] in which charge transport between neighboring nanoparticles or nanocrystals is impeded by adsorption of H_2S onto the gold surface causing resistance to increase. The sensitivity, defined as the slope of the linear region on the calibration curve, was 654%/ppm, within the linear range from 0 to 0.025 ppm. This sensitivity is more than an order of magnitude greater than other gold-based room temperature H_2S sensors [37, 45, 46]. Saturation of sensor response was observed at concentrations above 0.025 ppm. The lowest detection limit, defined as the concentration at which the response is 3 times the signal-to-noise ratio, was 2 ppb. This value is lower than that achieved by H_2S sensors composed of electrophoretically-assembled glycine-stabilized gold nanoparticles [46] and gold nanoparticles on 1-pyrenesulfonic acid-coated carbon nanotube templates [81], and comparable to the 3 ppb limit reported for sensors assembled from carbon nanotubes decorated with electrochemically deposited gold [37]. The response and recovery times, which are defined as the time to reach 95% of saturation resistance and the time for resistance to recover to 10% above the baseline resistance, were greater than 15 min and 30 min, respectively. Seventy percent recovery was observed within 30 min for all as-assembled devices, indicating desorption of the gas analytes from the surface. Faster recovery was observed with exposure to lower analyte concentrations such that devices exposed to 0.025 ppm H_2S experienced up to 70% recovery within 9 min. The sensors exhibited some cross-sensitivity to NH_3 and NO_2, toxic gases which are also frequently present in water treatment and mining industries. Figure 2-9 shows the response of the devices to 0.5 ppm of H_2S, NH_3 and NO_2.

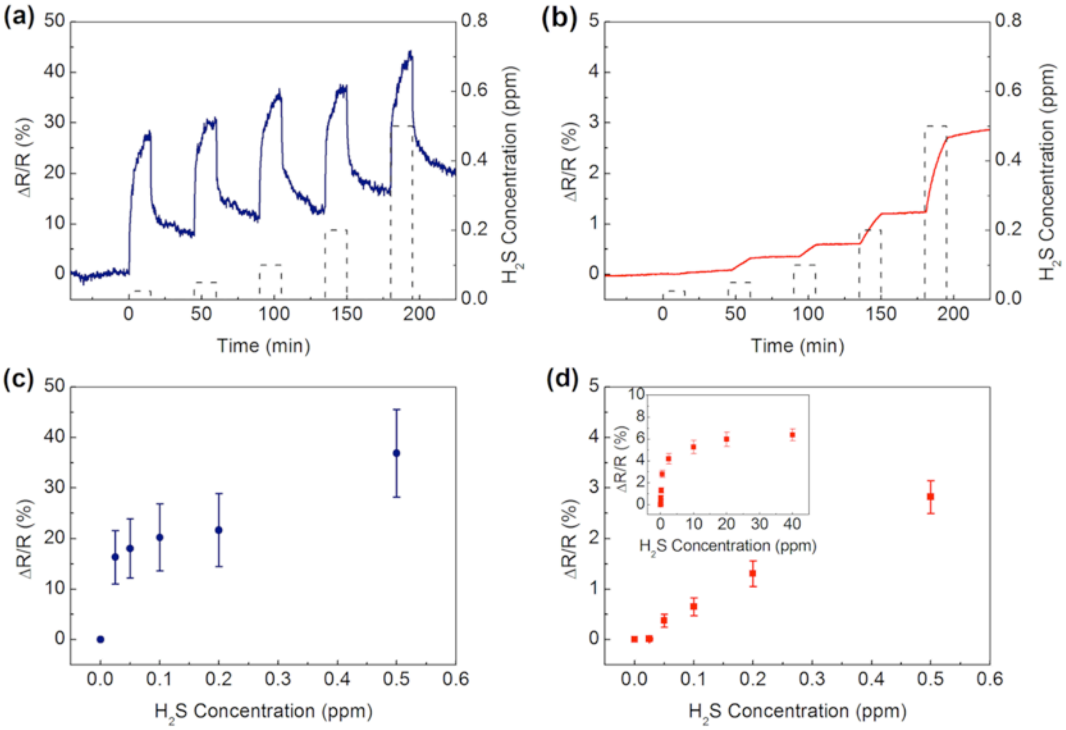

Figure 2-8 Representative room temperature H_2S sensing behavior of (a) as-assembled and (b) ethanol-treated viral-templated gold nanowire devices. Sensors were alternately exposed to H_2S and dry air for intervals of 15 and 30 min, respectively. Dashed line indicates the H_2S concentration to which the sensors were exposed at each time. Calibration curve of (c) as-assembled and (d) ethanol-treated sensors showing sensor response to H_2S concentrations between 0 and 0.5 ppm. Inset in (d) shows calibration curve of ethanol-treated devices for H_2S concentrations between 0 and 40 ppm.

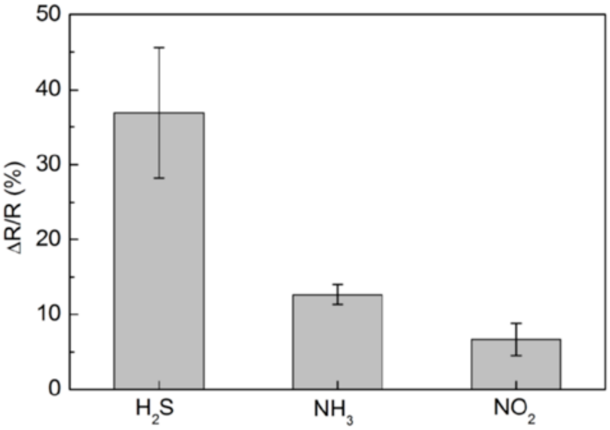

Figure 2-9 Sensing response of viral-templated gold nanowire sensors to exposure to 0.5 ppm of H_2S, NH_3, and NO_2 gases.

To highlight the importance of the gold-binding peptides and viral template on device behavior, the sensing performance of ethanol-treated devices, in which organics were removed, was also analyzed. A characteristic real-time sensing response and a calibration curve for ethanol-treated gold nanowire sensors are shown in Figure 2-8 (b) and (d). Ethanol-treated devices increased in resistance with exposure to H_2S concentrations ranging from 0.025 ppm to 40 ppm. These sensors maintained a linear response up to 0.5 ppm with a sensitivity of 6%/ppm, and a 6 ppb lower limit of detection. Like the as-assembled sensors, response times were greater than 15 min; however, a considerably slower initial response rate was observed for the ethanol-treated than for the as-assembled devices. No recovery was observed in these sensors. This irreversible behavior suggests the continued presence of analyte on the gold nanowire sensor surface. Similar behaviors have been reported at room temperature for H_2S

sensors based on ligand-free gold thin films [45] and citrate-coated gold nanoparticles [47, 81], due to strong Au-S affinity. Recovery was only attained in these devices at temperatures >140°C. Table 2-1 summarizes the sensing performance of these viral-templated nanowire devices and provides a comparison to other gold nanoparticle-based chemiresistive H_2S sensors.

The sensing behaviors of as-assembled and ethanol-treated sensors were notably different. As-assembled devices, in which the viral template and gold-binding peptides were intact, exhibited a slightly decreased lower detection limit (3x), decreased dynamic range (20x), and a substantial sensitivity increase (100x) compared to ethanol-treated devices. Moreover, the analyte adsorption and desorption rates of the as-assembled sensors were markedly faster than the ethanol-treated sensors. This behavior suggests that, although the viral template with the gold-binding peptide was intended primarily for structural assembly of nanowires, it also played an active role in device-analyte interaction.

Biological molecules incorporate a range of chemical moieties which enable extraordinary diversity and specificity for in vivo processes. These same attributes have proven useful in discrete sensor and electronic nose applications. Biological molecules including proteins [98, 99], peptides [100-102], antibodies [103], and DNA [104] have been successfully integrated into gas or vapor phase sensors to impart analyte specificity. Of particular relevance to these studies is the use of peptides. For example, piezoelectric-based sensors have utilized molecular modeling in conjunction with oligopeptide mimics of human olfactory [99] and dioxin [100] receptors to detect vapor phase acetic acid [99], ammonia [99], and dioxin [100]. The same oligopeptides have also been used to sensitize silicon nanowire-based chemiresistive sensors [102]. Furthermore, peptides identified with a combinatorial phage display library [105], in a process very similar to that used to select the gold-binding peptide found in these studies, have been used for detection of trinitrotoluene (TNT) with both fluorescence quenching [106] and conductance-based field effect transistor (FET) [107] device platforms. In the former, the entire virus with high copy peptide fusions was incorporated into the device [106]. Indirect evidence exists that, indeed, the gold-binding peptide may have an affinity for sulfur found in H_2S gas. Specifically, the pVIII major coat protein of the unmodified or wild-type M13 virus has been recently reported to display an affinity for sulfur [108]. The carboxyl groups associated with acidic amino acids such as aspartate (D) and glutamate (E) found within the wild-type pVIII coat donate electrons to sulfur, creating S-O and C-S bonds [108]. Like the wild-type M13, the gold-binding phage template displays acidic amino acid (aspartate, D) on its pVIII coat and may, therefore, share this attraction to the H_2S analyte, potentially increasing device sensitivity and response rate. In addition, amine groups have demonstrated an affinity for H_2S [109-111]. Each of 2700 copies of the pVIII protein found along the length of the viral template is terminated with an amine group, which may again cause increased sensitivity and enhanced response rate. Moreover, very rapid initial response rates were observed in H_2S sensors fabricated from glycine-stabilized gold nanoparticles on which amine groups were also displayed [46].

Alternatively, the gold-binding peptide fusion and/or phage template may interact with the H_2S analyte or its decomposed, adsorbed products without exhibiting a specific affinity. The gold-binding phage template displays an 8-mer peptide known to preferentially bind to and reduce gold in solution [13]. Specifically, hydroxyl-containing amino acids such as serine (S) can act as anchoring sites for peptide adsorption to Au surfaces [13, 112, 113]. The presence of the high affinity gold-binding peptide, rich in serine (S), on the surface of the as-assembled devices, may sterically hinder or decrease available adsorption sites and weaken analyte binding to the gold surface resulting in reduced dynamic range and enabling device recovery. As described here, a few potential mechanisms, which may act alone or in combination, could account for the active role of the viral template within the H_2S sensor. Yet, further studies are necessary to fully understand the function of the viral-template and gold-binding peptides in sensor performance, as well as in adsorption and desorption kinetics.

Table 2-1 Chart to compare sensor performance of gold nanoparticle-based H_2S chemiresistive sensors. Work described in this chapter in bold.

Device	Lowest detection limit (ppb)	Sensitivity (%/ppm)	Response time at lowest conc. (min)	Recovery time (min)	Reference
Gold nanoparticle on SWNT	3	70	6-8	10	[37]
Viral-templated nanocrystalline gold	**2**	**654**	**> 15**	**> 30**	**[114]**
Gold nanoparticles on PANI	0.1	13780	2	5	[43]
Gold nanoparticles On SWNT	50	-	> 5	No recovery	[81]
Thin gold film	120	-	10	No recovery	[45]
Dielectrophoresis gold nanoparticles	250	29.84	25 sec	2.5	[46]

2.4 Conclusion

We have demonstrated viral-directed assembly of very sensitive, nanocrystalline gold H_2S gas sensors which operate at room temperature. The M13 bacteriophage template enabled facile control over device morphology, creating discrete nanowires from chains of gold nanoparticles. Electroless deposition time and phage concentration were used to adjust individual nanowire width and connectivity, as well as to manipulate the nanowire surface coverage of the device. Increased nanowire width, connectivity, and surface coverage decreased sensor resistance. As-assembled viral-templated gold nanowire sensors with template and binding peptides intact, exhibited high sensitivity near 650 %/ppm, a very low limit of detection of 2 ppb, and 70% recovery within 9 min for 0.025 ppm H_2S. Upon removal of the viral template and binding peptides using O_2 plasma treatment and an ethanol dip, sensor resistance dropped by several orders of magnitude, the limit of detection increased, and sensitivity fell by more than a factor of 100. Furthermore, the initial rate of sensor response to H_2S exposure was substantially reduced and recovery was lost. The presence of the bacteriophage template and gold-binding peptide clearly plays a sizeable role in device resistance and is critical to H_2S sensing. Bio-templated materials not only have the potential to generate high surface area-to-volume nanostructured architectures desirable for gas sensing, but may exhibit additional functionality which facilitates and even enhances device performance.

Chapter 3. Gold-Palladium Nanopeapod H_2 Sensor

3.1 Introduction

Hydrogen (H_2), a zero-emission energy source, has long been recognized as a promising alternative to fossil fuels, yet technological hurdles remain. This colorless and odorless gas is extremely reactive with oxygen and explosive in air above 4 vol. %, necessitating specialized safety consideration. Specifically, to diminish risk aboard vehicles and in home or industrial settings, early leak detection is critical. For safe and effective use of H_2 as a fuel, highly sensitive sensors that rapidly detect low concentrations of H_2 gas are in demand.

Nanostructured, palladium (Pd)-based chemiresistive H_2 sensors are a sensitive and selective sensing option. Pd thin films [49-52], electrodeposited single nanowires [53, 55, 115], nanotubes [56], and nanoparticles [57, 116] are some examples of nanomaterials which have been used in this capacity. H_2 gas adsorbs to the surface and grain boundaries of Pd, dissociates, and diffuses into the lattice to form palladium hydride (PdH_x). The presence of hydrogen (H) within the lattice increases electron scattering sites, increasing bulk electrical resistivity. Additionally, H decreases the work function of Pd, which can impede electrical transport between Pd grains and across junctions with other materials [48, 49]. Furthermore, as H is incorporated within the Pd lattice, a volume expansion occurs which is amplified at high H content by a transition from α- to β-phase [48]. Consequently, two H_2 sensing schemes are common: (1) a resistance increase caused by resistivity or work function change, typically used for low H_2 concentrations and (2) a resistance decrease induced by material expansion and subsequent nanogap closure, most often used for high H_2 concentrations. In both approaches, nanostructured Pd materials increase device sensitivity and speed over bulk through increased surface-to-volume ratios. Despite previous reports of Pd-based H_2 sensors, further performance enhancements are needed.

Here, chemiresistive sensors were fabricated from bio-templated gold-palladium (Au-Pd) nanopeapods and low concentration H_2 gas detection was demonstrated in air. Sensor performance was dictated by Pd thickness and overall Au-Pd nanopeapod morphology. Devices assembled from peapods with thin Pd layers, on the order of a few nanometers, exhibited highly sensitive H_2 sensing below 2000 ppm_v or 0.2 vol. %.

3.2 Experimental details

3.2.1 Au-Pd nanopeapod assembly on substrate

A previously reported M13 viral-templating method was adapted to assemble H_2 sensors composed of Au-Pd nanopeapods [90, 114]. The M13 virus has been reported as a versatile nanoscaffold for inorganic nanowire assembly due to its filamentous structure with diameter of 6.5 nm and length of 930 nm [12, 13, 23, 33, 117] and was advantageous in establishing the desired peapod-like geometry. The assembly scheme and a final device schematic are depicted in Figure 3-1. Standard microfabrication techniques were used to pattern pairs of 50 μm wide gold electrodes separated by a 3 μm gap on Si/SiO$_2$ substrates. Gold-binding M13 bacteriophage, displaying VSGSSPDS gold-binding peptides [13], were adsorbed onto these pre-patterned substrates and used to template strings of gold nanoparticles which were subsequently enlarged via a 1 min electroless deposition. Each substrate was then placed in 3 mM H$_2$PdCl$_4$ and ascorbic acid was slowly added over a 30 min period to a final molar ratio of 1:8 while stirring constantly. For thick deposition, the procedure was completed twice followed by a 10 min incubation. For thin deposition, the procedure was completed once followed by a 12 min incubation.

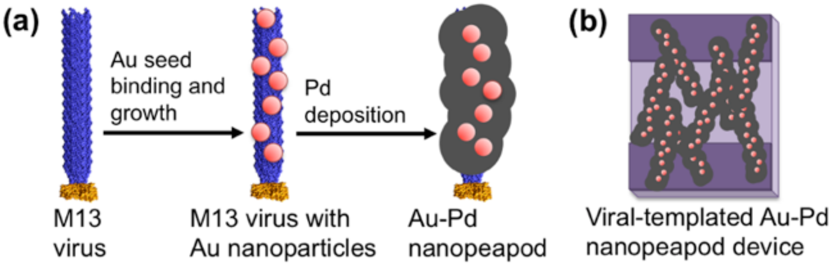

Figure 3-1 Schematics of viral templated Au-Pd nanopeapod assembly and chemiresistor geometry. (a) A gold-binding M13 virus was used to bind Au nanoparticles which were used as seeds for Pd deposition. (b) A chemiresistor composed of a random network of Au-Pd nanopeapods bridging two electrodes.

3.2.2 Morphological and materials characterization

Scanning electron microscopy (SEM, Phillips XL30 FEG) was used to determine morphology and distribution of gold nanoparticle chains and Au-Pd nanopeapod structures. Energy dispersive x-ray spectroscopy (EDS) on the SEM was used for elemental analysis and mapping of the fabricated nanopeapod devices.

3.2.3 Electrical and sensor characterization

Electrical resistance of the devices was determined by two-terminal current-voltage measurements. The voltage was swept from -0.3 V to 0.3 V using the Keithley 2636A sourcemeter while recording the current change on the custom Labview program.

Selected devices were wire-bonded to a copper printed circuit board (PCB), and then placed in a flow cell chamber with gas inlet and outlet [114]. The resistance of the devices was recorded while applying a constant bias of 0.15 V. A stable baseline resistance was established by flowing dry air for 5 hrs. The sensor was then alternately exposed to a known concentration of H_2 and dry air for 15 min and 30 min, respectively, at a flow rate of 200 sccm. H_2 gas was diluted to concentrations from 50 ppm_v to 2000 ppm_v using dry air as the carrier gas before introduction to the flow cell chamber. A custom Labview program was used to measure resistance, in addition to control gas concentration and exposure times.

3.3 Results and discussion

Scanning electron microscope (SEM) images of Au nanoparticle seeds and Au-Pd nanopeapod structures are shown in Figure 3-2. The 19 ± 4 nm diameter Au seeds were arranged in discontinuous chains along the viral templates which were randomly dispersed between electrodes. The Pd deposition selectively deposited on and enlarged the Au nanoparticles, creating an extended network of peapod structures. Two Pd deposition steps produced relatively thick nanopeapods with an average diameter of 50 ± 11 nm and an estimated shell thickness of 15.5 ± 6 nm, whereas a single Pd deposition step produced thinner nanopeapods with an average diameter of 29 ± 8 nm and an estimated shell thickness of 5 ± 4.5 nm. Consequently, the morphology of the nanomaterials was dissimilar. Despite thickness variations, thick Pd deposition yielded structures in which Au nanoparticles were completely encapsulated. In contrast, thin Pd deposition resulted in meager, perhaps even incomplete coating of Au seeds at some locations. Energy dispersive spectroscopy (EDS) spectra and elemental mapping of thick (Figure 3-3, Figure 3-4) and thin (Figure 3-5, Figure 3-6) Au-Pd nanopeapods showed presence of Pd and Au along the nanopeapod structures [118].

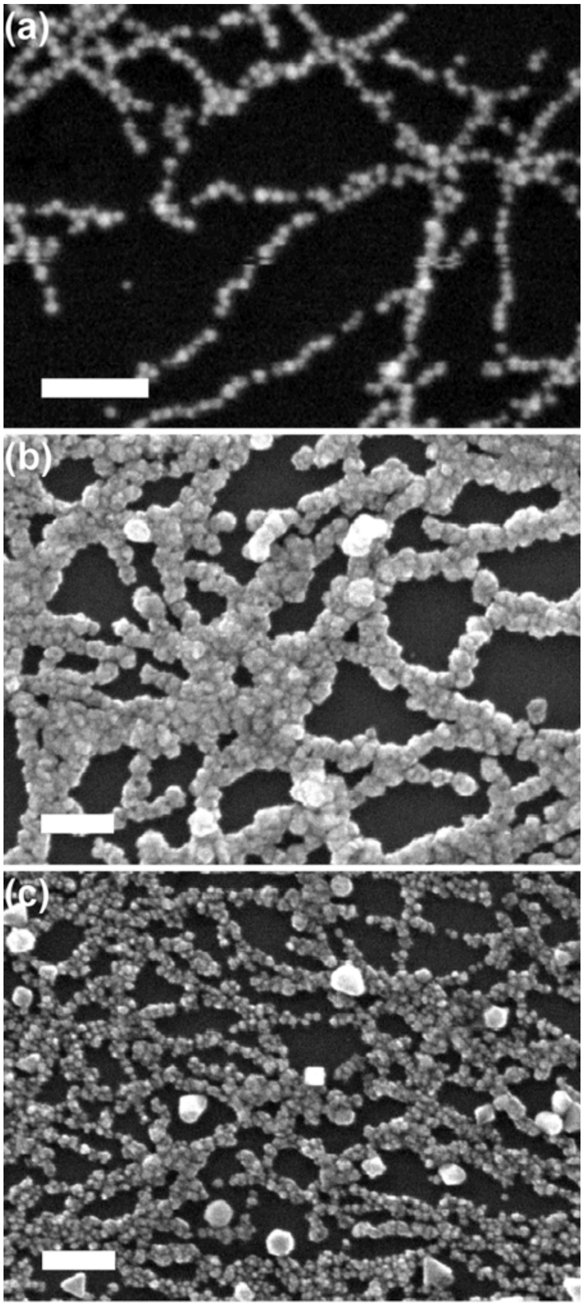

Figure 3-2 High magnification scanning electron microscope (SEM) images of (a) Au nanoparticle seeds and Au-Pd nanopeapods assembled with (b) thick and (c) thin Pd deposition. Scale bar is 200 nm.

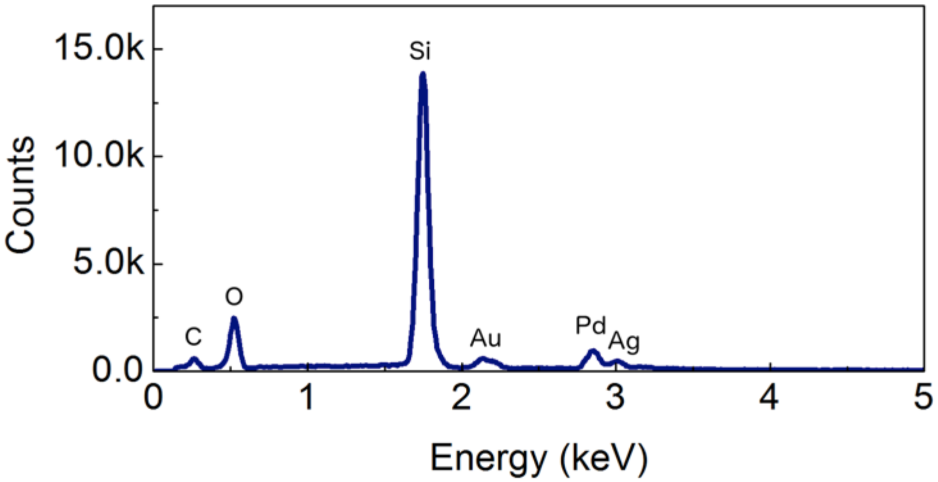

Figure 3-3 Energy dispersive spectroscopy spectrum of thick Au-Pd nanopeapods. Au and Pd were present in addition to Si and O from the substrate and Ag from the silver paste for grounding.

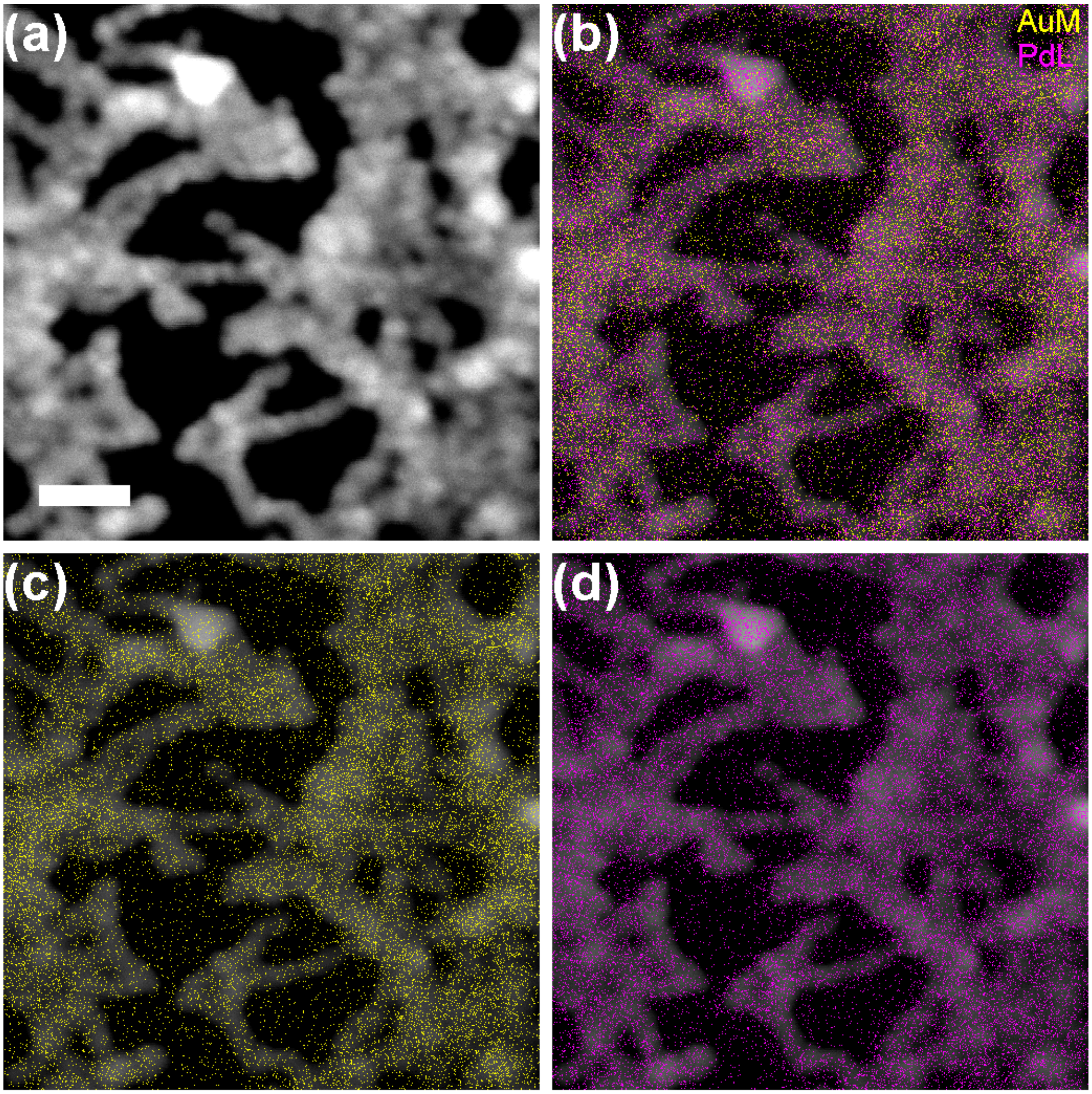

Figure 3-4 (a) Scanning electron microscopy image and (b-d) energy dispersive spectroscopy elemental mapping of thick Au-Pd nanopeapods with an average diameter of 50 ± 11 nm on a Si/SiO_2 substrate. SEM image is overlapped with elemental mapping of (b) both Au and Pd, (c) Au only, and (c) Pd only. Yellow and magenta are used to indicate the presence of Au and Pd, respectively.

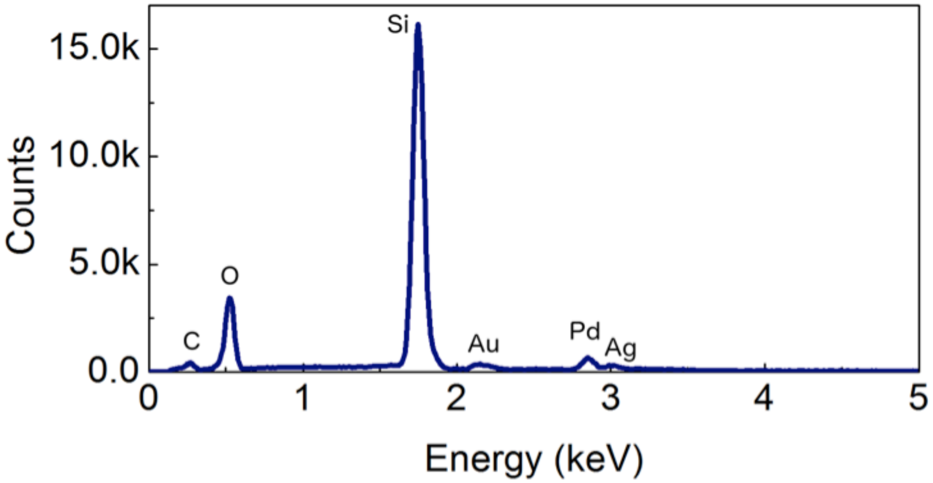

Figure 3-5 Energy dispersive spectroscopy spectrum of thin Au-Pd nanopeapods. Au and Pd were present in addition to Si and O from the substrate and Ag from the silver paste for grounding.

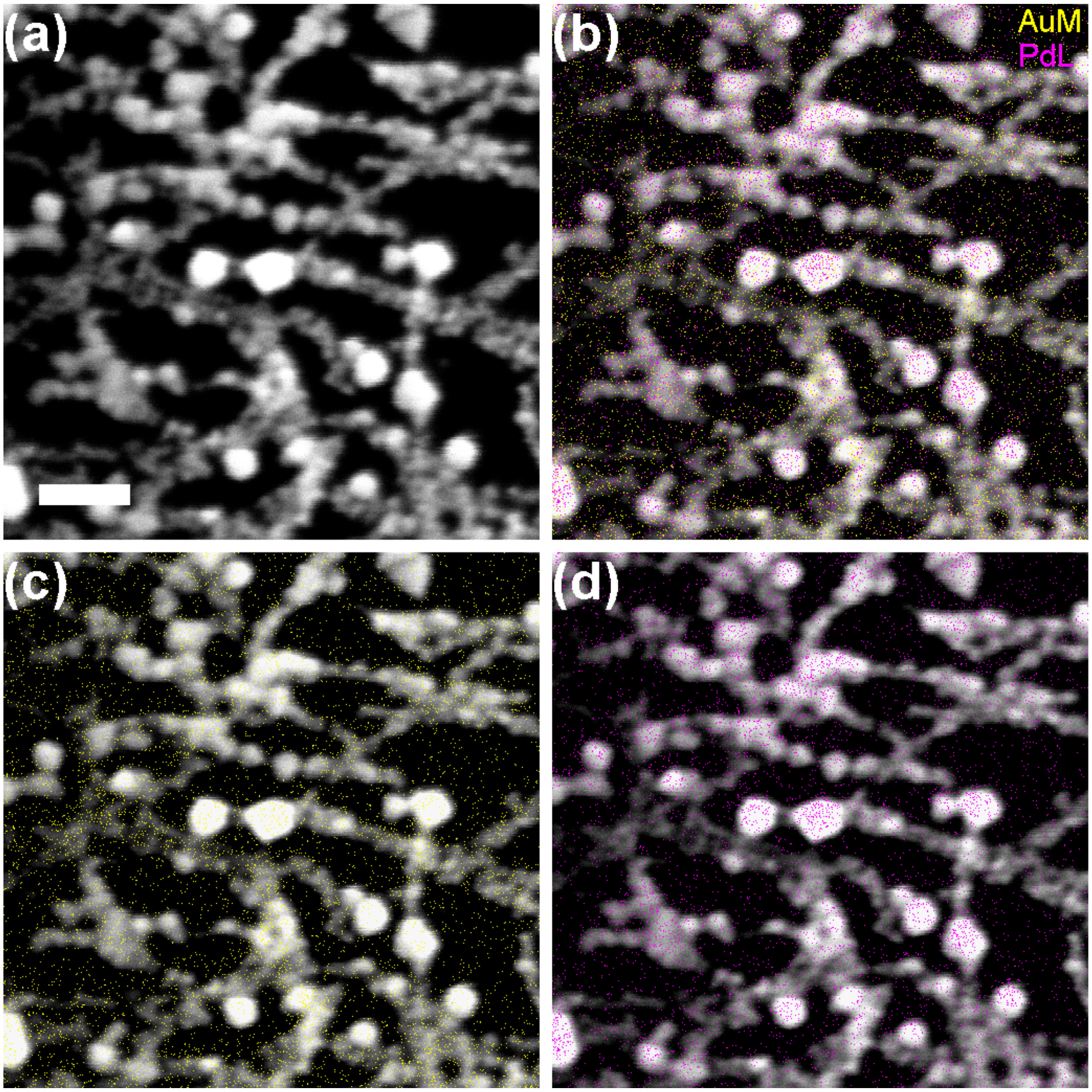

Figure 3-6 (a) Scanning electron microscopy image and (b-d) energy dispersive spectroscopy elemental mapping of thin Au-Pd nanopeapods with an average diameter of 29 ± 8 nm on a Si/SiO_2 substrate. SEM image is overlapped with elemental mapping of (b) both Au and Pd, (c) Au only, and (c) Pd only. Yellow and magenta are used to indicate the presence of Au and Pd, respectively.

The electrical resistance of the fabricated devices was measured at room temperature from -0.3 V to 0.3 V. Prior to Pd deposition there was no measurable current flow, thus confirming the electrical isolation of the Au nanoparticle seeds. Following Pd deposition, Ohmic behavior was observed within this voltage range for all devices. Current-voltage (I-V) characteristics for devices with thick and thin Pd layers are shown in Figure 3-7 (a) and (b), respectively. The median resistance of the devices with a thicker Pd layer was 4.7 kΩ, six to seven orders of magnitude lower than that of the devices with a thinner Pd layer. This disparate electrical behavior was well-correlated with differences in peapod morphology. Nanopeapods produced with two sequential Pd depositions were larger in cross-sectional area and less granular in appearance than those produced with a single Pd deposition. The complete encapsulation of the Au nanoparticles allowed significant conduction through the Pd coating, as well as through the seeds. The same was not true for the sparse Pd coverage created by a single deposition. Rather, the nearly incomplete Pd layer created a more bead-like morphology with tenuous connections between Pd-coated Au nanoparticles. This chain-like geometry hindered conduction between neighboring Pd shells strongly favoring electron hopping charge transport and substantially increasing resistance [94, 96, 119].

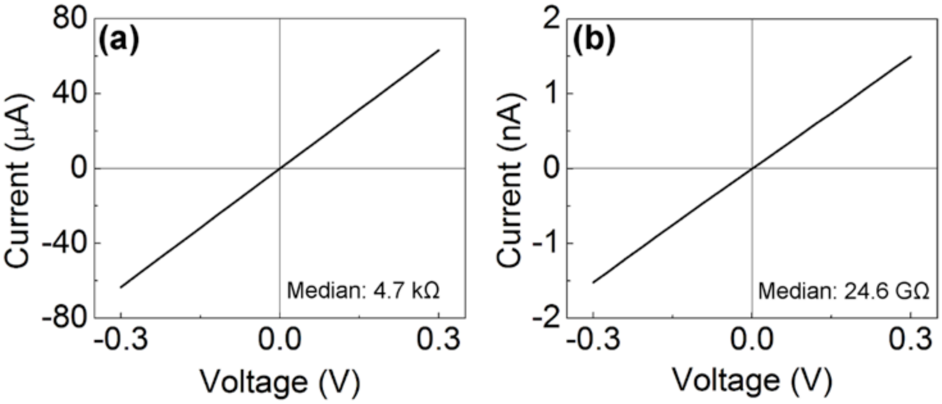

Figure 3-7 Representative I-V curves for Au-Pd nanopeapod devices with (a) thick and (b) thin Pd deposition shown with median resistance values for each fabrication condition.

The sensing performance of Au-Pd nanopeapod devices was evaluated in air at ambient temperature and pressure. The real-time sensing response of thick Au-Pd nanopeapod devices is presented in Figure 3-8 (a). Sensor response is defined as the change in resistance relative to the baseline resistance of the device, $R-R_0/R_0$ x 100, where R is resistance and R_0 is baseline resistance. A stable baseline resistance was obtained after 5 h of dry air flow. The expected increase in resistance associated with PdH_x formation was not observed with introduction of H_2 gas. Instead, the thick nanopeapod devices decreased in resistance with each H_2 gas exposure without recovery to the baseline during dry air purge. A similar decrease in resistance was reported for electrochemically-deposited and lithographically-patterned Pd nanowires [120, 121], Pd nanoparticle layers [57] and PdO thin films [122]. This behavior was attributed to the reduction of chemisorbed or incorporated oxygen caused by H_2 gas exposure, yielding Pd metal and irreversibly reduced resistance [57, 122]. We believe that during Pd electroless deposition and exposure to ambient air, oxygen species were incorporated into the Pd coating of the thick nanopeapods either as part of the bulk material or within the network of grain boundaries which extended throughout the layer. To test this hypothesis, the thick nanopeapod devices were conditioned through exposure to 2000 ppm_v H_2 for 3 h to remove residual oxygen species. The sensing response was then evaluated by alternating exposure to dry air and 2000 ppm_v H_2 gas. As shown in Figure 3-8 (b), during the conditioning period the device resistance decreased continually, rapidly at first and then more slowly. The time needed to fully reduce Pd-based nanomaterials is highly dependent on factors such material geometry, oxygen content, H_2 concentration, and gas flow. Reported times vary widely from 300 s to over 14 h [120, 121], therefore it is perhaps not surprising that a 3 h H_2 exposure was insufficient for complete removal of oxygen species and device resistance stabilization. Nonetheless, despite a slow, persistent decrease in resistance with each H_2 exposure due to continued reduction of oxygen species within the thick Pd layer, a rapid resistance increase and decrease corresponding to each H_2 exposure and dry air purge were observed following conditioning. Sensing responses ranging from 0.04% to 2.6%, calculated using the instantaneous resistance change and resistance just prior to H_2 exposure, were found for 2000 ppm_v H_2. Even though air was used as a carrier gas which was shown to lessen device response and increase lowest detection limit (LDL) compared to N_2 for some sensors [57, 115] the higher responses were comparable to those recorded for pure nanocrystalline 10-200 nm diameter Pd nanowire [55, 115] and nanoparticle [57] sensors.

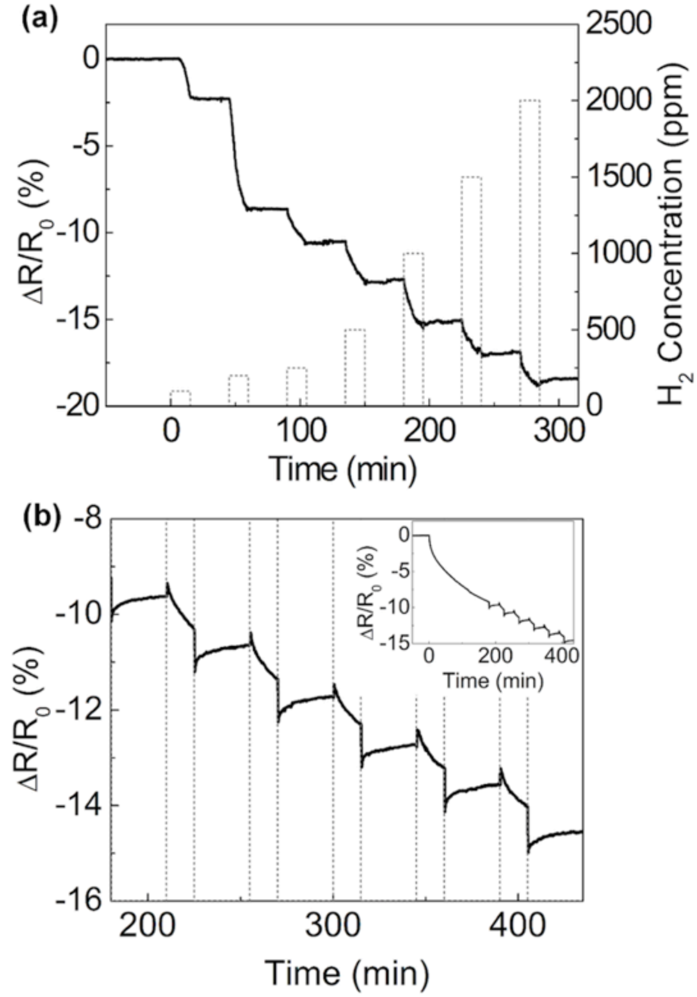

Figure 3-8 Representative real-time sensing behavior of thick Au-Pd nanopeapod sensors. (a) Sensors were exposed to H_2 for 15 min followed by dry air for 30 min. Corresponding H_2 concentrations, ranging from 100 to 2000 ppm_v, are shown with dashed lines. (b) Sensors were conditioned by exposure to 2000 ppm_v H_2 gas for 3 hours. Subsequently, sensors were alternately exposed to dry air for 30 min followed by 2000 ppm_v H_2 for 15 min. H_2 gas on and off points are shown with dashed lines. Inset displays sensor response throughout entire conditioning and H_2/air alternating exposure sequence.

Figure 3-9 (a) shows the real-time sensing response of thin Au-Pd nanopeapod devices. For this morphology, even without conditioning, only a small decline in baseline resistance due to H_2 reduction of oxygen species was detected within the initial exposure cycles. The comparatively fast reduction of Pd was credited to the reduced volume of oxygen species present and the rapid diffusion possible within the thin layer. A well-defined increase in resistance with H_2 exposure was seen clearly, as well as a partial recovery to baseline resistance during dry air purge. A small, gradual decrease in baseline resistance was also observed throughout initial H_2 exposure cycles. Similar to thick Au-Pd nanowires, this drift was attributed to the removal of oxygen chemisorbed onto the Pd surface. The calibration curve for thin Au-Pd nanopeapod sensors is found in Figure 3-9 (b). The average response to H_2 in air ranged from 2% at 100 ppm_v to 177% at 2000 ppm_v. Specifically, at 1000 ppm_v H_2, an average response of 84% was recorded for thin Au-Pd nanopeapod sensors. These responses are among the highest reported for continuous, Pd nanowire-based sensors at low H_2 concentrations [55, 56, 115, 123]. With the exception of a nearly 1000% response in air achieved by Lim et al. [56] for a device composed of vertical Pd nanotubes, other reports for the same H_2 concentration in N_2 are typically in the range of only a few percent. For example, Yang et al. [115] reported a 1-3% response with electrodeposited nanowires 10-100 nm in diameter; Zeng et al. [124] attained a 1-2% response with a network of sputtered Pd nanowires; and Offermans et al. [121] noted a 1.5% response with microfabricated Pd nanowires. The average LDL, defined as the concentration at which the response is 3 times the signal-to-noise ratio, was 25 ppm_v for the thin Au-Pd nanopeapod sensors. This LDL was lower than most of those measured in air and matched the detection limit of those measured in N_2 [52, 57, 115]. The relatively high response and low LDL are attributed to the combination of high surface-to-volume ratio of the viral-templated nanopeapods and the limited conduction path through numerous tenuous Au-Pd and Pd-Pd junctions. The large surface area facilitated H_2 adsorption, dissociation, and diffusion; and the thin Pd shell, estimated as 5 ± 4.5 nm, constrained the maximum diffusion length necessary for H incorporation into the Pd lattice to a fraction of the peapod width. Due to sparse Pd deposition and the resulting bead-like morphology of the Pd-coated Au nanoparticles, electron conduction was likely dominated by activated hopping transport between Pd shells. Under these circumstances, the material conductivity decreases exponentially with bead-to-bead barrier height [125, 126]. The formation of even a small amount of high resistivity material, such as PdH_x, within these fragile connections can substantially increase material resistance, resulting in high sensitivity gas detection. Similar behavior has been reported for other nanoparticle-based chemiresistive sensors [57, 114, 116].

The response time, defined as the time it takes for the resistance to reach 90% of its saturation value, for thin Pd devices was greater than 15 min at all H_2 concentrations, but 70% response was obtained within 1 min. Unlike the unconditioned thick Pd layer devices, at least partial recovery was observed at all H_2 concentrations for thin Pd devices. The recovery of resistance varied among devices and ranged from 53% to 89% within the 30 min time span. Moreover, all devices exhibited a minimum of 50% recovery within 4 min at all H_2 concentrations. The range in recovery times was attributed to differences in H desorption time from the Au-Pd nanopeapods. Despite low

Pd thickness which characteristically accelerates sensing behavior [115], these response and recovery times were sluggish compared to other nanostructured Pd H_2 sensors [57, 115]. One possible explanation for the high response time is slow H_2 dissociation on the Pd surface caused by H_2O contamination from oxygen species [57, 127]. Further studies are necessary to more fully understand limitations of sensor speed and performance.

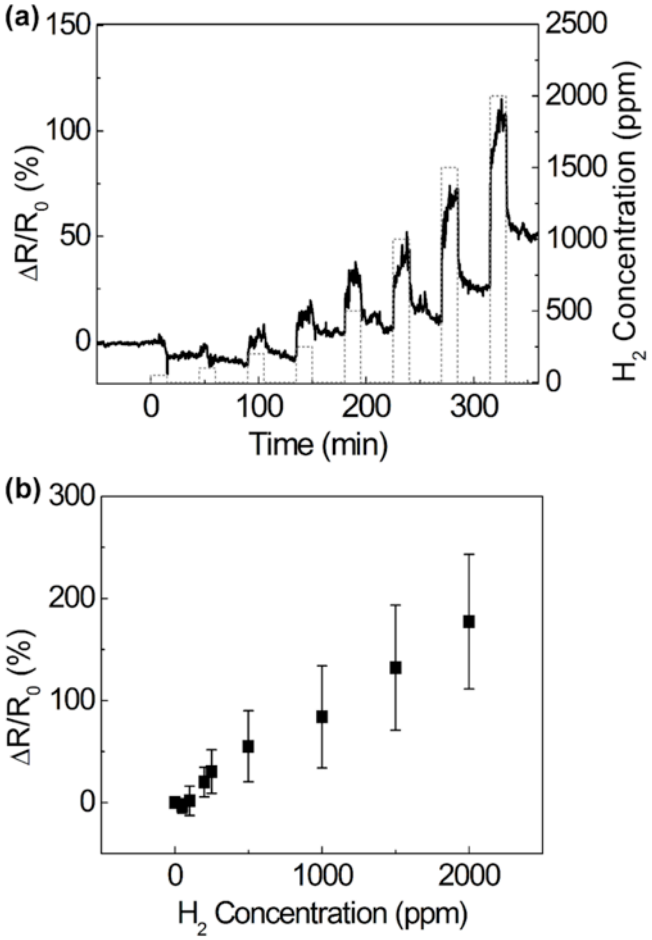

Figure 3-9 (a) Representative real-time sensing behavior and (b) average calibration curve of thin Au-Pd nanopeapod sensors. Sensors were exposed to H_2 for 15 min followed by dry air for 30 min. Corresponding H_2 concentrations, ranging from 50 to 2000 ppm_v, are shown with dashed lines.

These results were comparable or higher compared to previously reported work, as summarized in Table 3-1. An average response of 84% at 1000 ppm_v was notably high particularly at ambient air where O_2 and H_2 gases compete for adsorption to Pd surfaces.

Table 3-1 Chart to compare sensor performance of nanoscale Pd-based H_2 chemiresistive gas sensors. Work in this chapter in bold.

Device	Lowest detection limit (ppm)	Response to 1000%	Response time at lowest conc. (min)	Recovery time (min)	Carrier gas	Reference
Viral-templated Au-Pd peapod	**25**	**84**	**>15**	**>30**	**Air**	**[128]**
Ultrathin Pd film	25	12	40 sec	10 sec	N_2	[52]
Electrodeposited single Pd nanowire	1000-2000	1-3	13	0.1-30	Air	[115]
Network of ultrasmall Pd nanowires	100	1-2	1.7	1.7	N_2	[124]
Microfabricated Pd nanowire	10	1.5	45 sec	40 sec	N_2	[121]
Lithographically patterned single Pd nanowire	20	1	10 sec	3-80	N_2	[55]

3.4 Conclusion

In summary, we have fabricated highly sensitive H_2 sensors from Au-Pd nanopeapods that detect low concentrations of H_2 gas in air. Facile assembly of peapod structures was achieved with the M13 bacteriophage, a high aspect ratio bio-template. Pd shell thickness and the resulting Au-Pd nanopeapod morphology were critical factors affecting the electrical resistance and sensing performance of these devices. Thick Au-Pd nanopeapod devices with low electrical resistances displayed a rapid, irreversible decrease in resistance with initial H_2 exposure due to oxygen removal from the Pd layer, resulting in unsatisfactory sensing behavior. However, moderate sensing responses from 0.04% to 2.6% at 2000 ppm_v were achieved from these same devices after the removal of oxides by extended H_2 exposure for 3 h. In comparison, thin Au-Pd nanopeapod devices with high electrical resistances and more bead-like morphologies showed only a minimal resistance drop with initial H_2 exposure, and demonstrated very high sensitivity with a 117% response at 2000 ppm_v H_2 and a lowest detection limit of 25 ppm_v. Au-Pd nanopeapod sensors represent a promising device platform for room-temperature, highly sensitive chemiresistive detection of H_2 gas.

Chapter 4. ZnO Nucleation on Viral-Scaffold

4.1 Introduction

ZnO is a direct, wide-bandgap (3.2-3.4 eV) semiconductor which has proven useful for many electronic and optoelectronic applications in both bulk and nanocrystalline forms. It has been reported for applications in sensors, light emitting diodes, dye-sensitized solar cells, and photocatalytic devices [129, 130]. Bio-directed synthesis of ZnO is a promising technique capable of morphological control under generally mild, low temperature conditions. Biological molecules from small building blocks such as peptides and DNA, as well as larger structures such as bacteria, wood, and butterfly wings, have been reported to influence or direct ZnO nucleation [60, 86, 131]. Combinatorial phage display technology using the pIII library has been employed to discover number of different peptides with affinity to ZnO [28, 31, 132, 133]. Few of them have been further investigated for biomineralization purposes to form ZnO nanocrystals [132], nanoflowers [28, 134], and nanoplatelet [31] structures. However, such studies have focused on free peptides or peptides arranged on a planar surface.

M13 bacteriophage is a filamentous virus that is used in combinatorial phage display technique. It is composed of a pVIII major coat protein along the length of the virus, pIII and pVI minor coat proteins at one end, and two other minor coat proteins pVII and pIX at the other end of the virus Figure 1-1. These five coat proteins enclose a circular single stranded DNA inside, which encodes for the coat protein sequence and length of the virus. M13 bacteriophage has been reported as a promising scaffold for inorganic nanoamaterial assembly by displaying specific peptide sequences or molecules on its protein coat. Genetically modified phages have successfully template nanostructures of gold, silver, ZnS, and more [13, 21, 30, 135]. However, the tightly packed nature of pVIII coat protein limits the length (6-8 mer) and charge (negative at pH 7) of the peptides that can be displayed. Therefore, chemical conjugation methods used linker molecules have been employed for display of RGD cell affinity sequence [136] and poly(ethylene glycol) molecules [136], which will be adapted for display of highly positively charged, 12-mer ZnO-binding peptide.

Here we report the biomineralization of ZnO on a M13 bacteriophage biological scaffold. A reported peptide sequence (EAHVMHKVAPRP, Figure 4-1) with high affinity for ZnO [28] was displayed on each pIII and pVIII protein coats of the M13 bacteriophage to mineralize ZnO nanoparticles. For ZnO nucleation on the pVIII protein coat, a crosslinker molecule, sulfosuccinimidyl 4-[N -maleimidomethyl]cyclohexane-1-carboxylate (sulfo-SMCC) was used to covalently bind and display the reported peptide at controlled densities. The density of peptide coverage was controlled, confirmed, and mineralization of ZnO was performed. These studies explore ZnO biomineralization on the various structural proteins of the M13 bacteriophage at ambient conditions.

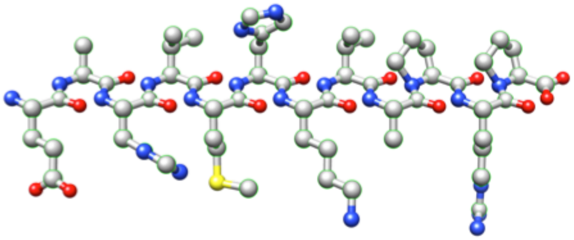

Figure 4-1 Ball-and-stick model of ZnO-binding sequence, EAHVMHKVAPRP, built using Chimera software [24].

4.2 Experimental details

4.2.1 Genetic insertion of ZnO-binding peptide in pIII

The previously published ZnO-binding peptide (EAHVMHKVAPRPGGGSC) [28] was genetically fused on the pIII coat protein of the M13 bacteriophage. An oligonucleotide 5'-CAT GTT TCG GCC GAA CAA GAA CCT CCG CCA GGA CGT GGT GCA ACT TTG TGC ATA ACA TGA GCT TCA GAG TGA GAA TAG AAA GGT ACC CGG G-3' (Integrated DNA Technologies, IDT) encoding for the 17-mer ZnO-binding peptide sequence was polymerase chain reaction (PCR) amplified and digested with *Acc65I* and *EagI* restriction enzymes. The M13 bacteriophage vector, M13KE, was digested using the same restriction enzymes, then the oligonucleotide and vector was ligated to form a circular vector DNA with insertion in gIII region. The vector was transfected into the XL1-Blue electroporation competent cells through electroporation and titered. The display of ZnO-binding peptide on the pIII minor coat protein was confirmed through DNA sequencing (Applied Biosystems 3730xl DNA Sequencer). Once confirmed, the phage was amplified using ER2738 strain *E. coli* and following the standard M13 amplification procedure.

4.2.2 Chemical conjugation of peptide with sulfo-SMCC linker

A crosslinker molecule, sulfosuccinimidyl 4-[N -maleimidomethyl]cyclohexane-1-carboxylate (sulfo-SMCC, Thermo Scientific) was used to covalently conjugate the ZnO-binding peptide (EAHVMHKVAPRPGGGSC, Biomatik) to the M13 bacteriophage pVIII protein coat using a two-step procedure. Sulfo-SMCC and pVIII protein coats are shown in Figure 4-2. First, the sulfo-SMCC chemical crosslinker (10 mg/mL) and M13 bacteriophage (1.86×10^{13} pfu total, 0.238 mM available amine group) were co-incubated in phosphate buffered saline (PBS, 100 mM sodium phosphate, 150 mM sodium chloride, pH 7.2) at room temperature for 30 min for covalent binding of the linker molecule on available amine groups. Free unbound crosslinker molecules were then removed using the Zeba desalt spin column (Thermo Scientific) according to the manufacturer protocol. In the second step, the collected sulfo-SMCC conjugated M13 bacteriophage was immediately aliquot into 100 μL volumes and peptide concentrations equal to 0.5 (0.012 mM) to 4 (0.95 mM) molar excess to available amine groups (0.238 mM) were added. The reaction was left at room temperature for another 30 min to result ZnO-binding peptide conjugated M13 bacteriophage.

Quantitative analysis to determine conjugated peptides on viral-template was performed with Ellman's reagent (5,5'-dithio-bis-(2-nitrobenzoic acid), Thermo

Scientific), which is a colorimetric indicator of free sulfhydryl groups in solution. A mixture of 1 mL phosphate buffer (PB, 0.1 M sodium phosphate, pH 8.0, 1 mM EDTA), 20 μL Ellman's reagent (4 mg/mL in PB), and 100 μL of conjugated sample was prepared and left at room temperature for 15 min. The absorbance of the mixture was measured at 412 nm to determine free sulfhydryl group. A standard curve was obtained first with peptide concentrations from 0 to 1.5 mM in place of 100 μL of conjugated sample, which was used to correlate absorbance at 412 nm to unbound peptide molarity. The percent coverage on the phage was found by subtracting the free, unbound sulfhydryl groups from the initial peptides added: molar peptide added in mixture – molar free sulfhydryl in solution determined from Ellman's reaction.

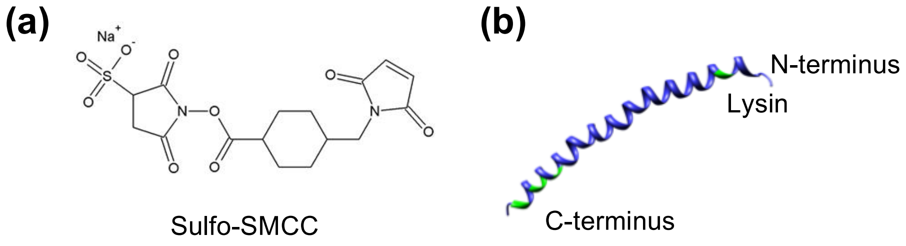

Figure 4-2 (a) Chemical structure of sulfo-SMCC and (b) Chimera image of pVIII coat protein [24]. The amine groups present in pVIII coat protein are indicated in green, and the sulfo-SMCC linker molecule can conjugate to the n-terminus and lysine residue.

4.2.3 Matrix-assisted laser desorption/ionization (MALDI) analysis

Covalent conjugation of ZnO-binding peptide on M13 pVIII protein coat was confirmed by matrix-assisted laser desorption/ionization time-of-flight mass spectroscopy (MALDI-TOF MS, QSTAR XL oMALDI MS/MS). The pVIII coat proteins were obtained by incubating 100 μL of 2.66 x 10^{10} pfu/μL of peptide conjugated phage with 25 μL of 6 M guanidine hydrochloride at room temperature for 5 min for denaturation. Smaller fragments, molecules, and salt were removed using a molecular weight cut-off filter (Vivaspin 500 MWCO 300, Vivaproducts). The purified, denature protein sample was mix with acetonitrile, trifluoroacetic acid, and α-cyano-4-hydroxycinnamic acid matrix and spotted on the matrix plate for analysis.

4.2.4 ZnO nanocrystal synthesis on M13 bacteriophage protein coat

A previously reported procedure for free peptide-assisted ZnO biomineralization, was adapted for ZnO mineralization on the M13 pIII minor coat protein [28]. Briefly, equal volumes of 10 mM zinc nitrate hexahydrate ($Zn(NO_3)_2$•$6H_2O$, > 99.0%, Acros Organics) and 20 mM potassium hydroxide (KOH, Fisher Scientific) were mixed to form zinc hydroxide ($Zn(OH)_2$). The formed $Zn(OH)_2$ was washed with deionized water and the concentration was adjusted to 10 mM $Zn(OH)_2$. Different concentrations of $Zn(OH)_2$ were prepared similarly by starting with the appropriate concentrations of $Zn(NO_3)_2$ and KOH. M13 bacteriophage were added to the $Zn(OH)_2$ solution to a final concentration of $2x10^9$ pfu/μL and $2x10^8$ pfu/μL for pIII modified and pVIII conjugated ZnO-binidng phages, respectively, and the samples were left to mineralize at room temperature without agitation.

4.2.5 Morphological characterization

Transmission electron microscopy (TEM, FEI-Phillips CM300 and FEI Tecnai12) was used to examine the nanocrystal diameter and size distribution of mineralized material. TEM samples were prepared by placing 5 μL of the reaction on a carbon-coated copper grid (Ted Pella, Inc), allowing 5 minutes for adsorption, and rinsing the grid twice in deionized water for 5 minutes. Selected samples were negatively stained with 5 μL of 2% uranyl acetate, followed by removal of excess liquid by wicking off with filter paper. Nanoparticle diameters and particle size distributions were determined using these images. Energy dispersive x-ray spectroscopy (EDS) was performed on the TEM (FEI-Phillips CM300) for elemental analysis of the nucleated materials.

4.3 Results and discussion

A genetically modified M13 bacteriophage displaying a previously report ZnO-binding peptide, EAHVMHKVAPRPGGGSC, on its pIII coat protein was used to form ZnO nanoparticles. Figure 4-3 shows the formation of ZnO nanoparticles on the M13 virus after incubation with the $Zn(OH)_2$ precursor solution for 10 h. The viral capsid appears structurally intact indicating insensitivity to the precursor solution. The location of the nanoparticles, at the tip of the filamentous virus suggests that ZnO was directly mineralized on the pIII coat protein due to the ZnO-binding peptide fusion. Notably, a ZnO nanoparticle cannot be found on all viruses. Further studies are needed to understand the low incidence of mineralization. The particle size distribution determined from TEM images is shown in Figure 4-4. A broad size distribution with an average particle diameter of 53 nm was found. The observed distribution is similar to that reported for the ZnO-mineralizing peptide, GAMHLPWHMGTL [132]. In contrast to the ZnO-binding peptide used in our experiments, the ZnO-mineralizing peptide was selected for catalytic activity rather than binding affinity. It is curious that both peptides exhibit the lack of control over polydispersity which has been reported for other peptides and other materials [30, 137]. No nanoparticles were seen in a control sample without bacteriophage, reinforcing the conclusion that the ZnO-binding peptide was responsible for nanoparticle formation. Unlike, previous reports of nanoparticles [28, 31, 130] mineralized with free ZnO-binding peptides, the nanoparticles attached to the tip of the virus remained as individual nanoparticles rather than forming larger clumps of ZnO.

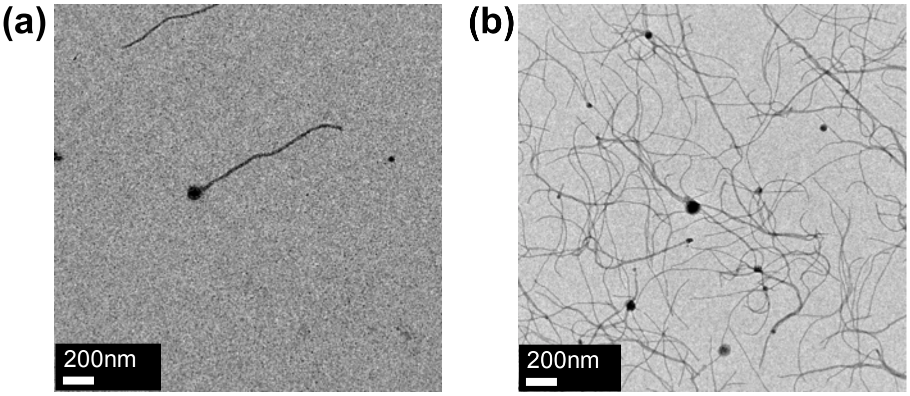

Figure 4-3 Transmission electron microscopy (TEM) images of ZnO nanoparticles formed on the pIII genetically modified M13 bacteriophage after 10 h of incubation. (a) A single M13 bacteriophage with nanoparticle attached at one end and (b) shows polydispersity of nanoparticles formed. TEM images were negatively stained with 2% uranyl acetate.

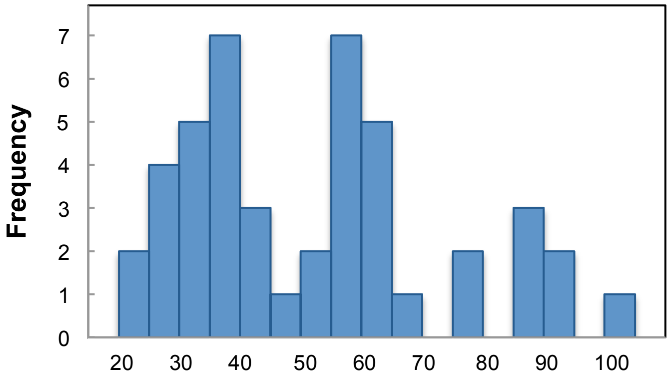

Figure 4-4 Histogram to show distribution of ZnO nanoparticle diameters obtained from 10 mM $Zn(OH)_2$ after 10 h incubation.

The effect of precursor concentration and incubation time on the diameter of the biomineralized ZnO nanoparticles is shown in Figure 4-5. TEM images were used to determine the diameters of nanoparticles formed in 1 mM and 10 mM of $Zn(OH)_2$ precursor solution at different incubation times. All studied mineralization conditions resulted in highly polydisperse nanoparticles. The standard deviation in particle diameter was typically ± 34% of the average diameter. Average nanoparticle diameters ranged from 51 to 77 nm. In addition, given the particle size distribution, there was no significant dependence of the nanoparticle diameters on precursor concentration or incubation time. The ZnO-binding peptide displayed on the M13 bacteriophage acted as a ZnO nucleation site, mineralizing polydisperse nanoparticles at wide range of conditions.

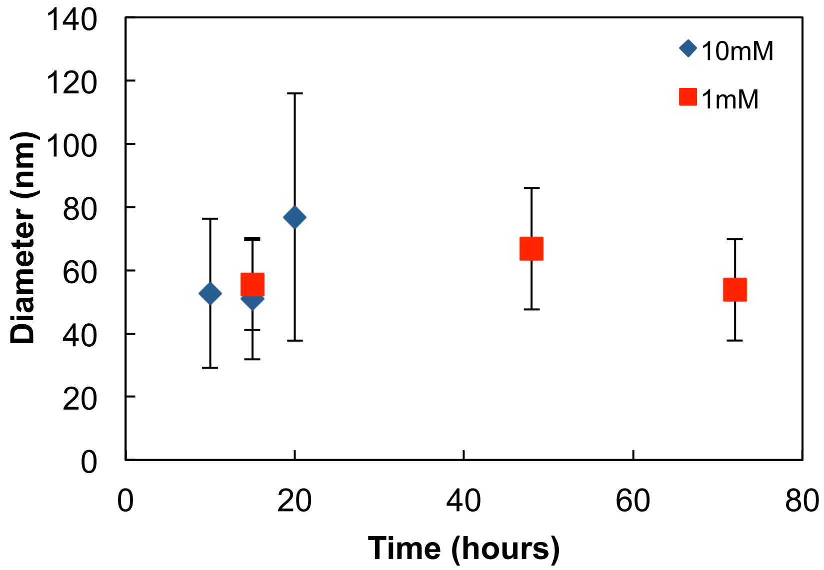

Figure 4-5 The average diameter of ZnO nanoparticles at different precursor and incubation times.

With successful nucleation of ZnO nanoparticles on the pIII coat protein, a chemical modification method was used to display the same ZnO-binidng peptide EAHVMHKVAPRPGGGSC on the pVIII protein coat for ZnO nucleation on a 1D scaffold. A bi-functional crosslinker, sulfo-SMCC was covalently conjugated on the amine groups on the n-terminus and lysine side group close to the n-terminus. Then, the sulfur on the cysteine side group was conjugated on the other end of the crosslinker for bioconjugation of the peptide. The % coverage of peptide on the phage with different peptide concentration added was monitored using the Ellman's reagent, which determines the amount of sulfhydryl groups left in solution, and shown in Figure 4-6. A saturation of the curve was expected close to 100%, however a continuously increasing curve was obtained up to 315% coverage. We attribute this to possible disulfide bond formation between the peptides within the solution to reduce sulfhydryl groups, resulting greater coverage above 100%. Although saturation was not obtained, a slight decrease in slope was observed at 0.5 molar excess (0.119 mM) of ZnO-binding peptide to available sites (0.238 mM).

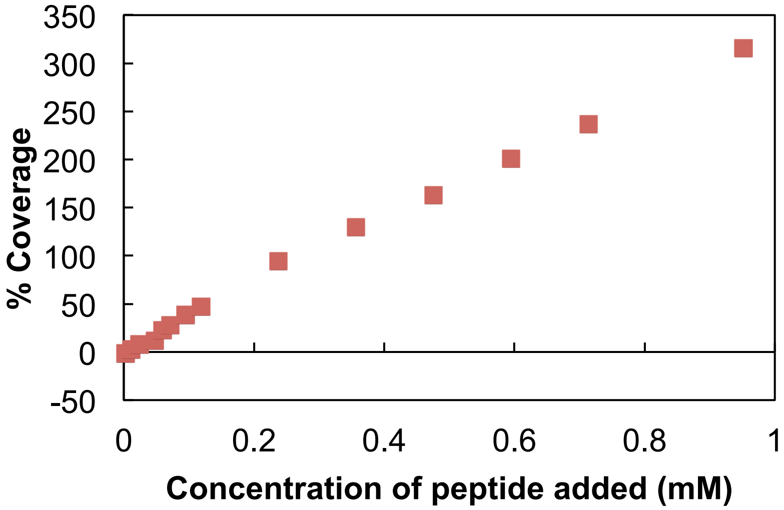

Figure 4-6 Percent coverage of ZnO-binding peptide on phage with 0.238 mM available sites with respect to concentration of peptides added in reaction.

Conjugation of ZnO-binding peptide on the M13 bacteriophage coat protein was confirmed by matrix assisted laser desorption/ionization time-of-flight (MALDI-TOF) analysis. Figure 4-7 displays the spectra obtained from the conjugation sample prepared with equal amounts of available binding sites and ZnO-binding peptides. The MALDI-TOF MS spectra displayed 4 major peaks at m/z 1733, 5238, 7189, and 9240. These peaks correlated well with different proteins that could exist in the sample: free ZnO-binding peptide (1733 Da), unmodified pVII coat protein (5238 Da), pVIII coat protein with one ZnO-binding peptide conjugated (7189 Da), and pVIII coat protein with two ZnO-binding peptide conjugated (9104 Da). This analysis showed conjugation of ZnO-binding peptide on the pVIII coat protein of the M13 bacteriophage. At 1 molar excess of peptide, 100% coverage of two ZnO-binding peptides on each pVIII protein was not possible. Although further study is necessary, fully understand the capability, 100% coverage may be difficult to obtain due to steric hindrances in the tightly packed pVIII coat proteins.

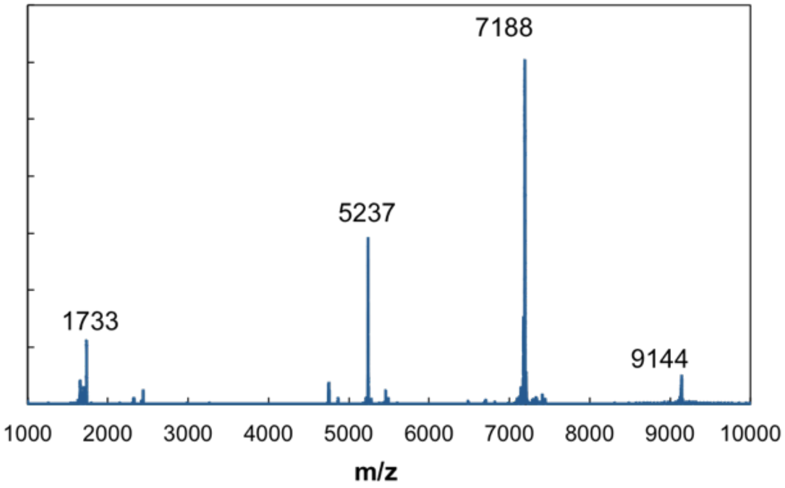

Figure 4-7 MALDI-TOF MS spectra of pVIII coat protein with sulfo-SMCC and ZnO-binding peptide conjugation.

The ZnO-binding peptide conjugated phages were flocculated when observed under the TEM as shown in Figure 4-8 (a). Conjugation of highly positively charged

ZnO-binding peptide increased the theoretical isoelectric point of the pVIII protein from 3.92 to 6.03. Therefore, a significant reduction in electrostatic repulsion between the phages at pH 8 buffer occurred, resulted large agglomerates phages. A similar nucleation condition to pIII ZnO nucleation was used for mineralization on the ZnO-binding peptide-conjugated phages. Instead of nanocrystal formation, a film of inorganic materials was obtained from the flocculated phages as shown in Figure 4-8 (b). Elemental analysis using energy dispersive x-ray spectroscopy (EDS) clearly indicated presence of Zn and O (Figure 4-8 (c)), however, amorphous rings were obtained with electron diffraction analysis (data not shown). The ZnO-binding peptide was successfully displayed on the pVIII coat protein of the M13 bacteriophage nanoscaffold. Challenges of phage flocculation and amorphous material synthesis still need to be resolved, however this study displays promise of M13 bacteriophage as a solid scaffold for directed ZnO mineralization.

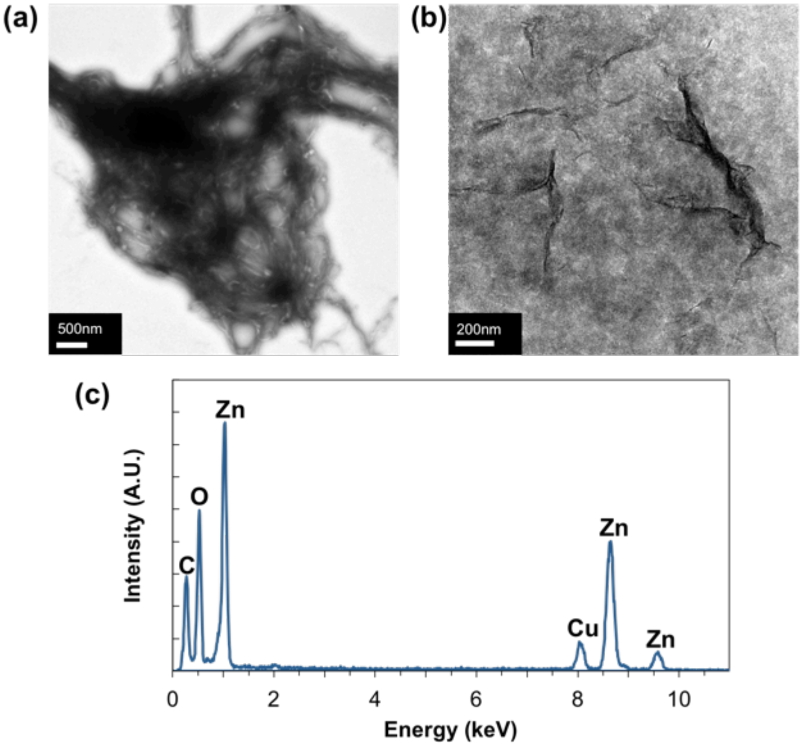

Figure 4-8 Transmission electron microscopy (TEM) images of flocculated ZnO-binding peptide-conjugated phages (a) after uranyl acetate staining and (b) after ZnO nucleation at room temperature in film-like form. (c) Energy dispersive x-ray spectrum (EDS) of nucleated material on flocculated ZnO-binding peptide-conjugated phages shown in (b). Copper and carbon peaks likely originate from carbon-coated copper grid used.

4.4 Conclusion

In this chapter, we demonstrated ZnO nucleation and growth on the M13 pIII and pVIII coat proteins using a previously reported ZnO-binding peptide [28]. The ZnO nanocrystal formation on the genetically displayed pIII protein was independent of precursor concentration and incubation time, resulting polydisperse nanoparticles. While

100% coverage was not obtained, M13 bacteriophage template with chemically conjugated ZnO-binding peptides were obtained and confirmed. Amorphous ZnO materials film was formed on the flocculated ZnO-binding peptide-conjugated phages. These studies are initial steps towards bottom-up synthesis of ZnO on M13 nanoscaffold that offer long range order that affect ZnO morphology and properties.

Chapter 5. Peptide-Assisted ZnO Nanomaterial Synthesis

5.1 Introduction

Zinc oxide (ZnO) is a wide bandgap semiconductor (3.2-3.4 eV), with high exciton binding energy (60 meV). Its unique electrical and optical properties have led to its widespread use in optoelectronic, piezoelectric, gas sensing, and photocatalytic devices, among others [138]. Morphology, particle size, crystallinity, and point defects must be modified to provide specialized physical properties required for each application. While single crystal, defect-free materials are typically essential for optoelectronic and piezoelectric applications, polycrystalline materials are largely acceptable for gas sensing and photocatalytic applications. Moreover, gas sensor performance can be enhanced by the accumulation of some defects which act as donors or preferential binding sites [70, 139]. In addition, the presence of sub-bandgap defect levels can improve sensitivity by acting as additional analyte adsorption sites and carrier donors in chemiresistive sensor applications [70, 71, 140]. In order to effectively tune ZnO properties, a range of synthesis methods including chemical vapor deposition, sol-gel processing, and aqueous-based chemistry have been reported [138].

More recently, synthesis assisted by biological molecules such as collagen [141], proteins [142] and peptides [28, 31, 132, 143, 144] has been introduced as a promising alternative ZnO growth strategy. Biomolecules allow formation of crystalline ZnO under environmentally benign conditions, which include mild temperature, atmospheric pressure, and aqueous solution. Amongst biomolecules, peptides have been studied extensively due to the specificity and chemical diversity made possible by their amino acid building blocks, and the ease of discovery afforded by combinatorial display techniques. Umetsu et al. first reported a 12-mer ZnO-binding peptide sequence discovered through pIII phage display technique and synthesized nanoflower ZnO [28]. Thereon, there have been several other peptides with high affinity for ZnO that have been identified using phage- or bacteria surface- display [31, 132, 133, 145, 146]. Like many naturally occurring zinc-binding proteins, the majority of the reported peptides have been net basic peptides (pI > pH 7), rich in arginine (R), histidine (H), or lysine (K) residues. In addition to binding capability, a handful of the identified peptides have demonstrated an ability to influence crystal growth by serving as either capping agents [31, 147] or nucleation sites [143] to form characteristic nanoparticles [132], nanorods [31, 143], nanoplatelets [31, 147], and nanoflowers [28]. Despite strong interest in material formation mechanisms, crystallinity, and morphology, optical and electrical behavior of the resulting bio-directed materials has been largely neglected.

In this chapter, an 8-mer M13 bacteriophage pVIII library was used to identify peptides with an affinity for ZnO. Because viral protein packing restricts the size and electrostatic charge of pVIII peptide fusions, net basic fusions tend to inhibit efficient capsid assembly and have low frequency within this library, allowing exclusive discovery and study of neutral to acidic peptides. In this work, an acidic peptide sequence (VPGAAEHT) with an affinity for ZnO was found and used to as an additive during ZnO synthesis. The resulting nanoscale ZnO materials were characterized, including photoluminescence measurements as a function of peptide concentration. In addition, resistance, sensing, and photocurrent measurements on a film of 0.1 mM structures were made. During synthesis, this acidic, hydrophobic peptide modified ZnO crystallinity, morphology, and defect level emission, suggesting potential for use in photocatalytic and gas sensing material formation.

5.2 Experimental details

5.2.1 Combinatorial phage display technology using the pVIII library

Peptides with affinity for ZnO were identified using combinatorial phage display technology, also known as biopanning [27]. A M13 phage display library with a random 8-mer peptide fused to the N-terminus of the pVIII coat protein was constructed with a previously reported method [34]. Figure 5-1 shows one single round of combinatorial phage display screening using the pVIII library. Similarly, the library, with a diversity of 3.65×10^7 clones, was added to 1 mg/mL ZnO powder (Sigma-Aldrich) dispersed in Tris-buffered saline with 0.1% Tween-20 (TBST, 50 mM Tris-Cl, 150 mM NaCl, pH 7.5) and incubated at room temperature for 1 h to allow phages to bind. Unbound and weakly bound phages were removed from the ZnO powder by repeated washing in 0.1% TBST. Bound phages were physically eluted from the powder surface by sonication in 0.7% TBST for 1 min [148]. The eluate was amplified by infecting the ER2738 strain *E.coli* and collected for use in the next selection round. This biopanning procedure was repeated to increase stringency. After five screening passes, DNA from the eluted phages was sequenced (Applied Biosystems 3730xl DNA Sequencer) to identify binding peptides. The most recurrent phage and associated 8-mer ZnO-binding peptide were chosen for further study.

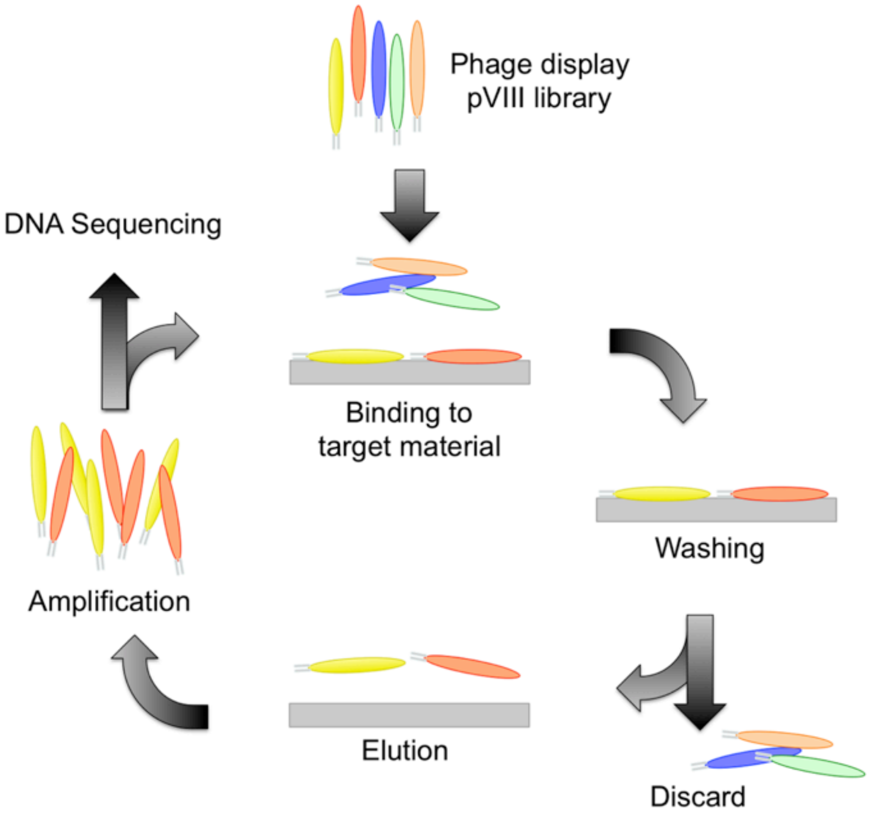

Figure 5-1 Schematic diagram of one complete round of combinatorial phage display technique (biopanning) from pVIII phage display library.

5.2.2 Binding test against ZnO

Phage binding strength was determined by incubating $1x10^{11}$ pfu of phages with a polycrystalline thin film of ZnO grown by molecular beam epitaxy (MBE) on a (100) Si substrate (ZnO/Si) in 0.1% TBST for 1 h. Following multiple washes with 0.5% TBST, the bound phages were physically eluted by sonication of the ZnO/Si substrate in 0.7% TBST for 1 min. The phage concentration of the eluate or binding strength was determined by titering. The binding strengths of the recurrent ZnO-binding and wild-type phages were each measured four times. Average values were reported. The same procedure was also completed for both phages with a (100) Si substrate. To isolate the binding strength associated with ZnO, the average binding strength for (100) Si was subtracted from that of ZnO/Si.

5.2.3 Nucleation with ZnO-binding phage

The ZnO-binding phage was co-incubated with ZnO precursors to direct mineralization. For zinc nitrate hydrate ($Zn(NO_3)_2 \bullet H_2O$, 99.999%, Sigma-Aldrich) and hexamethylenetetramine (HMTA, Sigma-Aldrich) condition, the two precursors were added at same molarity and volume. For zinc nitrate hydrate ($Zn(NO_3)_2 \bullet H_2O$, 99.999%, Sigma-Aldrich) and potassium hydroxide (KOH, Fisher) condition, zinc hydroxide ($Zn(OH)_2$) sol was made first by mixing the precursors at 1:2 ratio. The $Zn(OH)_2$ sol was washed 5 times with deionized water and adjusted to desired concentration before the addition of the ZnO-binding phage. Nucleation in solution with phage and precursors were performed according the Table 5-3 and phage concentrations were all $2x10^9$ pfu/μL.

5.2.4 ZnO synthesis with specific peptide additives

The ZnO-binding peptide was synthesized with a GGGSC linker (Biomatik) and suspended in TBS. Equimolar zinc nitrate hydrate ($Zn(NO_3)_2 \bullet H_2O$, 99.999%, Sigma-Aldrich) and hexamethylenetetramine (HMTA, Sigma-Aldrich) precursors were mixed to 50 mM in 300 μL of deionized water. ZnO-binding peptides from 0 to 0.6 mM were added to the precursors and incubated in 65°C oven for 24 h. Precipitates were washed twice with deionized water and collected through centrifugation.

5.2.5 Morphology and crystallinity characterization

Transmission electron microscopy (TEM) samples were prepared by drop casting washed precipitates onto carbon-coated copper grids followed by two water washes and gentle air dry. Elemental composition and crystal structure was determined by energy dispersive x-ray spectroscopy (EDS) and electron diffraction analysis using TEM (FEI CM300) at 300 kV. Scanning electron microscopy (SEM) samples were prepared by drop casting and drying the precipitates on clean Si wafers. The morphology of the synthesized materials was observed with SEM (Phillips XL30 FEG) at 10 kV and the aspect ratio (length/diameter) of the structures was measured.

5.2.6 Optical characterization

Fourier transform infrared spectroscopy (FTIR, Nicolet 6700 Thermo Scientific) analysis from 1300 to 1800 cm^{-1} was performed on vacuum dried precipitates in powdered form. Photoluminescence (PL, Horiba Jobin-Yvon Spex Fluorolog) measurements of drop cast ZnO materials were made at room temperature using 320 nm excitation and spectra were normalized to either the band-edge or near band-edge emission peak.

5.2.7 Device fabrication and photoresponse measurement

Gold electrodes (20 nm Ti/150 nm Au) with 200 μm gap was deposited on Si/SiO_2 substrate using shadow mask and electron-beam evaporation. The chips were cleaved and washed with acetone, isopropanol, and water prior to use. Similar deposition process was used as described in chapter 2 and 3. The washed chips were O_2 plasma treated for 30 sec, then submerged in solution of washed ZnO precipitates that is 3 times more concentrated than the as-synthesized solution. The chip was incubated in ZnO nanomaterial solution for 1 h, then gently washed in water, and dried with air.

Electrical resistance was determined by current-voltage measurement on the probe station. The change in current was recorded while the voltage was swept from -0.3 V to 0.3 V using the sourcemeter (Keithley 2636A). Selected devices on the chip were wire-bonded to the copper printed circuit board (PCB) using a 1% Si/Al wire.

The wire-bonded devices were each placed in a separate close cell chamber with 527 nm light emitting diode (LED, CREE, C503B-GAS/GAN) placed within 2 cm distance above the device. The resistance was recorded while a constant bias of 0.15 V was applied to the ZnO devices using a custom Labview program. A stable baseline was obtained in dark for 90 min, then the light was turned on and off alternating every 5 min. The LEDs were connected serially and 8 V was applied. In addition, gas sensing analysis was performed against NH_3 concentrations from 0.5 ppm to 100 pm at room temperature in a flow cell as described in Chapter 2.

5.3 Results and discussion

Combinatorial phage display screening using the M13 pVIII library identified several peptide sequences (Table 5-1) with affinity for ZnO, all of which were acidic in nature (pI < pH 7). One peptide, VPGAAEHT, was displayed on 7 out of the 23 phages sequenced and stood out as the strongest ZnO binder. This peptide sequence, depicted in Figure 5-2 (a), was selected for further study and will hereafter be referred to as the ZnO-binding peptide [24]. It included the charged amino acid residues histidine (H) and glutamate (E), and was rich in hydrophobic residues. Statistical analysis of the peptide sequences obtained after the fifth round of biopanning against ZnO is listed in Table 5-2. The peptide sequences contained high percentage of hydrophobic residues, alanine, valine, and glycine, which together made up 40% of total amino acids obtained. The frequency of each amino acid occurrence in the pVIII library is also indicated on the last column for comparison.

Table 5-1 List of peptide sequences obtained after 5 rounds of biopanning. The isoelectric point of each peptide was calculated using peptide property calculator by Innovagen AB (http://PepCalc.com). Of the 23 phages analyzed, 6 different peptides were isolated and 11 phages were found to be unmodified.

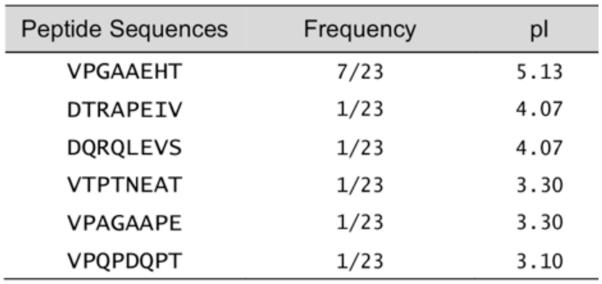

Peptide Sequences	Frequency	pI
VPGAAEHT	7/23	5.13
DTRAPEIV	1/23	4.07
DQRQLEVS	1/23	4.07
VTPTNEAT	1/23	3.30
VPAGAAPE	1/23	3.30
VPQPDQPT	1/23	3.10

Table 5-2 Statistical analysis of peptides obtained after 5 rounds of biopanning. The frequency of each amino acid occurrence at each position and within all resulting sequences was calculated. The amino acids are presented in single letter form and color coded according to its chemical moieties. Data associated with the 11 unmodified phage were not included in this analysis.

Amino Acid	Percentage of frequency at each position in peptide (%)								Frequency of occurrence (%)	
	1	**2**	**3**	**4**	**5**	**6**	**7**	**8**	against ZnO	in library
F	0	0	0	0	0	0	0	0	0	0.3
W	0	0	0	0	0	0	0	0	0	0
M	0	0	0	0	0	0	0	0	0	3.8
P	0	75	8	8	8	0	17	0	14.6	11.5
H	0	0	0	0	0	0	58	0	7.3	0.7
K	0	0	0	0	0	0	0	0	0	0.7
R	0	0	17	0	0	0	0	0	2.1	1.7
N	0	0	0	0	8	0	0	0	1.0	2.8
Q	0	8	8	8	0	8	0	0	4.2	3.8
E	0	0	0	0	0	83	0	8	11.5	11.1
D	17	0	0	0	8	0	0	0	3.1	8.0
V	83	0	0	0	0	0	8	8	12.5	6.3
G	0	0	58	8	0	0	0	0	8.3	9.7
A	0	0	8	67	67	8	8	0	19.8	12.8
I	0	0	0	0	0	0	8	0	1.0	0.7
L	0	0	0	0	8	0	0	0	1.0	6.6
Y	0	17	0	8	0	0	0	75	12.5	8.7
S	0	0	0	0	0	0	0	8	1.0	10.8
T	0	0	0	0	0	0	0	0	0	0
C	0	0	0	0	0	0	0	0	0	0
	V	**P**	**G**	**A**	**A**	**E**	**H**	**T**	**Consensus**	

Although not exactly identical, hydrophobic (V, G, A, I, L) and negatively charged (E, D) amino acids were observed at similar high frequency in both biopanning results and the pVIII library. This is largely affected by the characteristic of the pVIII protein coat which assembles readily when displaying hydrophobic and negatively charged residues. Notably, high percentage of histidine (H), 10-fold greater than in the pVIII library was obtained, consistent to other reports emphasizing histidine's role in ZnO affinity. The consensus sequence, determined by ordering the most frequent residue in each position, was concurred with the recurrent peptide sequence (VPGAAEHT).

The affinity of the ZnO-binding phage was evaluated via binding study. Figure 5-2 (b) shows the average binding strength of the ZnO-binding and wild-type phages for ZnO, respectively. The ZnO-binding phage was found to have an affinity for ZnO which was 228 times larger than that of the wild-type phage. Moreover, as depicted in Figure 5-2 (b) (inset), immediate agglomeration was observed when the ZnO-binding phages were added to a nanoparticle suspension. It is notable that the affinity of the identified ZnO-binding phage was robust, demonstrating binding capability for three different forms of ZnO: powder, nanoparticles, and thin film.

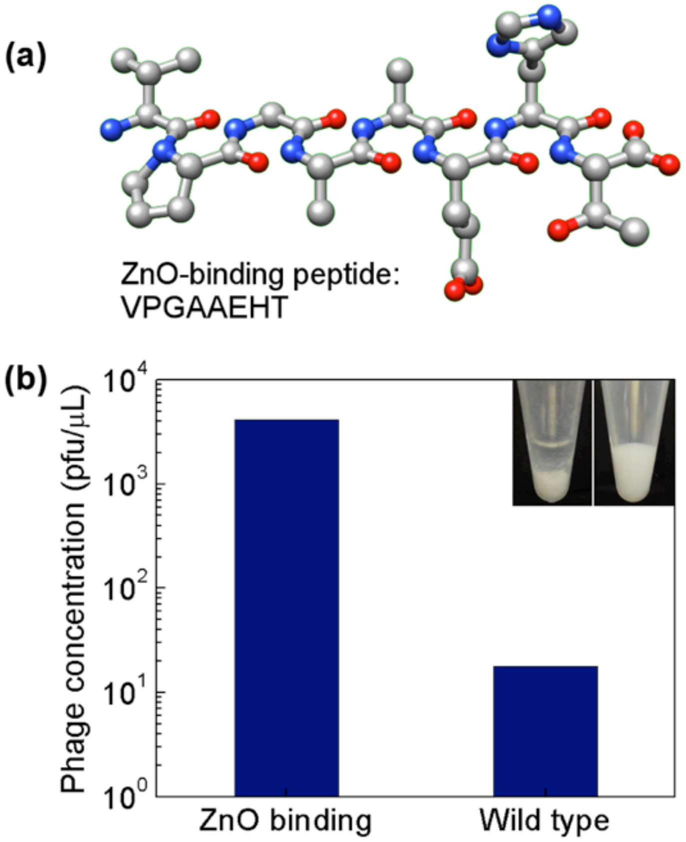

Figure 5-2 (a) Ball-and-stick model of identified ZnO-binding peptide sequence, VPGAAEHT. (b) The binding strength of the ZnO-binding and the wild-type phages for ZnO. Inset shows optical images of ZnO nanoparticle dispersion (left) with and (right) without the addition of the ZnO-binding phage.

The ability of ZnO-binding phage to template mineralization of 1D ZnO nanomaterials was studied. Table 5-3 summarizes the different precursor, temperature, and incubation times researched. At low temperature conditions, non-crystalline materials were obtained rather than crystalline ZnO materials as desired. In contrast high temperature conditions, resulted in large micron-sized crystalline material, where viral-templated synthesis was difficult to determine. Linear chains of nanocrystalline material was obtained with 100 mM $Zn(OH)_2$ at 40°C in PCR machine, however similar morphologies were obtained even without the ZnO-binding phage, eliminating the phage directed mineralization.

Table 5-3 Summary of nucleation conditioned using ZnO-binding phage in solution.

Precursor	Concentration	Temperature	Morphology
$Zn(NO_3)_2 \bullet H_2O$	10 mM, 4 days	RT	- Small particles not associated with phage - Non-crystalline material on phage agglomerate
$Zn(NO_3)_2 \bullet H_2O$	10 mM, 3 weeks	RT	- Non-crystalline material and particles on phage agglomerate - Few particles without clear phage association
$Zn(NO_3)_2 \bullet H_2O$	10 mM, 6 weeks	RT	- Non-crystalline material and particles on phage agglomerate - More than 3 weeks sample
$Zn(NO_3)_2 \bullet H_2O$ + HMTA	10 mM, 3 days	RT	- Non-crystalline material and particles on phage agglomerate
	100 mM, 3 days	RT	- Non-crystalline material and particles on phage agglomerate - Few dense particles
	1 mM, 24h + 72h	RT + 65°C	- Few peanut-like crystals (~4 μm) - Agglomerate of short hexagonal rods (~2 μm)
	10 mM, 24h + 2h	RT + 65°C	- Spindles-like structures (few μm)
	10 mM, 24h + 24h	RT + 65°C	- Hexagonal pointy rods (> 10 μm)
	10 mM, 24h + 72h	RT + 65°C	- Hexagonal pointy rods (> 10 μm)
	50 mM, 24h + 2h	RT + 65°C	- Hexagonal rods (2-5 μm)
	50 mM, 24h + 24h	RT + 65°C	- Hexagonal rods (3-10 μm)
	50 mM, 24h + 72h	RT + 65°C	- Hexagonal rods (5-10 μm)
	1 mM, 24h	65°C	- Peanut-like structures (few μm)
	10 mM, 1h	65°C	- Spindles (~1-3 μm)
	10 mM, 6h	65°C	- Elongated spindles (2-5 μm)
	10 mM, 24h	65°C	- Hexagonal rods (3-6 μm)
$Zn(NO_3)_2 \bullet H_2O$ + KOH	1 mM/2 mM, 95h	RT	- Dense non-crystalline material and particles on phage agglomerate
	10 mM/20 mM, 95h	RT	- Dense non-crystalline material and particles on phage agglomerate - Few dense particles on agglomerate
	100 mM/200 mM, 5m	40°C	- Agglomerate of nanocrystal chains (~10 nm)

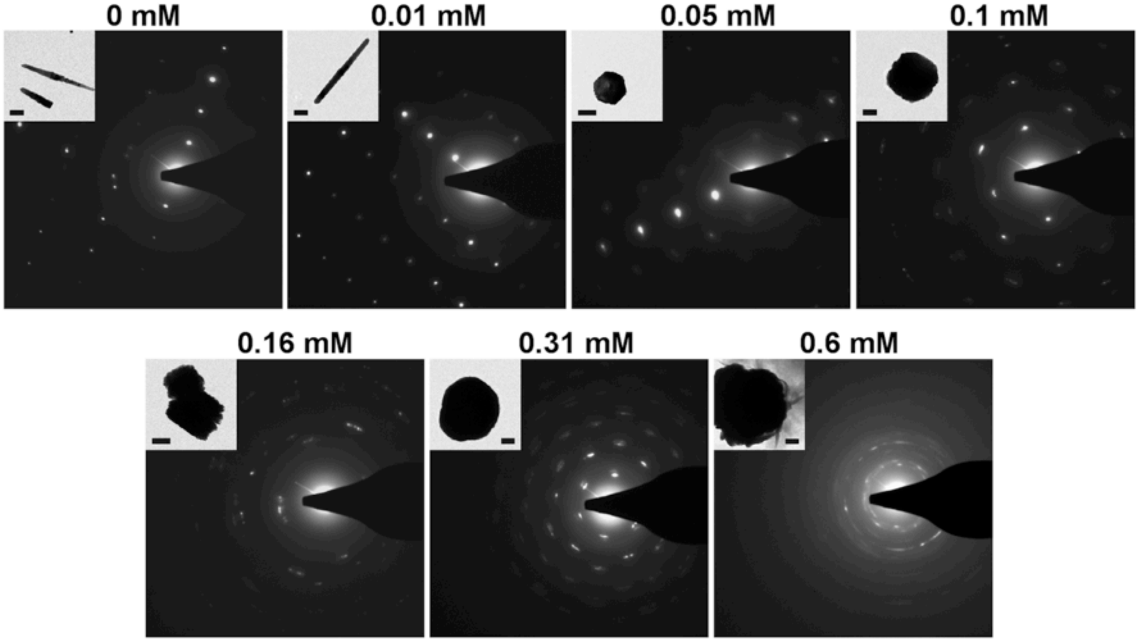

Figure 5-3 Transmission electron microscopy (TEM) images (inset, scale bar: 0.5 μm) and corresponding electron diffraction patterns of ZnO nanostructures synthesized with varied peptide concentrations.

To study the effects on ZnO formation with free peptides, the ZnO-binding peptide with functional linker (-GGGSC) [28] was added during ZnO synthesis. $Zn(NO_3)_2$ and HMTA precursor concentrations were held constant at 50 mM, while the peptide concentration was varied from 0 to 0.6 mM. Figure 5-3 shows electron diffraction patterns and TEM images (inset) of the resulting nanostructured material for each synthesis condition. Although diverse particle morphologies were observed, a diffraction pattern consistent with wurtzite ZnO was obtained for all samples [149]. A transition from single- to poly-crystalline material was apparent for peptide concentrations ≥ 0.1 mM. Elemental analysis of all samples using EDS revealed Zn and

O peaks in addition to grid-related Cu, C, and O peaks. Representative EDS spectra of structures formed with the addition of 0 mM and 0.6 mM peptide are shown in Figure 5-4.

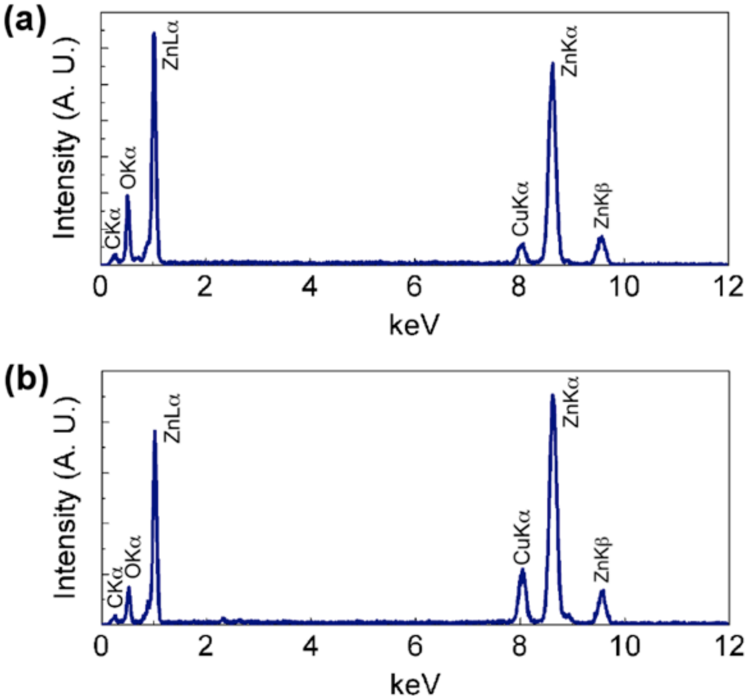

Figure 5-4 Representative energy dispersive x-ray spectra (EDS) of peptide-assisted structures synthesized with (a) no peptide and (b) 0.6 mM ZnO-binding peptide on carbon-coated copper TEM grid.

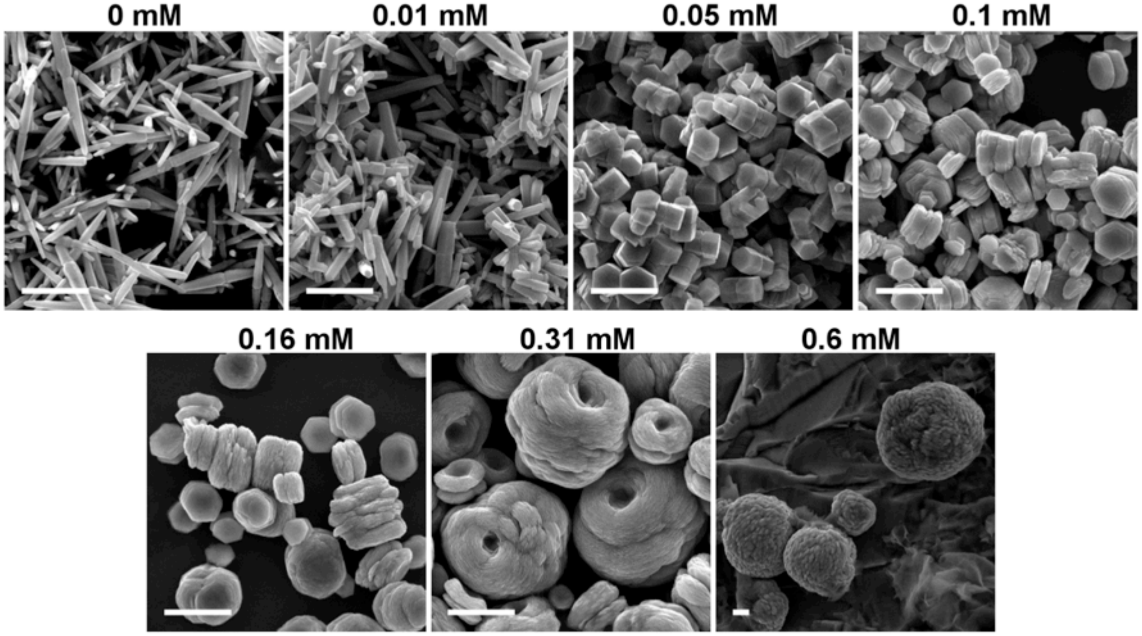

Figure 5-5 Scanning electron microscopy (SEM) images of ZnO nanostructures synthesized with the addition of varied peptide concentrations (scale bar: 2 μm).

SEM images of the ZnO materials are shown in Figure 5-5. Material synthesized without peptides had a hexagonal needle-like structure [31, 150]. With the addition of peptides, this morphology changed to flat-ended rods and, at high peptide concentrations, to microspheres. At or below 0.05 mM, the observed ZnO structures retained hexagonal facets but decreased in aspect ratio from 11 to 1.6 with increasing peptide concentration, as shown in Figure 5-6. A similar morphological change has also been observed in synthesis aided by a handful of previously-reported, basic peptides with ZnO affinity [31, 151]. These peptides displayed preferential binding on (0001) planes which inhibited or slowed c-axis growth, causing for the formation of plates. Interestingly, for one of these peptides, the use of the –GGGC linker increased binding selectivity for the (0001) places and further reduced aspect ratio [147]. Although histidine and cysteine are known to complex with Zn^{2+}, particularly in zinc finger proteins, histidine or cysteine monomers do not induce a needle to rod transition [144, 150]. Moreover, only a handful of histidine-containing dipeptides, composed of only two amino acids, have been shown to cause such a change [150]. As such, the single histidine residue within the VPGAAEHT sequence or the cysteine residue within the linker were not likely alone responsible for the morphological change observed here, but rather the combination of amino acids within the discovered ZnO-binding peptide influenced crystal growth collectively. Above 0.05 mM, layered (0.1 mM, 0.16 mM), yarn-like (0.31 mM), and microsphere (0.6 mM) morphologies composed of smaller, hierarchically arranged particles were found. This morphological observation corroborated the increased polycrystallinity in the electron diffraction data. The assembly of smaller ZnO nanoparticles into larger structures such as flowers [28] and olives [134] has also been observed under different bio-assisted synthesis conditions. In addition to the capping effect mentioned previously, the rise of peptide-peptide interactions at higher peptide concentrations likely promoted this kind of long-range organization [152, 153].

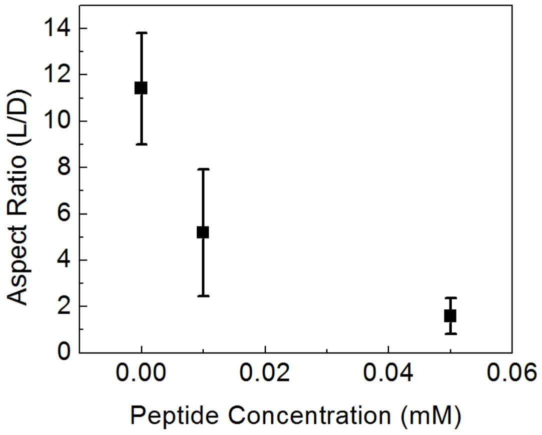

Figure 5-6 Aspect ratio (Length/Diameter) of ZnO structures synthesized with the addition of peptide concentrations from 0 to 0.05 mM.

It is notable that the morphological changes seen with the 8-mer acidic peptide were more significant than those recorded for 12-mer basic peptides [31, 147]. Under similar peptide concentrations and synthesis conditions, highly investigated basic peptides supported an aspect ratio change from needle to plate, whereas the 8-mer acidic peptide moved beyond a simple difference in height-width relationship forming more complex structures.

To assess peptide adsorption or incorporation in the peptide-assisted ZnO nanostructures, FTIR analysis was performed. Representative spectra in the wavenumber region of interest appear in Figure 5-7. Peptide characteristic amide I and amide II absorption peaks at 1500-1600 cm^{-1} and 1600-1700 cm^{-1}, respectively, were observed in the peptide alone and ZnO structures formed in presence of 0.1 mM ZnO-binding peptide. Notably, the amide II shifted from ~1670 cm^{-1} in the peptide only sample to

1645 cm^{-1} in the peptide-assisted ZnO structure, suggesting peptide adsorption onto the ZnO materials [147, 154]. ZnO synthesized without peptide did not show amide absorption peaks, however, broad features were present in the 1300-1450 cm^{-1} range which were also seen in the 0.1 mM peptide-assisted ZnO materials. Although exact attribution of these peaks needs to be elucidated, absorption of CO_2^-, CO_3^{2-}, and CH_3, and NO_3 which could be related to ZnO intermediate states have been reported within this range [144, 154].

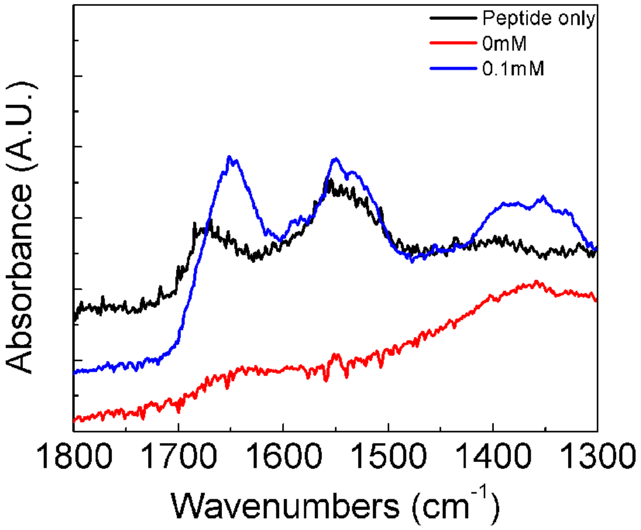

Figure 5-7 Fourier transform infrared (FTIR) spectra of ZnO-binding peptide (black) and ZnO nanostructures prepared with no peptide (red) and 0.1 mM peptide (blue). The absorbance of the ZnO-binding peptide spectrum was multiplied by 3 to aid in visualization.

Optical behavior of ZnO materials synthesized with peptide additives was investigated using photoluminescence measurements. Figure 5-8 shows the normalized emission spectra of the ZnO structures synthesized with different peptide concentrations.

The spectra of material synthesized without peptides and with peptide concentrations of 0.1 mM or less, showed a distinct peak near 380 nm, which was consistent with ZnO band-edge emission (3.2-3.4 eV). ZnO materials prepared without peptides also displayed strong green emission between 520 and 545 nm associated with electron-hole recombination at deep level defects such as surface-related oxygen and zinc vacancies [155]. Notably this green emission peak was reduced in samples synthesized with peptides and decreased with increasing peptide concentration, suggesting a reduction of oxygen and zinc vacancy-related defects within the ZnO material synthesized with peptide additives. At a peptide concentration of 0.05 mM, an increase in emission at wavelengths slightly longer than the band edge peak was also observed. At peptide concentrations more than 0.31 mM, this 400 nm peak increased substantially, obscuring the band edge emission. This sub-bandgap emission likely represented shallow donor to valence band and/or shallow acceptor to conduction band transitions of Zn_i and O_i interstitials, respectively [156]. Similar dominance of visible emission was observed from ZnO nanoparticles formed in presence of spider silk peptides, as well as through some non-biological processes [134, 157]. A band diagram displaying possible sub-bandgap defect states are shown in Figure 5-9. Peptide-assisted ZnO synthesis using the identified ZnO-binding peptide (VPGAAEHT) allowed hierarchical assembly of nanoscale ZnO that showed distinct, morphology-dependent optical emission properties.

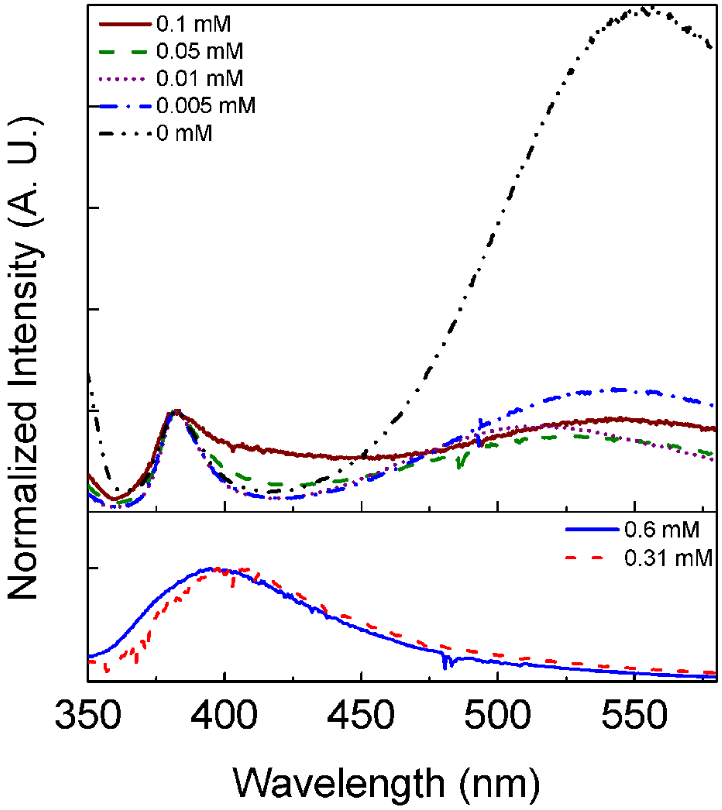

Figure 5-8 Photoluminescence (PL) spectra of ZnO nanostructures formed with different peptide concentrations: (top) 0, 0.005, 0.01, 0.05, 0.1, and (bottom) 0.31, 0.6 mM. Emission intensity was normalized to the band-edge or near band-edge peak.

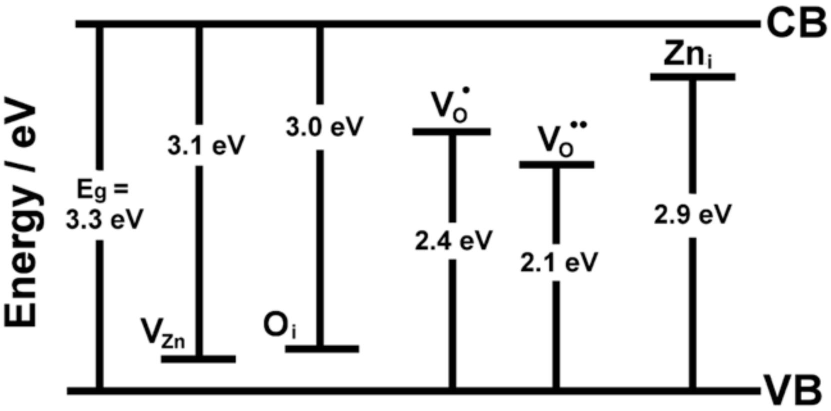

Figure 5-9 Schematic band diagram of intrinsic sub-bandgap defect levels in ZnO.

A film of ZnO nanostructures (0.1 mM peptide) was on a set of 200 μm gap gold electrodes by O_2 plasma treating the surface and incubating for 1 h, similar to the 3 μm gap devices in Chapter 2. The electrical resistance varied from a few MΩ to 100s MΩ range and displayed Schottky IV characteristics. Sensing analysis against NH_3 was tested at room temperature, but no definitive sensing response was obtained (data not shown). Sensor operation at room temperature is reported as one of the major challenges for metal oxide-based sensors including ZnO. To overcome this limitation, defect or light-aided approaches have been taken. To assess the potential of these bio-directed ZnO materials for such approaches, real-time photocurrent measurement of 0.1 mM ZnO film with green light (527 nm) illumination were taken and are shown in Figure 5-10. When green light was illuminated, the resistance decreased notably and increased back in dark, consistent to other reports [158, 159]. Although the recovery of resistance during the dark phase wasn't 100% during the first cycle, the recovery in following cycles was improved. Most reports on light-aided sensor improvement use above band-gap UV-light to create electron-hole pairs by promoting valence electrons to the conduction band. However, this ZnO film displayed photoresponse even to visible, green-light illumination. We attribute the this photoreseponse to the electron-hole pairs generated by defect to conduction band transitions, which in return enhance carrier concentration in ZnO for better conduction. While further studies are required to better understand the material defect states and their role in electrical conduction, photoresponse, and gas sensing, peptide-directed polycrystalline ZnO shows potential in visible light-aided gas sensor applications.

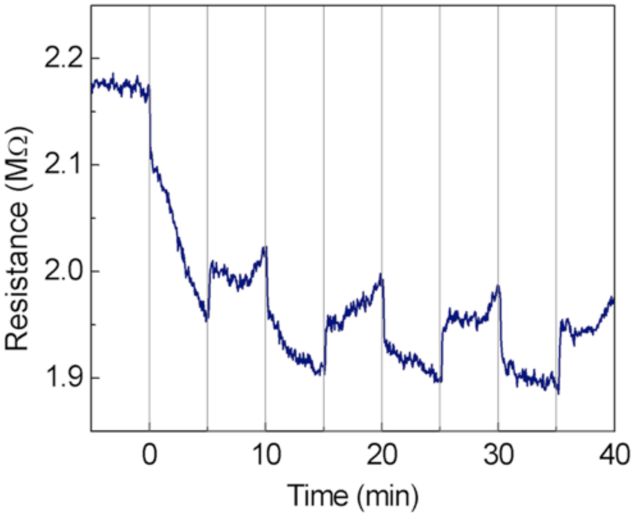

Figure 5-10 Photoresponse of ZnO film composed of nanostructures synthesized with 0.1 mM peptide to illumination of 527 nm green light. Constant bias of 0.15 V was applied. Light turned on at t=0 and turned off after 5 min. Five min cycles of on/off repeated 4 times.

5.4 Conclusion

In summary, a combinatorial pVIII phage display library, in which display of neutral and acidic peptides was favored, was used to find a peptide with an affinity for ZnO. When added during synthesis, this ZnO-binding peptide exhibited control over ZnO nanostructure crystallinity, morphology, and photoluminescence behavior. Higher peptide concentrations triggered an evolution from single crystal to polycrystalline particles and a range of concentration-dependent ZnO nanostructures including rods, platelets, yarn-like shapes, and microspheres was observed. Photoluminescence spectra of materials synthesized with the ZnO-binding peptide showed decreased green emission from surface-related oxygen and zinc vacancies as compared to materials synthesized without peptides. And, at greatly increased peptide concentrations, blue emission from interstitial defects acting as shallow donors and acceptors increased. The current-voltage measurement on the 0.1 mM ZnO film was a Schottky behavior and the resistance ranged from a few MΩ to 100s MΩ. Room-temperature sensing response to NH_3 was not observed in the concentrations tested. However, decrease of device resistance was observed with each green-light (527 nm) illumination caused by carrier transition from sub-bandgap deep-level defect to the valence band. Although further studies are necessary to elucidate specific mechanisms which enable adjustment of morphology, sub-bandgap emission, and photoresponse, this study demonstrates the potential control of these properties offered by peptide-mediated growth. Engineered morphology and defect levels are valuable for ZnO gas sensing and photocatalytic materials design.

Chapter 6. Conclusion

In this dissertation, we have developed a bio-direct approach to meet nanofabrication challenges for sensitive metal and metal oxide chemiresistive gas sensors. The M13 bacteriophage template enabled bottom-up assembly of nanomaterials in dimensions that are difficult to obtain. Nanomaterials with high surface area increased analyte binding sites and decreased diffusion length for greater sensitivity. Highly sensitive H_2S and H_2 gas sensors were synthesized from gold nanoparticle chains and gold-palladium nanopeapods, respectively. Bio-assisted ZnO synthesis was explored and ZnO structures with tunable morphological and optical properties were presented for future sensor applications.

We developed a relatively simple device fabrication platform to incorporate the filamentous M13 bacteriophage into miniature gas sensor devices. Gold-binding bacteriophage was used as the backbone for linear arrangement of gold nanoparticles, which were used as seeds for continuous nanowires. The size of gold nanoparticles was controlled by electroless deposition, which affected nanoparticle-nanoparticle connection and the electrical conduction through these nanowires. The concentration of phage also affected the electrical conductivity by adjusting surface coverage of nanowires on the device. The as-assembled viral-templated gold nanowire sensors were highly sensitive to H_2S gas at room temperature exhibiting sensitivity of 654 %/ppm, lowest detection limit of 2 ppb, and recovery of 70% within 9 min. Once the template was removed through oxygen plasma and ethanol dip treatment, the device performance dropped significantly: sensitivity of 6 %/ppm (100-fold lower), the lowest limit of detection of 6 ppb (3-fold higher), and did not show any recovery during air purge. The gold-binding phage template was not merely a backbone for assembly, but had an important role in analyte adsorption/desorption. We attribute this to the carboxyl groups on acidic amino acids as well as amine groups on the n-terminus of the viral-template that are reported for sulfur affinity. In addition, virus and its protein interaction on gold nanoparticles likely inhibited permanent binding of sulfur atoms on the gold sensor surfaces enabling reversibility.

The bio-directed sensor fabrication platform was adapted for synthesis of hybrid gold-palladium nanopeapod based chemiresistive H_2 gas sensor. The linearly arranged gold nanoparticles were again used as seeds to deposit palladium shells. The thickness of the palladium shells was controlled by electroless deposition cycles, and thick (~15 nm) and thin (~5 nm) shelled sensors were tested. The electrical resistance was dependent on palladium shell thickness, decreasing in average by five orders of magnitude. Contrary to reported, thick nanopeapod devices displayed decrease in resistance with low concentration H_2 exposure and did not display recovery. Conditioning of the sensor by prolonged exposure of high H_2 concentration revealed presence of palladium oxide (PdO) layer formed during synthesis and sensing response of 0.04% to 2.6% at 2000 ppm were obtained there onward. However, thin nanopeapod devices displayed high response to H_2 from 50 to 2000 ppm. A high response of 117% was obtained at 2000 ppm and the lowest detection limit was calculated as 25 ppm. Here, the biological template enabled assembly of tenuously connected gold-palladium nanowires with controlled shell thickness. The thin palladium shell of few nanometers was critical for sensing low concentrations of H_2 gas in air and room temperature. It decreased PdO surface layer and diffusion length allowing efficient H_2 diffusion over oxygen species.

Moving away from metals, zinc oxide (ZnO) nanomaterials were studied for chemiresistive gas sensing. A previously publish 12-mer peptide was genetically and chemically displayed on the pIII and the pVIII coat proteins, respectively. ZnO nanocrystals independent of incubation time and precursor concentration was formed on pIII end of the genetically modified ZnO-binding phage. The particles were highly polydisperse and the yield was relatively low. The 12-mer peptide was covalently conjugated on the pVIII coat protein using the bi-functional sulfo-SMCC crosslinker. The peptide was successfully bioconjugated on the pVIII coat protein, however 100% coverage was difficult to obtain due to steric hindrance. The reduced electrostatic repulsion resulted flocculation of phages and with mineralization, film of ZnO rather than viral-templated 1D nanostructures. These studies demonstrated ZnO mineralization on different protein coats and promise of chemical modification method to display longer, highly positively charged peptides.

A pVIII library display 8-mer peptides were used in combinatorial phage display screening for a ZnO-binding peptide. One peptide, VPGAAEHT, occurred 7 out of the 12 phages and was the consensus sequence. The ZnO-binding phage displayed a relatively high isoelectric point of 5.13, than all the other sequences observed which were more acidic. ZnO nanomaterials were synthesized with peptide additive from 0 to 0.6

mM. Peptide addition decrease the aspect ratio of crystals from rods to platelets, and above 0.1 mM polycrystalline layered, yarn-like, and microscphere were formed. In addition, photoluminescence spectra displayed peptide tuning of material defect levels. At no or low peptide addition, near-band edge emission and oxygen vacancy-related green emission peaks were observed. With peptide addition, the green emission peak decreased significantly suggesting reduced oxygen defects. Further tuning was observed at high peptide concentrations, where visible blue emission dominated the spectra. The broad visible light emission suggested presence of other sub-bandgap defects that can be favorable for gas sensor applications. Peptide-directed ZnO displayed photoresponse to 527 nm, green light which induced enhanced conductivity. The defect manipulation from peptides and its photoresponse to visible suggests potential use of peptide-directed ZnO nanomaterials for chemiresistive gas sensing.

Chapter 7. Future Work

This dissertation presented promise of bio-directed bottom-up assembly of inorganic nanomaterials for electrical devices, particularly chemiresistive sensor devices. The M13 bacteriophage and its peptide components have been utilized as a template, sensitizer, and additive in nano-chemiresistive gas sensors. The relatively simple device fabrication platform can be expanded for assembly of other materials and core-shell structures for nanodevice fabrication. For chemiresistive sensing, further studies are required to decrease the response and recovery times of the devices. The random network provides large surface area, however could result in many adsorption sites that does not change the conductivity. Therefore, methods to control the number of connection or perhaps align the conductive pathways could be studied. Furthermore, as shown in the results, the number of connections dictated the electrical resistance of the devices, which influences sensor performances.

Mineralization of ZnO different coat proteins have been demonstrated using genetically and chemically modified M13 bacteriophage template. One major challenge was the flocculation or agglomeration of phages as observed with the chemically modified ZnO-binding peptide-conjugated phage and genetically modified ZnO-binding phage. Mineralization on agglomeration of both phages was successfully obtained. Therefore, methods to increase or control electrostatic repulsion between the phages will allow synthesis of 1D ZnO nanostructures. The mechanism of peptide-assisted tuning of

ZnO materials properties needs further elucidation. With better understanding, this controlled mineralization can be used to tune sub-bandgap defect levels and in return, optical and electrical properties of ZnO to improve sensor performance at room temperature, as well as for other desired applications. Furthermore, combination of Au assembly and ZnO mineralization to create hybrid Au-ZnO nanostructures is promising for optoelectronic, photocatalytic and gas sensor device applications as Au has been extensively used as a catalyst for such applications.

References

[1] Schaffer T E, IonescuZanetti C, Proksch R, Fritz M, Walters D A, Almqvist N, Zaremba C M, Belcher A M, Smith B L, Stucky G D, Morse D E and Hansma P K 1997 Does abalone nacre form by heteroepitaxial nucleation or by growth through mineral bridges? *Chemistry of Materials* **9** 1731-40

[2] Morse D E 1999 Silicon biotechnology: harnessing biological silica production to construct new materials *Trends in Biotechnology* **17** 230-2

[3] Schuler D and Frankel R B 1999 Bacterial magnetosomes: microbiology, biomineralization and biotechnological applications *Applied Microbiology and Biotechnology* **52** 464-73

[4] Fincham A G, Moradian-Oldak J and Simmer J P 1999 The structural biology of the developing dental enamel matrix *Journal of Structural Biology* **126** 270-99

[5] Dong Q, Su H, Xu J and Zhang D 2007 Influence of hierarchical nanostructures on the gas sensing properties of SnO2 biomorphic films *Sensors and Actuators B-Chemical* **123** 420-8

[6] Yang F, Su H, Zhu Y, Chen J, Lau W M and Zhang D 2013 Bioinspired synthesis and gas-sensing performance of porous hierarchical alpha-Fe2O3/C nanocomposites *Scripta Materialia* **68** 873-6

[7] Huang J, Wang X and Wang Z L 2006 Controlled replication of butterfly wings for achieving tunable photonic properties *Nano Letters* **6** 2325-31

[8] Ota T, Imaeda M, Takase H, Kobayashi M, Kinoshita N, Hirashita T, Miyazaki H and Hikichi Y 2000 Porous titania ceramic prepared by mimicking silicified wood *Journal of the American Ceramic Society* **83** 1521-3

[9] Richter J, Seidel R, Kirsch R, Mertig M, Pompe W, Plaschke J and Schackert H K 2000 Nanoscale palladium metallization of DNA *Advanced Materials* **12** 507-+

[10] Zhou J C, Gao Y, Martinez-Molares A A, Jing X, Yan D, Lau J, Hamasaki T, Ozkan C S, Ozkan M, Hu E and Dunn B 2008 Microtubule-based gold nanowires and nanowire arrays *Small* **4** 1507-15

[11] Hartgerink J D, Beniash E and Stupp S I 2001 Self-assembly and mineralization of peptide-amphiphile nanofibers *Science* **294** 1684-8

[12] Lim J-S, Kim S-M, Lee S-Y, Stach E A, Culver J N and Harris M T 2010 Biotemplated Aqueous-Phase Palladium Crystallization in the Absence of External Reducing Agents *Nano Letters* **10** 3863-7

[13] Huang Y, Chiang C Y, Lee S K, Gao Y, Hu E L, De Yoreo J and Belcher A M 2005 Programmable assembly of nanoarchitectures using genetically engineered viruses *Nano Letters* **5** 1429-34

[14] Naik R R, Stringer S J, Agarwal G, Jones S E and Stone M O 2002 Biomimetic synthesis and patterning of silver nanoparticles *Nature Materials* **1** 169-72

[15] Atanasova P, Rothenstein D, Schneider J J, Hoffmann R C, Dilfer S, Eiben S, Wege C, Jeske H and Bill J 2011 Virus-Templated Synthesis of ZnO Nanostructures and Formation of Field-Effect Transistors *Advanced Materials* **23** 4918-22

[16] Naik R R, Brott L L, Clarson S J and Stone M O 2002 Silica-precipitating peptides isolated from a combinatorial phage display peptide library *Journal of Nanoscience and Nanotechnology* **2** 95-100

[17] Park S J, Lazarides A A, Mirkin C A, Brazis P W, Kannewurf C R and Letsinger R L 2000 The electrical properties of gold nanoparticle assemblies linked by DNA *Angewandte Chemie-International Edition* **39** 3845-+

[18] Lee D, Choe Y J, Choi Y S, Bhak G, Lee J and Paik S R 2011 Photoconductivity of Pea-Pod-Type Chains of Gold Nanoparticles Encapsulated within Dielectric Amyloid Protein Nanofibrils of alpha-Synuclein *Angewandte Chemie-International Edition* **50** 1332-7

[19] Patolsky F, Weizmann Y, Lioubashevski O and Willner I 2002 Au-nanoparticle nanowires based on DNA and polylysine templates *Angewandte Chemie-International Edition* **41** 2323-7

[20] Nam K T, Kim D W, Yoo P J, Chiang C Y, Meethong N, Hammond P T, Chiang Y M and Belcher A M 2006 Virus-enabled synthesis and assembly of nanowires for lithium ion battery electrodes *Science* **312** 885-8

[21] Lee S W, Mao C B, Flynn C E and Belcher A M 2002 Ordering of quantum dots using genetically engineered viruses *Science* **296** 892-5

[22] Barbas C F I, Burton D R, Scott J K and Silverman G J 2000 *Phage Display: A Laboratory Manual* (Cold Spring Harbor, New York: Cold Spring Harbor Laboratory Press)

[23] Sidhu S S 2001 Engineering M13 for phage display *Biomolecular Engineering* **18** 57-63

[24] Pettersen E F, Goddard T D, Huang C C, Couch G S, Greenblatt D M, Meng E C and Ferrin T E 2004 UCSF chimera - A visualization system for exploratory research and analysis *Journal of Computational Chemistry* **25** 1605-12

[25] Slocik J M, Stone M O and Naik R R 2005 Synthesis of gold nanoparticles using multifunctional peptides *Small* **1** 1048-52

[26] Chiu C-Y, Li Y, Ruan L, Ye X, Murray C B and Huang Y 2011 Platinum nanocrystals selectively shaped using facet-specific peptide sequences *Nature Chemistry* **3** 393-9

[27] Whaley S R, English D S, Hu E L, Barbara P F and Belcher A M 2000 Selection of peptides with semiconductor binding specificity for directed nanocrystal assembly *Nature* **405** 665-8

[28] Umetsu M, Mizuta M, Tsumoto K, Ohara S, Takami S, Watanabe H, Kumagai I and Adschiri T 2005 Bioassisted room-temperature immobilization and mineralization of zinc oxide - The structural ordering of ZnO nanoparticles into a flower-type morphology *Advanced Materials* **17** 2571-+

[29] Mao C B, Solis D J, Reiss B D, Kottmann S T, Sweeney R Y, Hayhurst A, Georgiou G, Iverson B and Belcher A M 2004 Virus-based toolkit for the directed synthesis of magnetic and semiconducting nanowires *Science* **303** 213-7

[30] Flynn C E, Mao C B, Hayhurst A, Williams J L, Georgiou G, Iverson B and Belcher A M 2003 Synthesis and organization of nanoscale II-VI semiconductor materials using evolved peptide specificity and viral capsid assembly *Journal of Materials Chemistry* **13** 2414-21

[31] Tomczak M M, Gupta M K, Drummy L F, Rozenzhak S M and Nalk R R 2009 Morphological control and assembly of zinc oxide using a biotemplate *Acta Biomaterialia* **5** 876-82

[32] Petrenko V A, Smith G P, Gong X and Quinn T 1996 A library of organic landscapes on filamentous phage *Protein Engineering* **9** 797-801

[33] Zaman M S, Moon C H, Bozhilov K N and Haberer E D 2013 Phage-directed synthesis of copper sulfide: structural and optical characterization *Nanotechnology* **24**

[34] Lee S K, Yun D S and Belcher A M 2006 Cobalt ion mediated self-assembly of genetically engineered bacteriophage for biomimetic Co-Pt hybrid material *Biomacromolecules* **7** 14-7

[35] Aswal D K, Gupta, Shiv K. 2007 *Science and Technology of Chemiresistor Gas Sensors* (New York: Nova Science Publishers, Inc.)

[36] Mubeen S, Lim J-H, Srirangarajan A, Mulchandani A, Deshusses M A and Myung N V 2011 Gas Sensing Mechanism of Gold Nanoparticles Decorated Single-Walled Carbon Nanotubes *Electroanalysis* **23** 2687-92

[37] Mubeen S, Zhang T, Chartuprayoon N, Rheem Y, Mulchandani A, Myung N V and Deshusses M A 2010 Sensitive Detection of H2S Using Gold Nanoparticle Decorated Single-Walled Carbon Nanotubes *Analytical Chemistry* **82** 250-7

[38] Penza M, Rossi R, Alvisi M, Cassano G and Serra E 2009 Functional characterization of carbon nanotube networked films functionalized with tuned loading of Au nanoclusters for gas sensing applications *Sensors and Actuators B-Chemical* **140** 176-84

[39] Star A, Joshi V, Skarupo S, Thomas D and Gabriel J-C P 2006 Gas sensor array based on metal-decorated carbon nanotubes *Journal of Physical Chemistry B* **110** 21014-20

[40] Chung F-C, Wu R-J and Cheng F-C 2014 Fabrication of a Au@SnO2 core-shell structure for gaseous formaldehyde sensing at room temperature *Sensors and Actuators B-Chemical* **190** 1-7

[41] Dobrokhotov V, McIlroy D N, Norton M G, Abuzir A, Yeh W J, Stevenson I, Pouy R, Bochenek J, Cartwright M, Wang L, Dawson J, Beaux M and Berven C 2006 Principles and mechanisms of gas sensing by GaN nanowires functionalized with gold nanoparticles *Journal of Applied Physics* **99**

[42] Choi S-W and Kim S S 2012 Room temperature CO sensing of selectively grown networked ZnO nanowires by Pd nanodot functionalization *Sensors and Actuators B-Chemical* **168** 8-13

[43] Shirsat M D, Bangar M A, Deshusses M A, Myung N V and Mulchandani A 2009 Polyaniline nanowires-gold nanoparticles hybrid network based chemiresistive hydrogen sulfide sensor *Applied Physics Letters* **94** 083502

[44] Krasteva N, Guse B, Besnard I, Yasuda A and Vossmeyer T 2003 Gold nanoparticle/PPI-dendrimer based chemiresistors Vapor-sensing properties as a function of the dendrimer size *Sensors and Actuators B-Chemical* **92** 137-43

[45] Yoo K S, Sorensen L W and Glaunsinger W S 1994 ADHESION, SURFACE-MORPHOLOGY, AND GAS-SENSING CHARACTERISTICS OF THIN-GOLD-FILM CHEMICAL SENSORS *Journal of Vacuum Science & Technology a-Vacuum Surfaces and Films* **12** 192-8

[46] Lee J, Mubeen S, Hangarter C M, Mulchandani A, Chen W and Myung N V 2011 Selective and Rapid Room Temperature Detection of H2S Using Gold Nanoparticle Chain Arrays *Electroanalysis* **23** 2623-8

[47] Geng J F, Thomas M D R, Shephard D S and Johnson B F G 2005 Suppressed electron hopping in a Au nanoparticle/H2S system: development towards a H2S nanosensor *Chemical Communications* 1895-7

[48] Lewis F A 1967 *The palladium hydrogen system* (London: Academic Press)

[49] Hughes R C and Schubert W K 1992 THIN-FILMS OF PD/NI ALLOYS FOR DETECTION OF HIGH HYDROGEN CONCENTRATIONS *Journal of Applied Physics* **71** 542-4

[50] Wagner S, Hamm M and Pundt A 2013 Huge hydrogen-induced resistive switching in percolating palladium thin films *Scripta Materialia* **69** 756-9

[51] Kiefer T, Villanueva L G, Fargier F, Favier F and Brugger J 2010 The transition in hydrogen sensing behavior in noncontinuous palladium films *Applied Physics Letters* **97**

[52] Xu T, Zach M P, Xiao Z L, Rosenmann D, Welp U, Kwok W K and Crabtree G W 2005 Self-assembled monolayer-enhanced hydrogen sensing with ultrathin palladium films *Applied Physics Letters* **86**

[53] Im Y, Lee C, Vasquez R P, Bangar M A, Myung N V, Menke E J, Penner R M and Yun M H 2006 Investigation of a single Pd nanowire for use as a hydrogen sensor *Small* **2** 356-8

[54] Yang F, Taggart D K and Penner R M 2010 Joule Heating a Palladium Nanowire Sensor for Accelerated Response and Recovery to Hydrogen Gas *Small* **6** 1422-9

[55] Jeon K J, Lee J M, Lee E and Lee W 2009 Individual Pd nanowire hydrogen sensors fabricated by electron-beam lithography *Nanotechnology* **20**

[56] Lim M A, Kim D H, Park C-O, Lee Y W, Han S W, Li Z, Williams R S and Park I 2012 A New Route toward Ultrasensitive, Flexible Chemical Sensors: Metal Nanotubes by Wet-Chemical Synthesis along Sacrificial Nanowire Templates *Acs Nano* **6** 598-608

[57] Gupta D, Dutta D, Kumar M, Barman P B, Sarkar C K, Basu S and Hazra S K 2014 A low temperature hydrogen sensor based on palladium nanoparticles *Sensors and Actuators B-Chemical* **196** 215-22

[58] Wang C H, Chu X F and Wu M W 2006 Detection of H2S down to ppb levels at room temperature using sensors based on ZnO nanorods *Sensors and Actuators B-Chemical* **113** 320-3

[59] Belysheva T V, Bogovtseva L P, Kazachkov E A and Serebryakova N V 2003 Gas-sensing properties of doped In2O3 films as sensors for NO2 in air *Journal of Analytical Chemistry* **58**

[60] Zhang H, Xu C, Sheng P, Chen Y, Yu L and Li Q 2013 Synthesis of ZnO hollow spheres through a bacterial template method and their gas sensing properties *Sensors and Actuators B-Chemical* **181** 99-103

[61] Li Y, Gong J, He G and Deng Y 2012 Enhancement of photoresponse and UV-assisted gas sensing with Au decorated ZnO nanofibers *Materials Chemistry and Physics* **134** 1172-8

[62] Liu X, Zhang J, Guo X, Wu S and Wang S 2010 Amino acid-assisted one-pot assembly of Au, Pt nanoparticles onto one-dimensional ZnO microrods *Nanoscale* **2** 1178-84

[63] Dayan N J, Sainkar S R, Karekar R N and Aiyer R C 1998 Formulation and characterization of ZnO : Sb thick-film gas sensors *Thin Solid Films* **325** 254-8

[64] Ahn H, Wang Y, Jee S H, Park M, Yoon Y S and Kim D-J 2011 Enhanced UV activation of electrochemically doped Ni in ZnO nanorods for room temperature acetone sensing *Chemical Physics Letters* **511** 331-5

[65] Cui J, Wang D, Xie T and Lin Y 2013 Study on photoelectric gas-sensing property and photogenerated carrier behavior of Ag-ZnO at the room temperature *Sensors and Actuators B-Chemical* **186** 165-71

[66] Shao C, Chang Y and Long Y 2014 High performance of nanostructured ZnO film gas sensor at room temperature *Sensors and Actuators B-Chemical* **204** 666-72

[67] Wan Q, Li Q H, Chen Y J, Wang T H, He X L, Li J P and Lin C L 2004 Fabrication and ethanol sensing characteristics of ZnO nanowire gas sensors *Applied Physics Letters* **84** 3654-6

[68] Baratto C, Sberveglieri G, Onischuk A, Caruso B and di Stasio S 2004 Low temperature selective NO2 sensors by nanostructured fibres of ZnO *Sensors and Actuators B-Chemical* **100** 261-5

[69] Joshi R K, Hu Q, Am F, Joshi N and Kumar A 2009 Au Decorated Zinc Oxide Nanowires for CO Sensing *Journal of Physical Chemistry C* **113** 16199-202

[70] Ahn M W, Park K S, Heo J H, Park J G, Kim D W, Choi K J, Lee J H and Hong S H 2008 Gas sensing properties of defect-controlled ZnO-nanowire gas sensor *Applied Physics Letters* **93**

[71] Vanheusden K, Warren W L, Seager C H, Tallant D R, Voigt J A and Gnade B E 1996 Mechanisms behind green photoluminescence in ZnO phosphor powders *Journal of Applied Physics* **79** 7983-90

[72] Momma K and Izumi F 2011 VESTA 3 for three-dimensional visualization of crystal, volumetric and morphology data *Journal of Applied Crystallography* **44** 1272-6

[73] 2006 Toxicology profile for Hydrogen Sulfide. ed U.S. Department of Health and Human Services-Public Health Service (Agency for Toxic Substances and Disease Registry (ATSDR)

[74] 2005 Fact sheet of hydrogen sulfide (H_2S). Occupational Safety and Health Administration (OHSA))

[75] Pandey S K, Kim K-H and Tang K-T 2012 A review of sensor-based methods for monitoring hydrogen sulfide *Trac-Trends in Analytical Chemistry* **32**

[76] Datta N, Ramgir N, Kaur M, Ganapathi S K, Debnath A K, Aswal D K and Gupta S K 2012 Selective H2S sensing characteristics of hydrothermally grown ZnO-nanowires network tailored by ultrathin CuO layers *Sensors and Actuators B-Chemical* **166** 394-401

[77] Liu Y L, Wang H, Yang Y, Liu Z M, Yang H F, Shen G L and Yu R Q 2004 Hydrogen sulfide sensing properties of NiFe2O4 nanopowder doped with noble metals *Sensors and Actuators B-Chemical* **102** 148-54

[78] Leavitt A J and Beebe T P 1994 CHEMICAL-REACTIVITY STUDIES OF HYDROGEN-SULFIDE ON AU(111) *Surface Science* **314**

[79] Leiterer C, Berg S, Eskelinen A-P, Csaki A, Urban M, Torma P and Fritzsche W 2013 Assembling gold nanoparticle chains using an AC electrical field: Electrical detection of organic thiols *Sensors and Actuators B-Chemical* **176** 368-73

[80] 2014 *CRC Handbook of Chemistry and Physics 94th Edition (Internet Version 2014)* (Boca Raton, FL: CRC Press/Taylor and Fracis)

[81] Ding M, Sorescu D C, Kotchey G P and Star A 2012 Welding of Gold Nanoparticles on Graphitic Templates for Chemical Sensing *Journal of the American Chemical Society* **134**

[82] Song P, Wang Q and Yang Z 2012 Biomorphic synthesis and gas response of In2O3 microtubules using cotton fibers as templates *Sensors and Actuators B-Chemical* **168** 421-8

[83] Bruckman M A, Liu J, Koley G, Li Y, Benicewicz B, Niu Z and Wang Q 2010 Tobacco mosaic virus based thin film sensor for detection of volatile organic compounds *Journal of Materials Chemistry* **20** 5715-9

[84] Dong Q, Su H, Zhang D and Zhang F 2006 Fabrication and gas sensitivity of SnO2 hierarchical films with interwoven tubular conformation by a biotemplate-directed sol-gel technique *Nanotechnology* **17** 3968-72

[85] Peng W, Zhu C, Zhu S, Yao F, Li Y and Zhang D 2013 Biomimetic fabrication of alpha-Fe2O3 with hierarchical structures as H2S Sensor *Journal of Materials Science* **48** 4336-44

[86] Liu Z, Fan T, Zhang D, Gong X and Xu J 2009 Hierarchically porous ZnO with high sensitivity and selectivity to H(2)S derived from biotemplates *Sensors and Actuators B-Chemical* **136** 499-509

[87] Merzlyak A and Lee S W 2006 Phage as templates for hybrid materials and mediators for nanomaterial synthesis *Current Opinion in Chemical Biology* **10** 246-52

[88] Mao C, Liu A and Cao B 2009 Virus-Based Chemical and Biological Sensing *Angewandte Chemie-International Edition* **48** 6790-810

[89] Mao C B, Flynn C E, Hayhurst A, Sweeney R, Qi J F, Georgiou G, Iverson B and Belcher A M 2003 Viral assembly of oriented quantum dot nanowires *Proceedings of the National Academy of Sciences of the United States of America* **100** 6946-51

[90] Haberer E D, Joo J H, Hodelin J F and Hu E L 2009 Enhanced photogenerated carrier collection in hybrid films of bio-templated gold nanowires and nanocrystalline CdSe *Nanotechnology* **20** 4215206

[91] Joo J H, Hodelin J F, Hu E L and Haberer E D 2012 Viral-assisted assembly and photoelectric response of individual Au/CdSe core-shell nanowires *Materials Letters* **89** 347-50

[92] Ishida T, Tsuneda S, Nishida N, Hara M, Sasabe H and Knoll W 1997 Surface-conditioning effect of gold substrates on octadecanethiol self-assembled monolayer growth *Langmuir* **13** 4638-43

[93] Tsai H C, Hu E, Perng K, Chen M K, Wu J C and Chang Y S 2003 Instability of gold oxide Au2O3 *Surface Science* **537** L447-L50

[94] Brust M, Bethell D, Kiely C J and Schiffrin D J 1998 Self-assembled gold nanoparticle thin films with nonmetallic optical and electronic properties *Langmuir* **14**

[95] Fishelson N, Shkrob I, Lev O, Gun J and Modestov A D 2001 Studies on charge transport in self-assembled gold-dithiol films: Conductivity, photoconductivity, and photoelectrochemical measurements *Langmuir* **17** 403-12

[96] French R W, Milsom E V, Moskalenko A V, Gordeev S N and Marken F 2008 Assembly, conductivity, and chemical reactivity of sub-monolayer gold nanoparticle junction arrays *Sensors and Actuators B-Chemical* **129** 947-52

[97] Sugden M W, Richardson T H and Leggett G 2010 Sub-10 Omega Resistance Gold Films Prepared by Removal of Ligands from Thiol-Stabilized 6 nm Gold Nanoparticles *Langmuir* **26** 4331-8

[98] Goldsmith B R, Mitala J J, Jr., Josue J, Castro A, Lerner M B, Bayburt T H, Khamis S M, Jones R A, Brand J G, Sligar S G, Luetje C W, Gelperin A, Rhodes P A, Discher B M and Johnson A T C 2011 Biomimetic Chemical Sensors Using Nanoelectronic Readout of Olfactory Receptor Proteins *Acs Nano* **5** 5408-16

[99] Wu T Z, Lo Y R and Chan E C 2001 Exploring the recognized bio-mimicry materials for gas sensing *Biosensors & Bioelectronics* **16** 945-53

[100] Mascini M, Macagnano A, Monti D, Del Carlo M, Paolesse R, Chen B, Warner P, D'Amico A, Di Natale C and Compagnone D 2004 Piezoelectric sensors for dioxins: a biomimetic approach *Biosensors & Bioelectronics* **20** 1203-10

[101] Lim J H, Park J, Ahn J H, Jin H J, Hong S and Park T H 2013 A peptide receptor-based bioelectronic nose for the real-time determination of seafood quality *Biosensors & Bioelectronics* **39** 244-9

[102] McAlpine M C, Agnew H D, Rohde R D, Blanco M, Ahmad H, Stuparu A D, Goddard W A, III and Heath J R 2008 Peptide-nanowire hybrid materials for selective sensing of small molecules *Journal of the American Chemical Society* **130** 9583-9

[103] Park M, Cella L N, Chen W, Myung N V and Mulchandani A 2010 Carbon nanotubes-based chemiresistive immunosensor for small molecules: Detection of nitroaromatic explosives *Biosensors and Bioelectronics* **26** 1297-301

[104] Staii C and Johnson A T 2005 DNA-decorated carbon nanotubes for chemical sensing *Nano Letters* **5** 1774-8

[105] Jaworski J W, Raorane D, Huh J H, Majumdar A and Lee S-W 2008 Evolutionary screening of biomimetic coatings for selective detection of explosives *Langmuir* **24** 4938-43

[106] Jin H, Won N, Ahn B, Kwag J, Heo K, Oh J-W, Sun Y, Cho S G, Lee S-W and Kim S 2013 Quantum dot-engineered M13 virus layer-by-layer composite films for highly selective and sensitive turn-on TNT sensors *Chemical Communications* **49** 6045-7

[107] Kim T H, Lee B Y, Jaworski J, Yokoyama K, Chung W-J, Wang E, Hong S, Majumdar A and Lee S-W 2011 Selective and Sensitive TNT Sensors Using Biomimetic Polydiacetylene-Coated CNT-FETs *Acs Nano* **5** 2824-30

[108] Dong D, Zhang Y, Sutaria S, Konarov A and Chen P 2013 Binding Mechanism and Electrochemical Properties of M13 Phage-Sulfur Composite *Plos One* **8**

[109] Mohammadzadeh F, Jahanshahi M and Rashidi A M 2012 Preparation of nanosensors based on organic functionalized MWCNT for H2S detection *Applied Surface Science* **259** 159-65

[110] Lu J-G, Zheng Y-F and He D-L 2006 Selective absorption of H2S from gas mixtures into aqueous solutions of blended amines of methyldiethanolamine and 2-tertiarybutylamino-2-ethoxyethanol in a packed column *Separation and Purification Technology* **52** 209-17

[111] Mandal B P, Biswas A K and Bandyopadhyay S S 2004 Selective absorption of H2S from gas streams containing H2S and CO2 into aqueous solutions of N-methyldiethanolamine and 2-amino-2-methyl-1-propanol *Separation and Purification Technology* **35** 191-202

[112] Yu J, Becker M L and Carri G A 2012 The Influence of Amino Acid Sequence and Functionality on the Binding Process of Peptides onto Gold Surfaces *Langmuir* **28** 1408-17

[113] Sarikaya M, Tamerler C, Jen A K Y, Schulten K and Baneyx F 2003 Molecular biomimetics: nanotechnology through biology *Nature Materials* **2** 577-85

[114] Moon C H, Zhang M, Myung N V and Haberer E D 2014 Highly sensitive hydrogen sulfide (H2S) gas sensors from viral-templated nanocrystalline gold nanowires *Nanotechnology* **25**

[115] Yang F, Kung S-C, Cheng M, Hemminger J C and Penner R M 2010 Smaller is Faster and More Sensitive: The Effect of Wire Size on the Detection of Hydrogen by Single Palladium Nanowires *Acs Nano* **4** 5233-44

[116] Khanuja M, Kala S, Mehta B R and Kruis F E 2009 Concentration-specific hydrogen sensing behavior in monosized Pd nanoparticle layers *Nanotechnology* **20**

[117] Manocchi A K, Horelik N E, Lee B and Yi H 2010 Simple, Readily Controllable Palladium Nanoparticle Formation on Surface-Assembled Viral Nanotemplates *Langmuir* **26** 3670-7

[118] See supplementary material at [URL] for energy dispersive spectroscope spectra of Au-Pd nanopeapods.

[119] Hill R M 1969 ELECTRICAL CONDUCTION IN ULTRA THIN METAL FILMS .2. EXPERIMENTAL *Proceedings of the Royal Society of London Series a-Mathematical and Physical Sciences* **309** 397-&

[120] Yang F, Taggart D K and Penner R M 2009 Fast, Sensitive Hydrogen Gas Detection Using Single Palladium Nanowires That Resist Fracture *Nano Letters* **9** 2177-82

[121] Offermans P, Tong H D, van Rijn C J M, Merken P, Brongersma S H and Crego-Calama M 2009 Ultralow-power hydrogen sensing with single palladium nanowires *Applied Physics Letters* **94**

[122] Lee Y T, Lee J M, Kim Y J, Joe J H and Lee W 2010 Hydrogen gas sensing properties of PdO thin films with nano-sized cracks *Nanotechnology* **21**

[123] Sennik E, Kilinc N and Ozturk Z Z 2010 Temperature-dependent H-2 gas-sensing properties of fabricated Pd nanowires using highly oriented pyrolytic graphite *Journal of Applied Physics* **108**

[124] Zeng X Q, Latimer M L, Xiao Z L, Panuganti S, Welp U, Kwok W K and Xu T 2011 Hydrogen Gas Sensing with Networks of Ultrasmall Palladium Nanowires Formed on Filtration Membranes *Nano Letters* **11** 262-8

[125] Barwinski B 1985 TEMPERATURE-DEPENDENCE OF ELECTRICAL-CONDUCTION IN DISCONTINUOUS GOLD-FILMS ON SAPPHIRE SUBSTRATES *Thin Solid Films* **128** 1-9

[126] Neugebauer C A and Webb M B 1962 ELECTRICAL CONDUCTION MECHANISM IN ULTRATHIN, EVAPORATED METAL FILMS *Journal of Applied Physics* **33** 74-&

[127] Patton J F, Lavrik N V, Joy D C, Hunter S R, Datskos P G, Smith D B and Sepaniak M J 2012 Characterization of hydrogen responsive nanoporous palladium films synthesized via a spontaneous galvanic displacement reaction *Nanotechnology* **23**

[128] Moon C H, Myung N V and Haberer E D 2014 Chemiresistive hydrogen gas sensors from gold-palladium nanopeapods *Applied Physics Letters* **105**

[129] Gao P, Ying C, Wang S Q, Ye L N, Guo Q X and Xie Y 2006 Low temperature hydrothermal synthesis of ZnO nanodisk arrays utilizing self-assembly of surfactant molecules at solid-liquid interfaces *Journal of Nanoparticle Research* **8** 131-6

[130] Umar A, Chauhan M S, Chauhan S, Kumar R, Kumar G, Al-Sayari S A, Hwang S W and Al-Hajry A 2011 Large-scale synthesis of ZnO balls made of fluffy thin nanosheets by simple solution process: Structural, optical and photocatalytic properties *Journal of Colloid and Interface Science* **363** 521-8

[131] Zhang W, Zhang D, Fan T, Ding J, Gu J, Guo Q and Ogawa H 2006 Biomimetic zinc oxide replica with structural color using butterfly (Ideopsis similis) wings as templates *Bioinspiration & Biomimetics* **1** 89-95

[132] Wei Z, Maeda Y and Matsui H 2011 Discovery of Catalytic Peptides for Inorganic Nanocrystal Synthesis by a Combinatorial Phage Display Approach *Angewandte Chemie-International Edition* **50** 10585-8

[133] Rothenstein D, Claasen B, Omiecienski B, Lammel P and Bill J 2012 Isolation of ZnO-Binding 12-mer Peptides and Determination of Their Binding Epitopes by NMR Spectroscopy *Journal of the American Chemical Society* **134** 12547-56

[134] Huang Z, Yan D, Yang M, Liao X, Kang Y, Yin G, Yao Y and Hao B 2008 Preparation and characterization of the biomineralized zinc oxide particles in spider silk peptides *Journal of Colloid and Interface Science* **325** 356-62

[135] Nam K T, Lee Y J, Krauland E M, Kottmann S T and Belcher A M 2008 Peptide-mediated reduction of silver ions on engineered biological scaffolds *Acs Nano* **2** 1480-6

[136] Rong J, Lee L A, Li K, Harp B, Mello C M, Niu Z and Wang Q 2008 Oriented cell growth on self-assembled bacteriophage M13 thin films *Chemical Communications* 5185-7

[137] Banerjee I A, Muniz G, Lee S Y and Matsui H 2007 Mineralization of semiconductor nanocrystals on peptide-coated bionanotubes and their pH-dependent morphology changes *Journal of Nanoscience and Nanotechnology* **7** 2287-92

[138] Kolodziejczak-Radzimska A and Jesionowski T 2014 Zinc Oxide-From Synthesis to Application: A Review *Materials* **7** 2833-81

[139] Venkatesh P S, Dharmaraj P, Purushothaman V, Ramakrishnan V and Jeganathan K 2015 Point defects assisted NH3 gas sensing properties in ZnO nanostructures *Sensors and Actuators B-Chemical* **212** 10-7

[140] Liao Y C, Xie C S, Liu Y and Huang Q W 2013 Enhancement of photocatalytic property of ZnO for gaseous formaldehyde degradation by modifying morphology and crystal defect *Journal of Alloys and Compounds* **550** 190-7

[141] Bai H, Xu F, Anjia L and Matsui H 2009 Low temperature synthesis of ZnO nanowires by using a genetically-modified collagen-like triple helix as a catalytic template *Soft Matter* **5** 966-9

[142] Wang Y, Liao X, Huang Z, Yin G, Gu J and Yao Y 2010 Preparation and characterization of Ni-doped ZnO particles via a bioassisted process *Colloids and Surfaces a-Physicochemical and Engineering Aspects* **372** 165-71

[143] Anjia L, Wei Z and Matsui H 2012 One-pot crystalline ZnO nanorod growth in mineralizing peptide gels *Rsc Advances* **2** 5516-9

[144] Gerstel P, Hoffmann R C, Lipowsky P, Jeurgens L P H, Bill J and Aldinger F 2006 Mineralization from aqueous solutions of zinc salts directed by amino acids and peptides *Chemistry of Materials* **18** 179-86

[145] Thai C K, Dai H X, Sastry M S R, Sarikaya M, Schwartz D T and Baneyx F 2004 Identification and characterization of Cu2O- and ZnO-binding polypeptides by Escherichia coli cell surface display: Toward an understanding of metal oxide binding *Biotechnology and Bioengineering* **87** 129-37

[146] Golec P, Karczewska-Golec J, Los M and Wegrzyn G 2012 Novel ZnO-binding peptides obtained by the screening of a phage display peptide library *Journal of Nanoparticle Research* **14**

[147] Liang M-K, Deschaume O, Patwardhan S V and Perry C C 2011 Direct evidence of ZnO morphology modification via the selective adsorption of ZnO-binding peptides *Journal of Materials Chemistry* **21** 80-9

[148] Donatan S, Yazici H, Bermek H, Sarikaya M, Tamerler C and Urgen M 2009 Physical elution in phage display selection of inorganic-binding peptides *Materials Science & Engineering C-Biomimetic and Supramolecular Systems* **29** 14-9

[149] Sawada H, Wang R P and Sleight A W 1996 An electron density residual study of zinc oxide *Journal of Solid State Chemistry* **122** 148-50

[150] Togashi T, Yokoo N, Umetsu M, Ohara S, Naka T, Takami S, Abe H, Kumagai I and Adschiri T 2011 Material-binding peptide application-ZnO crystal structure control by means of a ZnO-binding peptide *Journal of Bioscience and Bioengineering* **111** 140-5

[151] Baier J, Blumenstein N J, Preusker J, Jeurgens L P H, Welzel U, Do T A, Pleiss J and Bill J 2014 The influence of ZnO-binding 12-mer peptides on bio-inspired ZnO formation *Crystengcomm* **16** 5301-7

[152] Limo M J, Ramasamy R and Perry C C 2015 ZnO Binding Peptides: Smart Versatile Tools for Controlled Modification of ZnO Growth Mechanism and Morphology *Chemistry of Materials* **27** 1950-60

[153] Kim S H, Olson T Y, Satcher J H, Jr. and Han T Y-J 2012 Hierarchical ZnO structures templated with amino acid based surfactants *Microporous and Mesoporous Materials* **151** 64-9

[154] Barth A 2000 The infrared absorption of amino acid side chains *Progress in Biophysics & Molecular Biology* **74** 141-73

[155] Dutta S, Chattopadhyay S, Sarkar A, Chakrabarti M, Sanyal D and Jana D 2009 Role of defects in tailoring structural, electrical and optical properties of ZnO *Progress in Materials Science* **54** 89-136

[156] Xu P S, Sun Y M, Shi C S, Xu F Q and Pan H B 2003 The electronic structure and spectral properties of ZnO and its defects *Nuclear Instruments & Methods in Physics Research Section B-Beam Interactions with Materials and Atoms* **199** 286-90

[157] Zeng H, Duan G, Li Y, Yang S, Xu X and Cai W 2010 Blue Luminescence of ZnO Nanoparticles Based on Non-Equilibrium Processes: Defect Origins and Emission Controls *Advanced Functional Materials* **20** 561-72

[158] Li Q H, Gao T, Wang Y G and Wang T H 2005 Adsorption and desorption of oxygen probed from ZnO nanowire films by photocurrent measurements *Applied Physics Letters* **86**

[159] Furuta M, Kamada Y, Kimura M, Shimakawa S-i, Kawaharamura T, Wang D, Li C, Fujita S and Hirao T 2011 Photocurrent and Persistent Photoconductivity in Zinc Oxide Thin-Film Transistors under Ultraviolet-Light Irradiation *Japanese Journal of Applied Physics* **50**

Appendix A. Construction of pVIII Library

A modified M13 vector named M13SK was used for genetic insertion of random 8-mer oligonucleotide in the gVIII region. The wild-type M13 vector was modified at the 1372 site from T to A to insert a *PstI* restriction site and at 1382 site from C to G for *BamHI* site. Another *PstI* restriction enzyme site at 6246 was removed by modifying the T at 6250 site to A. An oligonucleotide 5'- CTA CTA CAA GGA TCC NNM NNM NNM NNM NNM NNM NNM NCT GCA GCG AAA GAC AGC A -3' (Integrated DNA Technologies) was annealed and extended following the standard procedure. N and M represents mixed bases where random insertion of G, C, A, T and T, G each with equal percentage is inserted, respectively. The oligonucleotide duplex and vector was digested with *BamHI* and *PstI* restriction enzymes overnight at 37°C, and purified for further usage. These digested DNAs were ligated and inserted into the electrocompetent cells (Stratagene) through electroporation, which was then amplified for the final pVIII library.

Table A 1 lists the expected % and actual % of each amino acid chemical groups obtained in the pVIII library. The expected % of the amino acid group was calculated as (# DNA codons that encode amino acid group)/(total # DNA codons) x 100. The first position of the peptide sequence was restricted to G, V, A, E, D amino acids due to the *PstI* restriction enzyme site. High percentage of acidic (E, D) and proline (P) groups and lower percentage of basic (H, R, K) and ring (F, W) groups were observed in the final pVIII library. We attribute this to the nature of pVIII coat protein, which is natively negatively charged and also very tightly packed in the α-helical form. This negative charge preference and steric hindrance prevent assembly of the viral protein coats in presence of positively charged and large ring group amino acids. The diversity of the pVIII library constructed was $3.65x10^7$ clones and was employed for discovery of various target materials.

Table A 1 Percentage of expected and actual amino acid groups present pVIII library.

Amino Acids	Expected %	Actual %
Basic: R, K, H	15.6	3.1
Acidic: E, D	6.3	19.1
Hydrophobic: A, V, G, I L	32.8	36.1
Amide: Q, N	6.3	6.6
Ring: F, W	4.7	0.3
Hydroxyl: S, T, Y	18.8	19.4
Proline: P	6.3	11.5
Methionine: M	1.6	3.8

Appendix B. Discovery of SiO_2-Binding Peptides

Combinatorial phage display screening is used to identify a phage and its corresponding peptide that has affinity for a specific target. Here, negative biopanning was performed to discover a phage with affinity to silicon dioxide (SiO_2) and specifically not to gold (Au). The procedure for negative biopanning was modified from the standard biopanning procedure described in Chapter 5. Instead of adding the library directly to the target material SiO_2, the library was added to an Au foil in Tris-buffer saline with 0.1% Tween-20 (TBST, 50 mM Tris-Cl, 150 mM NaCl, pH 7.5) and incubated at room temperature for 1 h. The supernatant containing unbound phages were removed, then added to the target material, SiO_2 chunks in 0.1% TBST. Here onward, the standard biopanning procedure was followed. Briefly, the phage unbound to Au were incubated with SiO_2 for 1 h, then washed to remove unbound phages to SiO_2, followed by elution of phages from SiO_2 chunks. The eluted phages were determined by DNA sequencing. The biopanning procedure was repeated 4 times to identify phages and its peptides with affinity to SiO_2 and not Au, as shown in Table B 1. Statistical analysis of the peptides found after 4 rounds of biopanning is shown in Table B 2. High frequency of hydrophobic residues (V, G, A, I, L) was as expected from their presence in the library. Notably high percentage of acidic aspartic acid (D), as well as basic lysine (K) and arginine (R) residues were detected. Lysine occurred 12 fold more in this biopanning round than the library. Phage with sequence similar to consensus sequence, DPKSADLT, and that containing most recurrent sequence, DKPGSDLT were selected for further study.

Table B 1 List of peptide sequences obtained after 4 rounds of negative biopanning for SiO_2 and not Au. Nineteen sequences were obtained and 2 out of 19 were unmodified phages.

Peptide Sequence	Frequency
DKPGSDLT	4/17
DPKSADLT	1/17
DKSTESMT	1/17
VQEATKVE	1/17
DPSKQMPE	1/17
VPQSGVDA	1/17
DPKGAEIV	1/17
DPRAPELV	1/17
DPRTADAA	1/17
DSRQDLSA	1/17
DLKSGAPE	1/17
DPKSADAT	1/17

Table B 2 Statistical analysis of peptides obtained after 4 rounds of negative biopanning. The frequency of each amino acid occurrence at each position within all resulting sequences was calculated. The amino acids are presented in single letter form and color coded according to its chemical moieties. The consensus sequence is shown at the bottom of the list.

Amino Acid	Percentage of frequency at each position in peptide (%)								Frequency of occurrence (%)	
	1	**2**	**3**	**4**	**5**	**6**	**7**	**8**	against SiO_2	in library
F	0	0	0	0	0	0	0	0	0	0.3
W	0	0	0	0	0	0	0	0	0	0
M	0	0	0	0	0	6	12	0	2.2	3.8
P	0	47	24	0	6	0	12	0	11.0	11.5
H	0	0	0	0	0	0	0	0	0	0.7
K	0	29	29	6	0	6	0	0	8.8	0.7
R	0	0	18	0	0	0	0	0	2.2	1.7
N	0	0	0	0	0	0	6	0	0.7	2.8
Q	0	6	6	6	6	0	0	6	3.7	3.8
E	0	0	6	0	6	18	0	18	5.9	11.1
D	82	0	0	0	6	47	6	0	17.6	8.0
V	18	0	0	0	0	6	6	12	5.1	6.3
G	0	0	0	29	12	0	0	0	5.1	9.7
A	0	0	0	18	29	6	12	18	10.3	12.8
I	0	0	0	0	0	0	6	0	0.7	0.7
L	0	6	0	0	0	6	35	0	5.9	6.6
Y	0	6	6	12	6	0	0	47	9.6	8.7
S	0	6	12	29	29	6	6	0	11.0	10.8
T	0	0	0	0	0	0	0	0	0	0
C	0	0	0	0	0	0	0	0	0	0
	D	**P**	**K**	**G**	**A**	**D**	**L**	**T**	**Consensus**	
				S	**S**					

Binding affinity of recurrent (DKPGSDLT) and consensus (DPKSADLT) sequence was determined using the standard binding test, in comparison to the wild type M13 phage. For these sequences, confirmation of phages not binding to Au was equally important as their affinity for SiO_2. Therefore, the binding test was performed on both Au foil and SiO_2 chunk materials. As shown in Figure B 1, both phages displayed greater affinity for SiO_2 than wild type phage, by showing 1768 and 484 times higher phage concentrations. However, in comparing phage affinity to SiO_2 to Au, the recurrent phage (DKPGSDLT) showed 5.3×10^3 pfu/μL and 2.8×10^1 pfu/μL concentrations of bound phage, respectively, resulting 189 times greater binding to SiO_2 than Au. The consensus (DPKSADLT) on the other hand, only showed 9 times more affinity to SiO_2 than Au, with bound phage concentrations of 1.5×10^3 pfu/μL and 1.7×10^2 pfu/μL, respectively. Such large difference in affinity between these phages was notable, particularly considering how close these two sequences are differing by only 1 amino acid and order of 2 amino acids. This suggest that not only the individual amino acid, but the ordering and peptide sequence as whole affects peptide or phage binding to target materials. The recurrent phage displayed strong affinity for SiO_2 than Au, and can be utilized to form SiO_2 specific structures in nanomaterial synthesis.

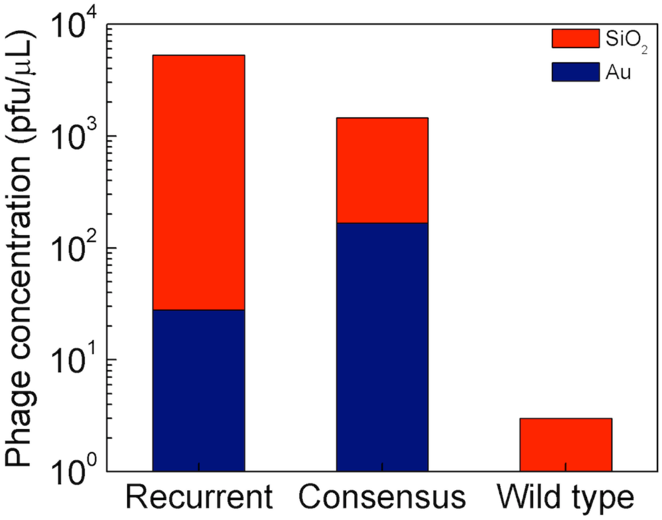

Figure B 1 The binding strength of recurrent, consensus, and wild-type phages for SiO_2 (red) and Au (blue). Bar height that starts from 0 indicates concentration of phages that were bound and eluted from each target materials.